A 3D High-Order Aeroacoustics Model for Turbomachinery Fan Noise Propagation

by
Matthew Morgan Cand
Department of Mechanical Engineering
Imperial College London / University of London

A thesis submitted for the degree of
Doctor of Philosophy
June 2005

Abstract

This study investigates computational tools to predict forward-arc fan noise from aero-engines. Efficient computational procedures are needed to model sound propagating in the intermediate zone between the fan assembly and the intake surroundings, where boundary-element methods can then propagate it to the ground level. A high-order method that is able to fully simulate the intake geometry's non-axisymmetric nature, while remaining faster than traditional methods, is investigated.

Following a review of the literature, a code solving the linearised Euler equations, using a time-domain finite difference scheme, is developed. For the solid wall boundary condition, an immersed boundary technique designed for aeroacoustics, with a careful extrapolation of values from the fluid, allows a regular Cartesian grid to be used in the whole domain. A novel 3D formulation of this method, suitable for the aeroacoustics problems considered, was developed, and the algorithm is described in detail.

This scheme is first applied to a series of standard benchmark cases, of increasing complexity, for validation purposes. Some more representative 3D inlet cases are then simulated: a simple model of the JT15D bellmouth turbofan and an elliptic profile. Finally, the effect of an asymmetric inlet geometry on modal propagation is investigated. Comparisons are made with results from a 2D aeroacoustics code, and from a traditional computational fluid dynamic scheme, evaluating the benefit of using the current approach. It is shown that a high-order scheme is more computationally efficient than low-order techniques, by at least one order of magnitude. But the wall boundary condition is shown to be excessively dissipative in 3D, and further work is needed to improve its accuracy.

Acknowledgements

I would like to address heartfelt thanks to my supervisors, Pr. Mehmet Imregun and Dr. Abdulnaser Sayma. First, for directing me towards this research subject, but mostly for their patience, their supernatural ability to point me in the right direction every time, and their constant availability despite a busy schedule.

For providing ACTRAN solutions for comparison, as well as guidance, the help and efforts of Dr. Naoki Tsuchiya and Prof. Jeremy Astley, from the Institute of Sound and Vibration, University of Southampton, U.K., are gratefully acknowledged.

Thanks also to those, too numerous to mention all, who provided friendly advice and guidance when we met. Amongst them: Brian Tester, François Moyroud, Alexander Wilson, Joaquim Peiró, Spencer Sherwin, Fred Perié, Pr. Hirsch ...

I am grateful for the essential financial support of the *Fondation de l'Ecole Polytechnique* and the *OECD*.

Many thanks to the delightful colleagues which made working much nicer: Dr. Enrique Gutierrez, Dr. Hugo Elizalde, Sen Huang, Dario Di Maio, Gabriel Saiz and Marija Nikolic, Dr. Ibrahim Sever Dr. Suresh Perinpanayagam, and all the italian Erasmus students in the office; Mehdi Vahdati, Michael Kim and Luca Di Mare in the UTC. I will have many fond memories of discussions around (essential) cups of strong coffee.

My parents are to thank for many things, and I will limit myself here to acknowledging, with great affection, their total support and confidence during these long years of study. The same goes for my darling Robyn, the little London bird that I neglected too much in the last 4 years. You made it all worthwhile.

Contents

List of Figures

List of Tables

Nomenclature

Latin

a	Characteristic length scale of the problem.
$A_{nm\mu}$	Amplitude of the (n, m, μ) mode.
$\tilde{A}, \tilde{C}$	Arrays used in the Cartesian wall boundary condition method.
a_j	Finite difference coefficient.
b	Half-width of gaussian profile.
$\tilde{b}$	Intermediate, pre ghost-value vector.
b_j	Optimised Adams-Bashforth scheme coefficients.
c	Speed of sound.
c_g	A wave's group velocity.
$(\vec{e_r}, \vec{e_\theta}, \vec{e_\varphi})$	Basis vectors of the spherical coordinate system.
$\boldsymbol{E}, \boldsymbol{F}, \boldsymbol{G}$	Pseudo-conservative flux vectors (LEE).
$\boldsymbol{H}$	Main flow inhomogeneities vector (LEE).
$\mathcal{F}(\boldsymbol{Q})$	Right-hand side or “residual” vector, for the variable set $\boldsymbol{Q}$.
i	$\sqrt{-1}$
J_m, Y_m	Bessel function of the first and second kind, of order m.
(l, m, n)	Discrete indexes of a Cartesian mesh point.
M	Mach number.
(m, μ)	Acoustic modal indexes (azimuthal, radial).
N_g	Number of ghost points.
p	Pressure.
$\tilde{p}_g$	Vector of ghost pressure values.
$\boldsymbol{Q}$	Unknowns vector (total).
$\boldsymbol{Q}^n$	Unknowns at discretised time level n.
$\boldsymbol{Q'}$	Unknowns vector (perturbations).
$\boldsymbol{Q_0}$	Unknowns vector (mean flow).
R_Δ	Artificial selective dissipation Reynolds number.
$\Re$	Takes the real part of a complex number.
r_w	Wall radius in the inlet duct.
$\boldsymbol{S}$	Acoustic source vector (LEE).

s	Number of Runge-Kutta stages per time step.
t	Time.
T	Temporal period of the signal.
$\boldsymbol{\vec{v}} = (u, v, w)$	*Velocity* vector and 3D Cartesian components.
$\boldsymbol{\vec{V}} = (V_x, V_y, V_z)$	General vector and 3D Cartesian components.
(x, y, z)	Cartesian coordinates.

Greek

α	Wavenumber.
$\alpha_{m\mu}$	Radial wavenumber for mode (m, μ).
$\alpha_{x,m\mu}$	Axial wavenumber for mode (m, μ).
$\bar{\alpha}$	Computed wavenumber.
$\tilde{\alpha}$	Reduced wavenumber, or Helmholtz number.
β_j	Runge-Kutta coefficients.
γ	Ratio of specific heats of the gas.
Δg	Elementary spacing of discretised variable g (Δt, Δx...)
$\vec{\eta}$	Normal vector.
θ	Polar angle.
κ_i	Optimised extrapolation weights.
λ	Wavelength.
Λ_a, Λ_b	Interpolation parameters.
ν	Frequency.
ρ	Density.
σ	Dissipation coefficient for the absorbtion zone (amplitude σ_m).
τ	Scarfing ratio.
φ	Azimuthal angle.
ω	Circular frequency.
ζ	Annular mode coefficient.

Abbreviations

1D	1-dimensional.
2D	2-dimensional.
2.5D	3D problem reduced to 2D using simplifying assumptions.
3D	3-dimensional.
BPF	Blade Passing Frequency.
CAA	Computational Aero-Acoustics.
CAD	Computer Assisted Design.

CFD	Computational Fluid Dynamics.
CFL	Courant-Friedrichs-Lewy number $c(1+M)\Delta t/\Delta x$.
DNS	Direct Numerical Simulation.
DRP	Dispersion Relation Preserving.
ENO	Essentially Non-Oscillatory.
FW-H	Ffowcs-Williams and Hawkings.
HOP	High Order Propagation computational code.
LEE	Linearised Euler Equations.
LES	Large Eddy Simulation.
LDDRK	Low-Dispersion and Dissipation Runge-Kutta scheme.
OAB	Optimised Adams-Bashforth time integration scheme.
PML	Perfectly Matching Layer.
PPW	Points Per Wavelength.
RANS	Reynolds-Averaged Navier-Stokes.
RHS	Right-Hand Side (of an equation).
RMS	Root-Mean-Square.
SPL	Sound Pressure Level.

Chapter 1

Introduction

1.1 Background

1.1.1 The place of noise in civil aviation

The last 50 years have seen a dramatic evolution of the civil aeronautical sector, with a constant increase in air traffic all around the world, by a factor of more than 20 since the sixties. In that time, airplane noise has changed from a source of wonder to a nuisance [1], as the zones surrounding airports are densely populated, and it is now a major concern for the aeronautics industry. In 1969 the USA introduced the first set of aircraft noise regulations: Federal Aviation Regulations part 36. This was followed by several international agreements under the International Civil Aviation Organisation (*ICAO*), the most relevant currently being ICAO Chapter 4, requiring high bypass ratio engines for all new aircrafts to be certified from January 2006 [3]. Regulations are becoming increasingly stringent, and local regulations, such as the ones in effect in the London airports, are often more demanding.

In an industry where large time scales are involved to get a return on investment, any major civil aircraft design must be able to comply with regulations over a long period of time. These constraints are of far-reaching strategic importance: noise significantly restricted usage of the Concorde supersonic aircraft in the USA, which led to an unexpectedly bad commercial performance. A 1997 European regulation on "hush-kits" (adapting older aircrafts to more demanding noise regulations) led to a 5-year cross-atlantic trade dispute.

Since the mid-sixties, significant progress has been made, and noise produced by aircraft engines has been reduced overall by around 20dB: a reduction of two orders of magnitude in the radiated acoustic energy, and a fourfold reduction in perceived noise. This reduction in individually emitted noise has compensated the effect of the increase in traffic. However, trends indicate that this might cease to be the case in the next 10 to 20 years if usage increases at the same rate and significant progress is not made in the acoustic performance of modern aircraft. This is why noise is today one of the main design considerations. Indeed, the point has been reached where performance and economics need to be compromised in order to comply with noise requirements [4]. However, in the future, concerns about climate change may put the reduction of greenhouse effect-causing emissions to the top of the environmental agenda [3].

Because of the nature of civil aviation, the aeronautics industry is of course conservative and risk-averse, operating in a competitive environment demanding high investment costs; therefore in the near- to mid-term there will probably not be any revolutionary modifications of the current classic turbofan airplane engine design. A radical re-thinking of the civilian aircraft, driven by sustainability concerns [5] is for the long-term. Therefore a lot of effort will be concentrated on relatively small modifications of the existing engine design.

1.1.2 The importance of fan noise

Noise emitted by civil aircrafts can be classified [1, 6] into *external* noise, caused by the flow around the aircraft and the jet exhaust, and *internal* engine noise radiating outside. In the latter category, sound mainly originates from the rotor and stator blades in the different compressor and turbine stages, and from the fuel combustion. Jet noise is mainly caused by turbulence occurring as the high-speed exhaust flow mixes with the surrounding air [7], and by the shocks present in under-expanded supercritical jets [8].

The dramatic progress in noise reduction described above has mostly been due to a transition (driven by the need for fuel economy) from pure turbojet engines to turbofans. In the latter, a large fan stage, powered by a highly efficient compressor/turbine core, pushes a relatively slow and cold flow into a secondary surrounding *bypass* duct. This allows the exhaust jet velocity to be reduced, for the same thrust, which dramatically reduces the noise created by the exhaust jet, whose intensity is mostly proportional to the 8^{th} power of the flow velocity. The noise from the fan does increase because of the additional loading, but is more amenable to design techniques, whereas jet noise is difficult to reduce without altering the exhaust speed [1, 7, 9].

This has led to a greater emphasis on the study of blade-related noise. In modern engines this mainly comes from the large main fan, as it interacts with various flow features and blocks a lot of the sound from the compressor and turbine. It is now a dominant source of flyover noise in the critical takeoff and approach flight phases, when the aircraft has a relatively slow speed [10, 11]. It is also during those phases, when the airplane is the closest to the ground level, that the impact of noise on the community is the most significant. Therefore reducing fan noise is crucial for airplane certification [1]. Fig. 1.1 shows a diagram representing the importance of the different noise sources in a modern engine.

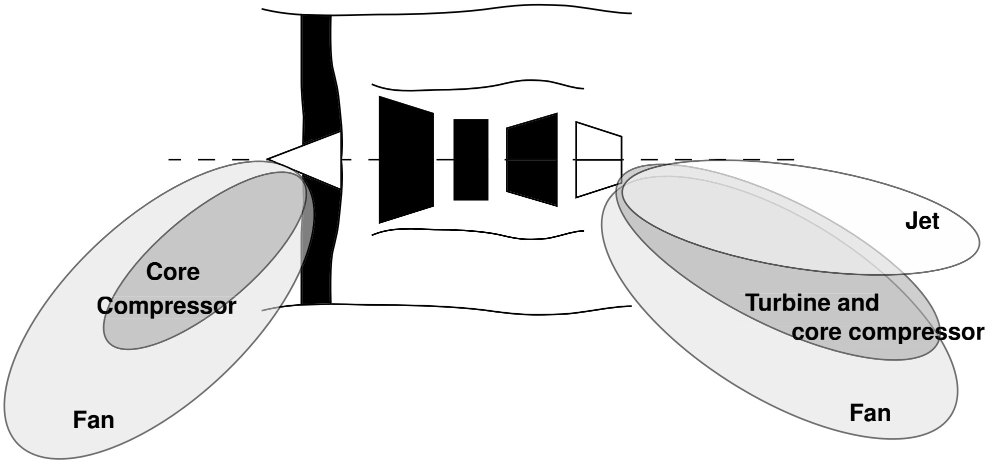

Figure 1.1: Approximate diagram of the noise radiation patterns from a typical modern high-bypass aeroengine [1].

Most of the noise generating mechanisms are now well-known [1, 10, 12]. A typical fan noise spectrum consists of a broadband spectrum, on top of which is found a succession of high-pitched discrete frequency components and their harmonics. The first part is called *broadband noise*, generated by internal turbulence impinging on structures, and the latter is *tone noise*: this loud whine is composed of frequencies which are multiples of the engine rotation frequency (engine orders). Tyler and Sofrin [13] have identified this turbine noise as originating from forward and backward interactions between rotor and stator blade rows: the main fan and associated guiding vanes, and the internal compressor and turbine. The propagation of the associated "spinning" modes in the inlet ducts is very complex [9, 12].

When the fan blade tips are supersonic, shocks are produced. This creates a sound spectrum rich in discrete frequencies, often called "Multiple Pure Tone" noise. Furthermore, the complex interaction of these N-waves amplifies blade-to-blade variability, which adds low engine order components to the pure-tone ones: "buzz-saw" noise [14]. This high-amplitude, relatively low-frequency noise is highly disturbing because it is poorly attenuated by the cabin walls and by the atmosphere.

When the mean flow coming in the inlet is not circumferentially uniform, *distortion* noise can also be produced. This may occur when wind is blowing on the side of the engine, or if an intake droop is disturbing the inflow. The blades, in their rotating frame of reference, perceive this perturbation periodically, which can produce a low engine-order (and therefore low-frequency) sound.

"Lined" walls, porous surfaces with resonant cavities, can absorb a large part of the generated noise spectrum through absorbtion and dissipation mechanisms, as illustrated in Ref. [1]. They were one of the earliest features used to reduce fan noise [6], and are now systematically found in commercial aeroengine inlets. Their design and tuning is delicate, but their presence is critical to the sonic performance of the engine. However, there are limits to this approach, and some other recent fan noise reduction techniques, investigated at the NASA [10] and in European programs devoted to aeroacoustics [4, 15], include:

Fan design: lowering the tip speed or modifying the blade shape can reduce shock strength.

Wake management consists of ensuring that the flow immediately downstream of blades is as smooth as possible to avoid strong noise-generating turbulence.

Optimising the number of blades/bypass vanes: the nature of the modes generated by rotor/stator interaction is related to the number of blades [13]. By carefully adjusting their relative numbers, it is possible to control which modes are generated.

Increasing the rotor/stator distance to make use of the natural decay of wakes.

Using swept/leaned guide vanes as opposed to straight ones, can effectively reduce interaction effects in some cases.

An inversely scarfed inlet: traditionally, engine inlets are *scarfed* so that the upper lip is longer, for aerodynamical reasons. However, negatively-scarfed intakes are being investigated: the extended lower lip is intended to reflect most of the sound away from the ground.

Active control: this regroups all methods trying to cancel out sound by the means of diverse actuators or generators, responding to the noise levels through a carefully designed feedback chain.

It should be noted that many of these modifications involve complex, strongly 3-dimensional effects. More importantly, many are also strongly linked to aerodynamic or aeroelastic aspects of the engine design [16]: concerns such as blade vibration and robustness, the power regime and efficiency of the engine, *etc.* For example, a negatively scarfed inlet might cause inflow distortion, and might also affect the wing's lift or create drag.

Because of progress in materials and techniques, fan blades are getting lighter; this means higher vibrations, and aeroelastic interactions with the acoustic and unsteady flow when there is a match (in shape and frequency) between structural and acoustic modes. Vahdati *et al.* [17], and later Wu *et al.* [18], examined the influence of inlet acoustics on the fan blades' "flutter", or self-excited vibrations. Both domains of expertise, aeroelasticity and aeroacoustics, are now closely linked, while the requirements for quieter engines get at the same time more important and more difficult to meet. This challenge demands an integrated design solution.

1.2 Problem statement

1.2.1 The need for computational models

Analytical solutions of acoustic equations are complex, even in the simplest cases [19]. In most realistic situations, a solution is out of reach, unless some strongly simplifying assumptions are made, and the effects of the underlying flow are rarely taken into account. Özyörük [9] presents a review of early fan noise modelling methods; for example, Nayfeh presented several models [6]. More recently, the multi-scales propagation model for slowly varying ducts of Rienstra [20], or in the case of high frequencies, ray theory [21, 22], have been used to study propagation inside the duct, and the diffraction at the lip, for relatively simple geometries. Empirical methods are also widely used in the industry; several examples in the current domain of interest can be found in the literature [12, 23]. But these simple models have their limits.

On the other hand, experiments on aeroengines are very costly and lengthy to set up [9]. Therefore, it is important to develop predictive computational models to simulate these phenomena, for use in the design phase. A computed solution is known over the whole domain of study, compared to experiments that can only give a limited set of measurement points. This allows a better understanding of the physical mechanisms underpinning certain behaviours. For example, numerical experiments by Tam and Kurbatskii [24] have precisely identified the mechanisms providing sound dissipation through vortex shedding in certain acoustic liners.

1.2.2 Computational aeroacoustics

As aeroacoustics is a particular branch of fluid mechanics, it is theoretically possible to use a traditional Computational Fluid Dynamics (*CFD*) code to study noise. In the last 30 years this area of research has matured, and very efficient and robust CFD methods have been developed, and validated for a variety of applications [25]. To include the effect of turbulence in viscous fluids, a Direct Numerical Simulation (*DNS*) approach can be taken, or a less computationally expensive modelling of turbulence through Large Eddy Simulation (*LES*) or Reynolds-Averaged Navier-Stokes (*RANS*) approaches [25].

A typical example is the AU3D code: it can solve the RANS equations with a second-order accurate finite volume formulation on hybrid (structured and unstructured) grids. A mix of adaptive Jameson second and fourth order dissipation combined with a pressure sensor prevents odd-even oscillation, while preserving accuracy in the smooth regions and reverting to first order near shocks. It advances the solution in time using a second-order backwards implicit formulation, with dual time-stepping [26–28].

The fan region is home to many strongly non-linear noise-generating phenomena, where vorticity, turbulence, solid-fluid interaction, shear layers, viscous effects, *etc.* play a large part. A traditional CFD, viscid or inviscid solver can, in principle, model sound generated by these effects, and propagate it over a short distance. Rumsey *et al.* [29] describe the use of a similar code, CFL3D, developed in the NASA Langley Research Center, to model tone noise in a realistic 3D ducted-fan aeroengine geometry.

As many researchers have pointed out [9, 30–33], and as will be explained in Chapter 2, traditional CFD codes cannot cope well with the nature of sound signals. This is because they employ low-order discretisation schemes, for their relative ease of development and coding. These schemes also do not require highly accurate boundary conditions, grid metrics, or expensive computations at each discretisation point; they are quite robust and have effectively modelled many fluid phenomena. But when it comes to propagating the generated sound waves, it became apparent that, unless a very fine spatial resolution is used (at prohibitive computational cost), or large wavelengths are studied [17], important phase and amplitude errors appear. Often, the waves, already of low amplitude relatively to the ambient flow, are numerically dissipated after a few wavelengths. The disparity between the length scales of the problem and the short acoustic wavelengths is also a major problem. This explains the considerable interest in dedicated, efficient numerical methods, and the relatively recent emergence of the field of Computational Aero-Acoustics (*CAA*) [30].

Although general CAA principles and methods are now starting to be well-established, there still is a need for efficient techniques to model sound scattering from complex geometries, while still retaining a high order of accuracy. Overall, two main approaches can be found: using *unstructured* grids, or using a *structured* body-fitted grid mapped to a regular computational domain. These techniques and the related discretisation schemes will be reviewed in Chapter 2 and 3. Curved grids, and to a lesser extent unstructured grids, are problematic to generate, of poor quality except in the simplest cases, and can be the source of numerical instability and distortions. In the current work, an alternative structured approach will be investigated, using techniques that allow the use of regular, uniform grid in the whole domain. This means that strongly non-uniform problems would be difficult to model, but in most of the domain a discretisation with good isotropy and resolution characteristics, adapted to acoustics, will be used, avoiding the meshing problems outlined above.

1.2.3 The mid-field domain

A traditional CFD method can be used in the internal region of the engine (as shown in the centre of Fig. 1.2), to simulate the aerodynamic and aeroelastic behaviour of the forward region of the engine. This includes the generation of sound and its accurate propagation in this limited region, where a fine grid can be used. On the other hand, integral methods, described in Section 2.1.3, can take, as input, the sound on a certain surface and propagate it to the far-field very efficiently; however, they do not model acoustic/aerodynamic interactions or the effects of propagation through complex non-uniform mean flows [9, 34].

There is therefore a need for methods that propagate sound in the *mid-field*: between the near-field where the sources of sound reside, and the zone where the flow is uniform; it must be able to model the complex refraction and wavelength-shifting effects caused by non-trivial flows in the transition zone between the internal and the external regions of the engine, as represented in Fig. 1.2. Work of this type has been done, for complex 3D situations, by Özyörük [9, 35, 36] and Stanescu [37–39]. Also of note is the 2D model of Bréard [40], and early studies made by assuming an irrotational flow [41].

It might also be interesting to use the method developed for the mid-field domain in the bypass duct zone downstream of the main fan and the stator vanes. Noise propagation is affected by the complex flow, and the geometry is curved, and non-axisymmetric because of the presence of obstacles like the support pylon.

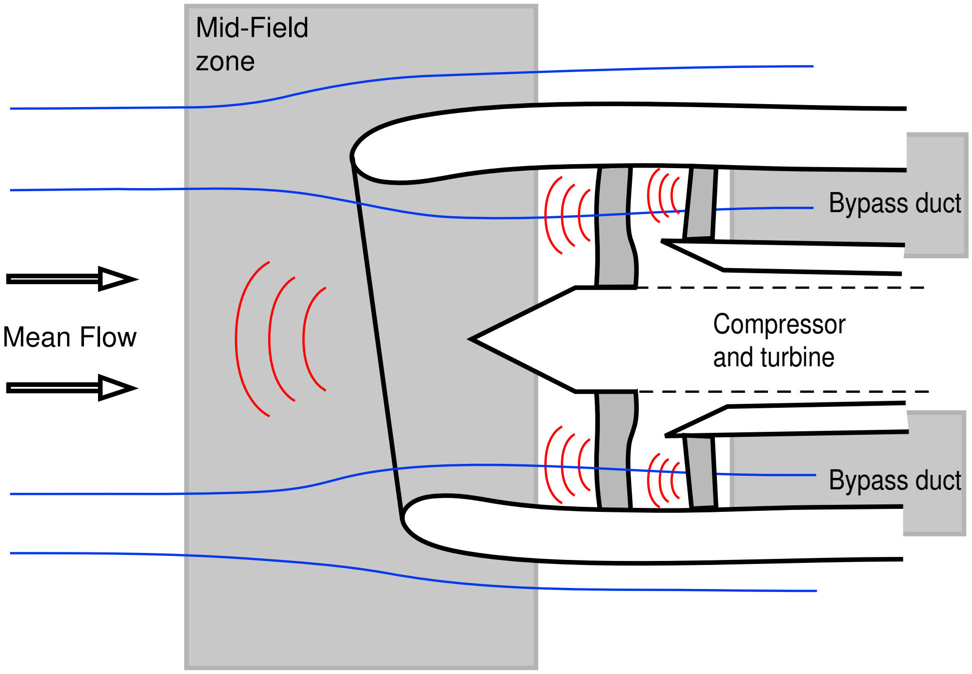

Figure 1.2: Description of the mid-field region in a typical modern aeroengine.

1.3 Scope and aims of the thesis

This work originated in the need for developing an integrated computational design tool, combining well-established aerodynamic and aeroelastic models with acoustic prediction capabilities. Linking both of these aspects of the design of modern aeroengines would shorten the long feedback process that is now necessary given the preponderance of noise concerns.

It is necessary, in such a complex environment, to focus on certain aspects of the noise problem. This study is concerned with the front half of the aeroengine, as aeroelastic design mainly deals with the blades of the large low-pressure fan and of the first stages of the compressor. This domain was studied for example by Özyörük [9] and Keith [22]. The paramount importance of fan noise in modern engine design has been stressed in this chapter. It was decided to focus on tone noise, as broadband noise is of smaller magnitude in most cases, and, by its nature, is less suited to direct numerical simulation. Given the importance of N-waves caused by supersonic fan rotation and the resulting buzz-saw noise, the methods described should also be considered for their ability to model these phenomena. In the context of noise certification, the most important flight phases are takeoff and approach, because of the proximity to the affected communities. This means that the airplane is at relatively low speed, and the mean flow on which the sound propagates will be of low Mach number ($M < 0.3$) [11]. The propagation of these acoustic signals should be designed to be run in parallel to the aeroelastic/dynamic computations, which would then provide the sound source. This hybrid approach would be well-suited to the problem, allowing the use of methods adapted to each part of the problem [34].

The current work concentrates on efficient schemes which are needed to propagate sound in the mid-field region. They must be able to handle the great difference in amplitude between these acoustic perturbation and the flow on which they propagate. The influence of the latter is of great importance, in the zone of interest, since the complex effect this has on sound propagation is the main reason simple models cannot be used. Crucially, the method must provide a great level of accuracy in the resolved sound waves, up to the limit of the computational zone, where integral methods can take over. At the same time it must be able to be used in realistic situations, to solve complex engineering problems. Therefore issues such as implementation and the computational resources used are critical. Finally, the overall scheme, no matter how refined, must be faster than what would be obtained by simply using a traditional CFD scheme with a very fine resolution.

Fully asymmetric inlet geometries, such those found in modern aeroengines, need to be modelled. Furthermore, as has been pointed out above, many of the noise generation mechanisms (like distortion noise) are highly 3-dimensional but cannot be modelled by the many efficient 2D models that exist already.

Therefore, not only must the simulations be fully 3D, but an efficient way to represent complex 3D wall surfaces must also be found. The methods developed here might also be used for other problems with similar requirements.

Outline of the thesis

In Chapter 2, an appropriate set of equations to model the problem at hand is presented, after having separated the acoustic part. The next step is to discretise these equations both in space and time: a review of popular CAA schemes is presented. A finite difference method is implemented, following the requirements described above. The importance, for the correct resolution of acoustic waves, of the scheme's order of accuracy is investigated in detail. This is followed by some notes on implementation and stability, and a quick overview of the correct boundary conditions to be used with this scheme.

In Chapter 3, the need for an efficient way to model complex wall boundaries in the context of CAA is described, preserving the high order of accuracy of the solution. One of the main contributions of the current work is the development of a novel systematic method to deal with 3D wall boundaries. The associated algorithmic and computational issues are addressed.

In Chapter 4, a validation of the code against benchmark results is presented. The basic model and computational scheme, in 2D and 3D, are first considered. Then, the treatment of the wall boundary condition is investigated in detail, first by replicating basic 2D test cases, and then by validating the new 3D approach against a standard benchmark. It is found that the performance of the 3D method is inferior to the 2D one. The effects of complex mean flows are studied in both cases, but instability is observed in the presence of mean flows with important Mach numbers.

In Chapter 5, some more complex situations, of the type commonly encountered in studies of aero-engine noise, are investigated. This includes asymmetric situations. The current scheme performs efficiently overall, but some important dissipation is found to be present close to the wall boundary.

This outline is summarised in Fig. 1.3.

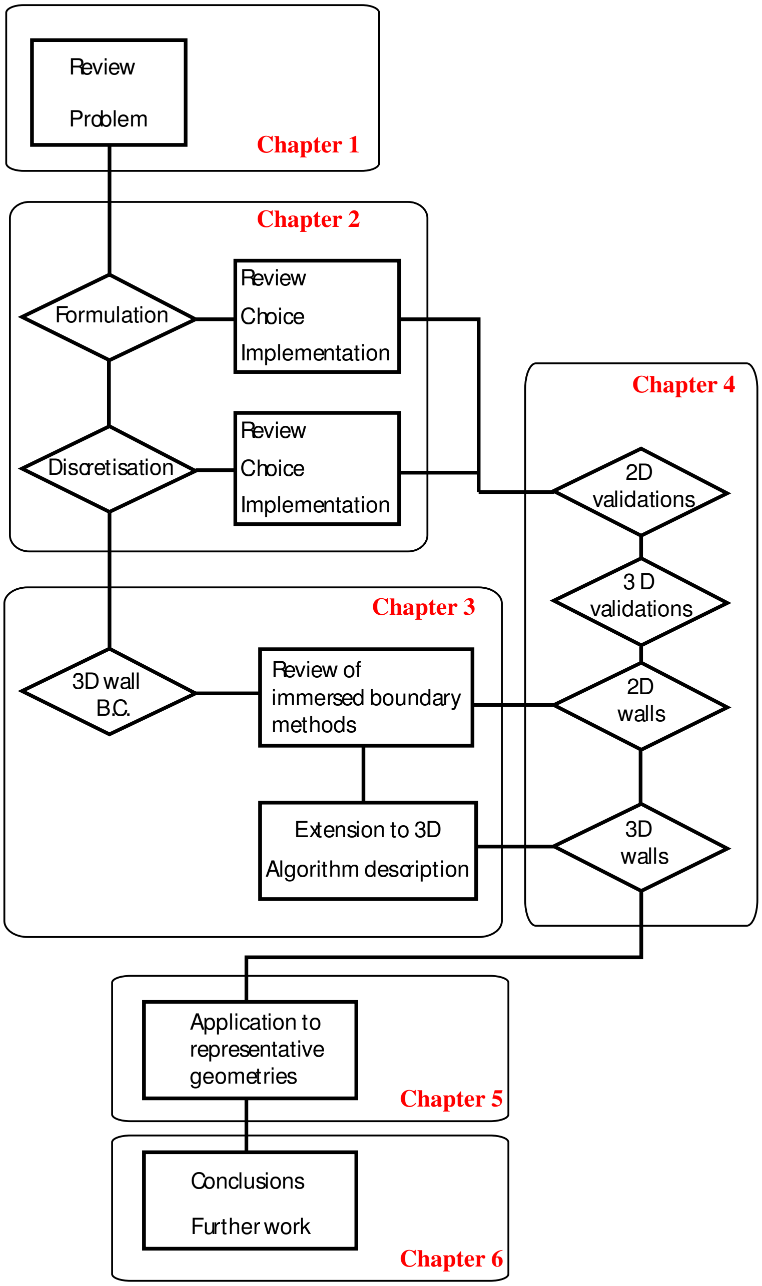

Figure 1.3: Outline of the thesis.

Chapter 2

Model and discretisation

In this chapter, a numerical model is chosen to efficiently solve the problem described in Chapter 1: the complexity of time-accurate sound propagation over arbitrary non-uniform flows must be represented in 3D. First, an appropriate set of equations is considered to this effect, given some acceptable hypotheses. If the acoustic part of the fluid behaviour is treated separately, it is then possible to use dedicated numerical CAA techniques, a review of which is made. Spatial and temporal discretisation schemes are considered, as well as their stability. In both cases, the advantages of using high-order accurate formulations become apparent. Because of their nature, particular attention must be devoted to the boundary conditions of the problem. The treatment of wall boundaries is delicate in this context, and will be investigated in more detail in Chapter 3.

2.1 Equations for acoustic perturbations

It is necessary to find a model for the *mid-field* propagation: between the near-field where the sources of sound reside (close to the turbine blades and the fan), and the zone where the flow is uniform (away from the engine). The objective is to propagate the interaction tone sound, and possibly the N-waves of buzz-saw noise, while including the complex effects caused by non-uniform flows in the transition zone between the internal and the external regions of the engine.

2.1.1 Partition of variables

Essentially, sound consists of the unsteady, propagating perturbations $\boldsymbol{Q'}$ of a quasi-permanent fluid state $\boldsymbol{Q_0}$. The latter is often called the *mean flow*. The unknowns are the density ρ, the velocity components u, v and w, and the pressure p. The total solution $\boldsymbol{Q}$ is then separated as:

$$\boldsymbol{Q} = \boldsymbol{Q_0} + \boldsymbol{Q'} \tag{2.1}$$

Not only is this consistent with the intuitive definition above, but it allows decoupling of the two behaviours, and treating each part with methods best adapted to their intrinsic characteristics. The perturbations often have amplitude of several orders of magnitude less than that of the mean flow quantities, so considering them separately avoids rounding-off errors. This also means that a *linear* approximation is made possible by neglecting terms of second order or more in $\boldsymbol{Q'}$.

In cases of interest for aeroengine acoustic certification, the mean flow is considered steady, and given as an input. This allows a hybrid system, with a traditional CFD program computing the steady flow while the propagation of the acoustic perturbations is computed separately by a CAA code [34].

2.1.2 Nature of the model

The generation of the sound is an area of research in its own right, separate from the propagation. For the problem considered, sound is generated by the complex, often non-linear, interaction phenomena around the fan region outlined in Chapter 1. This can be given by a CFD program, solving the full viscous equations in the near-field region. In this case, to obtain a total design solution, the programs computing the source and the propagation should both run in parallel. This is why a time-domain implementation is chosen for the latter, as in Özyörük's work [9]; this treatment allows multiple modes and frequencies to be considered at the same time. However, frequency-domain models can be very useful to study the propagation of a single mode or frequency once it has been isolated, and the effect of a specific inlet configuration. For example, see the study of Lan, Guo and Bréard [42]. Furthermore, the implementation of porous wall boundary condition is much more straightforward in the frequency domain, as described in Section 2.3.2. On the other hand, a time-domain formulation allows for the possibility of a straightforward implementation of the full non-linear equations, for further extensions (see Section 2.1.4); although there has been recently investigations into non-linear frequency-domain methods [40].

Ray theory provides a good model of high frequency sound propagation [21], but implementing complex geometries is mathematically very complex [22]; furthermore, most of the acoustic energy is contained in the lower harmonics [1, 9].

From now on, as in the majority of similar sound scattering or propagation studies referenced therein, the perturbations $\boldsymbol{Q'}$ are assumed to behave in an inviscid manner. It is possible to consider the effects of viscosity and temperature gradients, but they are not important in most studies of scattering and propagation (except for very long distances, when dissipation becomes apparent). Viscous effects are fundamental in some of the noise generation mechanism, especially from turbulence, like in jet noise studies [7, 43, 44] or broad-band noise effects [1]. In small-scale studies of unsteady vortex-shedding or when unsteady boundary layer effects are important, the viscous terms should be considered, as in Refs. [45] and [24], but this will not be done here. The perturbation equations can however take as input a fully viscous mean flow, without needing to change them [46].

2.1.3 Formulation

The need for a complete model

Many of the existing methods used to predict forward noise propagation from engine inlets use simplifying assumptions that will not capture the more complex wave phenomena induced by the mean flow, aerodynamic/acoustic couplings, *etc.*

When the mean flow is perfectly still, and the acoustics are assumed linear, inviscid and isentropic, the problem can be reduced to a traditional wave propagation problem [47, 48]. This is also true for a uniformly convective flow (constant mean flow velocity $\vec{\boldsymbol{v_0}} = [u_0 \; v_0 \; w_0]$ everywhere), after an appropriate Galilean coordinate transformation [9]. These equations are solved with Green's functions, and an integral representation of the solution can be found, depending only on the time history of the variables on a certain control surface. The sound field at any distance is obtained from a very computationally efficient surface quadrature. This is the basis of the widely used *integral* or Boundary Element Methods (*BEM*), of which Lyrintzis presents a review [34]. There are no dispersion or dissipation errors introduced during the propagation and the accuracy only depends on that of the source.

The Kirchhoff method, modified to allow for a moving control surface [49], is often used to propagate sound to an arbitrary distance in the far-field (for example see Özyörük [9, 36] and Rumsey [29]). The porous surface Ffowcs-Williams Hawking method [50, 51], with the quadrupole source term neglected, is equivalent, but it might be preferable for reasons of reduced sensitivity to the quality and linearity of the input solution. It is also less sensitive to vorticity disturbances, and therefore well adapted to exhaust noise problems [52, 53].

In both cases the control surface must include all regions of sound generation, non-linear behaviour, and inhomogeneous flow. The flow going in the inlet mouth of a typical aero-engine is highly non-uniform, and aerodynamic/acoustic couplings occur: refraction, wavelength modifications or more complex effects. These phenomena are rarely taken into account by analytical or empirical models: it is in those cases that a full computational assessment is most useful.

It is possible to include all these effects while still using the BEM approach: by re-arranging the Navier-Stokes equations, a wave-type equation can be obtained, with the noise generation and flow effects appearing as a source term. This is the basis of the "acoustic analogies", the equations of Lighthill and Lilley and their modifications or simplifications [7, 54]. But a Green's function is still assumed to be found, so this approach can be only used in certain wall-bounded problems, and only for simple mean flows. Lilley's equation has the advantage of separating the mean flow effects from the source term, but, as a third order differential equation, it is difficult to solve numerically. These formulations are mostly used to evaluate noise generated by turbulence.

Many early CAA studies used perturbed potential equations, which assume that the mean flow is irrotational [41, 55]. But this limits the type of input flows that may be used upstream of the fan. Redonnet [46] presents a comprehensive review of more elaborate perturbation equations based on Euler or Navier-Stokes equations. In the light of the current study's objectives, the non-conservative Linearised Euler Equations (*LEE*) will be considered. They are well-suited to the modelisation of the mid-field region [34].

The linearised Euler equations

The inviscid behaviour of small acoustic perturbations ($\boldsymbol{Q'}$) is considered in three dimensions, on top of a stationary mean flow ($\boldsymbol{Q_0}$). Eq. (2.1) is introduced into the non-conservative Euler equations, and all quadratic terms in $\boldsymbol{Q'}$ are neglected. The equations are then arranged in a pseudo-conservative fashion, for reasons of numerical stability [46], by introducing the pseudo-flux vectors $\boldsymbol{E}$, $\boldsymbol{F}$ and $\boldsymbol{G}$. The following is obtained:

$$\text{Let:}\quad \boldsymbol{Q'} = \begin{bmatrix} \rho' \\ u' \\ v' \\ w' \\ p' \end{bmatrix} \quad \text{and:}\quad \boldsymbol{Q_0} = \begin{bmatrix} \rho_0 \\ u_0 \\ v_0 \\ w_0 \\ p_0 \end{bmatrix}$$

$$\frac{\partial \boldsymbol{Q'}}{\partial t} + \frac{\partial \boldsymbol{E}}{\partial x} + \frac{\partial \boldsymbol{F}}{\partial y} + \frac{\partial \boldsymbol{G}}{\partial z} + \boldsymbol{H} = \boldsymbol{S} \tag{2.2}$$

$$\boldsymbol{E} = \begin{bmatrix} \rho_0 u' + \rho' u_0 \\ u_0 u' + \dfrac{p'}{\rho_0} \\ u_0 v' \\ u_0 w' \\ u_0 p' + \gamma p_0 u' \end{bmatrix}, \ \boldsymbol{F} = \begin{bmatrix} \rho_0 v' + \rho' v_0 \\ v_0 u' \\ v_0 v' + \dfrac{p'}{\rho_0} \\ v_0 w' \\ v_0 p' + \gamma p_0 v' \end{bmatrix}, \ \boldsymbol{G} = \begin{bmatrix} \rho_0 w' + \rho' w_0 \\ w_0 u' \\ w_0 v' \\ w_0 w' + \dfrac{p'}{\rho_0} \\ w_0 p' + \gamma p_0 w' \end{bmatrix} \tag{2.3}$$

$\boldsymbol{S}$ represents a possible source term. $\boldsymbol{H} = 0$ if the mean flow is uniform. Otherwise [46, 56]:

$$\boldsymbol{H} = \begin{bmatrix} 0 \\ u'\left(\frac{\partial u_0}{\partial x} - \nabla\vec{\boldsymbol{v_0}}\right) + \frac{1}{(\rho_0)^2}\left(\rho'\frac{\partial p_0}{\partial x} + p'\frac{\partial \rho_0}{\partial x}\right) \\ v'\left(\frac{\partial v_0}{\partial y} - \nabla\vec{\boldsymbol{v_0}}\right) + \frac{1}{(\rho_0)^2}\left(\rho'\frac{\partial p_0}{\partial y} + p'\frac{\partial \rho_0}{\partial y}\right) \\ w'\left(\frac{\partial w_0}{\partial z} - \nabla\vec{\boldsymbol{v_0}}\right) + \frac{1}{(\rho_0)^2}\left(\rho'\frac{\partial p_0}{\partial z} + p'\frac{\partial \rho_0}{\partial z}\right) \\ (\gamma - 1)\left[p'\nabla\vec{\boldsymbol{v_0}} - \vec{\boldsymbol{v'}}\nabla p_0\right] \end{bmatrix} \tag{2.4}$$

2.1.4 Possible extensions

Using conservative variables generally leads to more robust numerical schemes for CFD [46]; however, the author has not encountered a study that directly proves the necessity of such a formulation for the type of applications considered here. Tam [57] notes that they should be used in cases of strong shocks to correctly assess the shock's velocity. In computational acoustics [30], the important metric is the accuracy of the phase and amplitude of the propagated waves, and not the numerical conservation of the variables. Furthermore, with a non-conservative formulation, the equations are expressed in terms of the primitive variables (density, velocity, pressure) [7, 33, 40, 52, 54]. This will allow a direct implementation of the solid wall boundary condition using the pressure values (see Chapter 3).

The partition into mean flow and fluctuations does not imply that the perturbations are small; indeed some researchers have investigated equations where the non-linear terms are retained. Morris *et al.* [58] described the "non-linear disturbances equations", and Long [59] derived a non-conservative formulation. This treatment has many advantages over using the Euler equations for the total variable $\boldsymbol{Q}$: as described above, adapted methods can be used for each part, with a much more efficient result. This is useful because sometimes the propagation is non-linear: high sound pressure levels are often present in aero-engine inlets (more than 160dB). In this case, the small perturbation assumption is not valid, and wave-steepening effects can occur. This is the case for N-waves produced by supersonic fan blade tips (and buzz-saw noise). Also, in cases where the mean flow is highly sheared (such as those found in the aft zone of the engine), neglecting the non-linear effects can lead to instability [54], unless some of the LEE terms are suppressed [52, 56].

A linear scheme is investigated here: this can represent a very good approximation of the propagation of an N-wave if its amplitude has decayed sufficiently. This depends on the point where the mid-field zone is set to start; usually halfway up the inlet is satisfactory. This means neglecting the interaction of the harmonic components of the wave as it progresses. It is probably overall much less computationally expensive to extend the non-linear CFD region up to the right point than to perform a full non-linear treatment of the propagation. Not only must the non-linear terms be added to the equations, and conservative variables used, but also specific shock-capturing schemes are needed to handle the discontinuities of the solution, as will be explained in Section 2.2.1.

2.2 Literature survey: spatial and temporal discretisation

The chosen set of acoustic equations must now be discretised, in order to solve it numerically. The inefficiency of traditional CFD codes in propagating sound over several wavelengths will be illustrated with a simple example in the following pages. Using very fine grids with a traditional, low-order scheme, to obtain the accuracy needed for acoustics computations, is impractical, so the choice of integration scheme is really important. There is now a large body of work [30, 31, 33, 60, *etc.*] showing that high-order accurate discretisations capture the waves much more accurately, for a lower overall computational effort.

Some commonly used methods will be reviewed. Several workshops on benchmark computational acoustics problems have provided a very interesting platform for the direct comparison of different methods, and their resolution of several typical CAA problems [33, 60, 61].

Intuitively, using a low-order discretisation is equivalent to building a solution with a piecewise linear function; this is badly suited to the oscillating nature of acoustic signals. High-order methods use more elaborate representations, which are more appropriate for these problems, hence their efficiency. One problem is that unless filtering or dissipative mechanisms are used, instability will occur next to discontinuities because of the creation of spurious high-frequency waves. This is similar to Gibb's phenomenon, which occurs when trying to approximate a discontinuous function with a truncated Fourier series [62].

2.2.1 Spatial discretisation

Overview

The crucial part of the numerical treatment resides in the *spatial* discretisation of the equations. Many different methods are adapted for this purpose, and some well-known methods have been re-designed specifically for CAA purposes. They will be examined in this study, considering that a computationally economic 3-dimensional method is needed, to replace low-order CFD schemes.

A good metric to characterise how efficient the scheme performs is the number of Points-per-Wavelength (PPW) required to propagate sound accurately over several wavelengths, allowing a certain maximal error in phase (**dispersion**) and amplitude (**dissipation**).

Rumsey *et al.* [29] refer to results indicating that the CFL3D code, from NASA Langley Research Center, needs resolutions of around 25 PPW in each spatial direction to propagate sound correctly in the near-field. This is typical of traditional, low-order CFD codes, and even more would be needed to cover longer distances. Lockard [63] shows that, to have less than 10% relative phase and amplitude error, for a propagation over 20 wavelength, a second-order central difference scheme needs 91PPW. He also points out that, for a given distance, increasing the frequency leads to surprisingly large PPW requirements because it represents a propagation of several more wavelengths, which requires even more stringent criteria to avoid numerical errors.

A simple study of propagation using a low-order discretisation was made using the AU3D code described in Section 1.2.2. Originally designed to study aero-elasticity in axial turbomachinery, it can model many viscous or inviscid fluid mechanics problems, and has been used successfully in some low-frequency acoustic cases [17, 18]. A simple plane wave, of wavelength $\lambda = 49$ cm, is imposed at one end of a hexahedral 3D domain, of dimensions 10 m×1 m×1 m, to propagate along the $\vec{x}$ axis in the negative direction. On half the domain (x from 0 to -5 m), the grid is fine, with uniform grid spacing along $\vec{x}$ of size Δ, and 15 grid-points in both the $\vec{y}$ and $\vec{z}$ directions. In the rest of the domain (x from -5 m to -10 m), the grid becomes increasingly stretched in the x direction to prevent artificial reflections, as shown in Fig. 2.1.

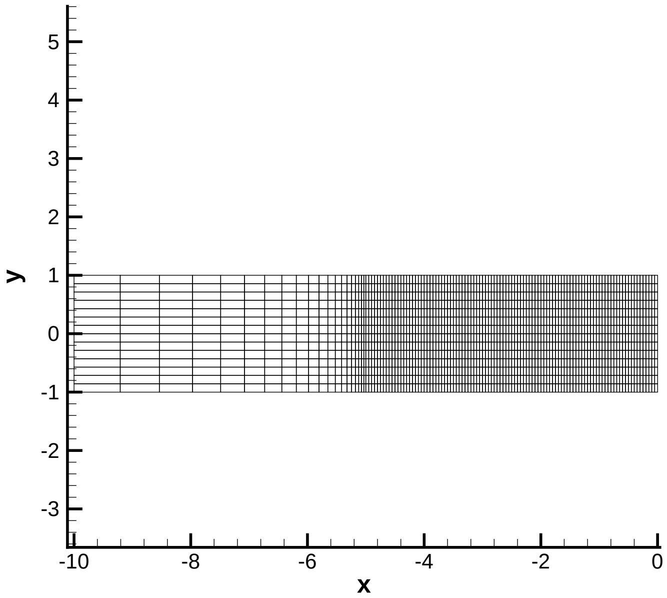

Figure 2.1: 2D slice (constant z plane) of the grid used to model plane wave propagation, shown here for the 10 PPW resolution.

The mean flow is considered at rest. A symmetric boundary condition is imposed on all boundaries parallel to $\vec{x}$, and the two other boundaries have 1-D non-reflecting boundary conditions using a characteristics method, which allows the imposition of an incoming wave at $x = 0$. It was decided, after numerical tests, to use 150 time steps per oscillation period, and the computation was done for 10 wave periods. The acoustic pressure $p' = p - p_0$ is computed, for different resolutions: a very fine grid with $\Delta = 0.6$ cm, which is nearly 82 PPW, then $\Delta = 1.667$ cm or around 30 PPW, and $\Delta = 5$ cm which represents 10 PPW. As with all following AU3D results, p' is non-dimensional, normalised by a reference pressure of $p_{ref} = 10000$ Pascals. The resulting acoustic pressure, along the centerline, is shown in Fig. 2.2, along with an exact solution.

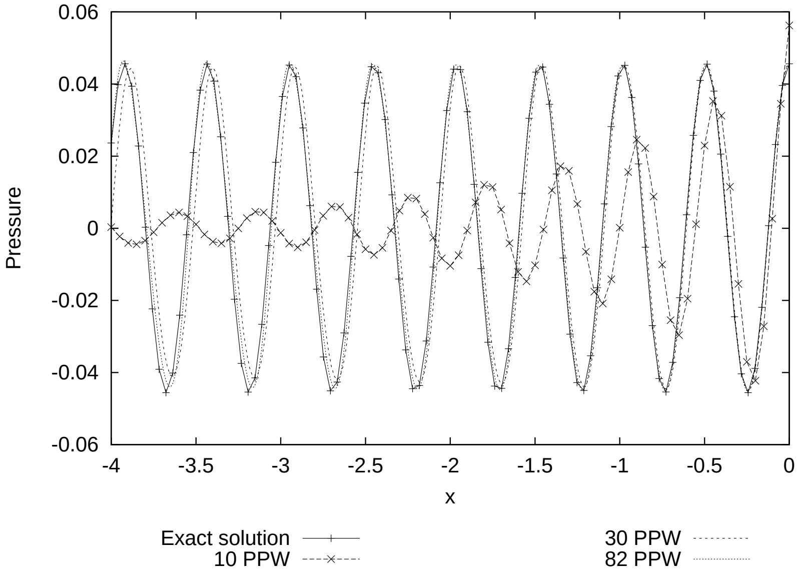

Figure 2.2: Plane wave computation with a low-order scheme.

The results very clearly show the strong numerical dissipation and dispersion that arise when a coarse mesh is used. For 10 PPW the wave is very quickly damped and becomes more than half a wavelength out of phase. Even when the wave is not strongly dissipated (30 PPW), an increasing phase error appears as the wave propagates (up to 6% of the wavelength): as Lockard pointed out, dispersion errors are much more important than dissipation ones for low-order discretisations [63]. Using even 30 PPW is impractical in demanding aeroacoustics cases, where the Helmholtz number $\bar{\alpha} = \alpha a = 2\pi a/\lambda$ can go up to 20 or more (where a is a length scale of the problem, for example the duct radius, and α the wavenumber).

It is therefore necessary to investigate more efficient methods for realistic CAA computations. Typically, high-order methods permit using less than 10PPW, and even with this resolution, large problems remain quite a challenge. When directly computing the noise generated by turbulence, for example from LES computations, a very high level of accuracy is needed to resolve the length-scales all the way to the limits of the sub-grid model; this means typically a 7^{th} order or more scheme capable of resolving 4 PPW [64, 65]. But in this project, the objective is to get overall more efficiency than a low-order scheme; a good compromise seems to be around 7 to 10 PPW.

The order of accuracy can be raised by increasing the number of points used to compute the derivative, or by using, in an implicit fashion, the values from neighbouring points. Another approach is to construct the solution using more complex and appropriate "test" functions. These methods introduce many mathematical, algorithmic and numerical difficulties, and the resulting schemes are often less robust than their low-order counterparts, so careful work is needed.

Commonly used schemes (as summarised in Fig. 2.3) will now be reviewed:

Explicit finite difference: this is the most straightforward formulation, based on a truncated Taylor series. To extend the order of accuracy, more points are included in the derivations stencil [25]. However, the resulting extended stencils can be the source of many new algorithmic difficulties, near boundaries mostly. They also prohibit the use of unstructured meshes. Those schemes will be described in more detail below.

MacCormack schemes: integrate equations both in space and time using an extended asymmetric stencil and a predictor-corrector method. High-order accurate versions were used in early CAA applications [66], but they were found to perform less well than some finite difference methods [67], and they are not commonly used in recent CAA applications.

Compact scheme: an implicit finite difference scheme. The derivative at each point is expressed proportionally to the derivatives on the immediately neighbouring points [68]. After solving the resulting tridiagonal linear system, a very accurate representation is obtained (even for resolutions as low as 4 PPW). Furthermore, a 3-point stencil can be used, hence the name. This means that meshing techniques used with low-order schemes can be retained, and the algorithmic

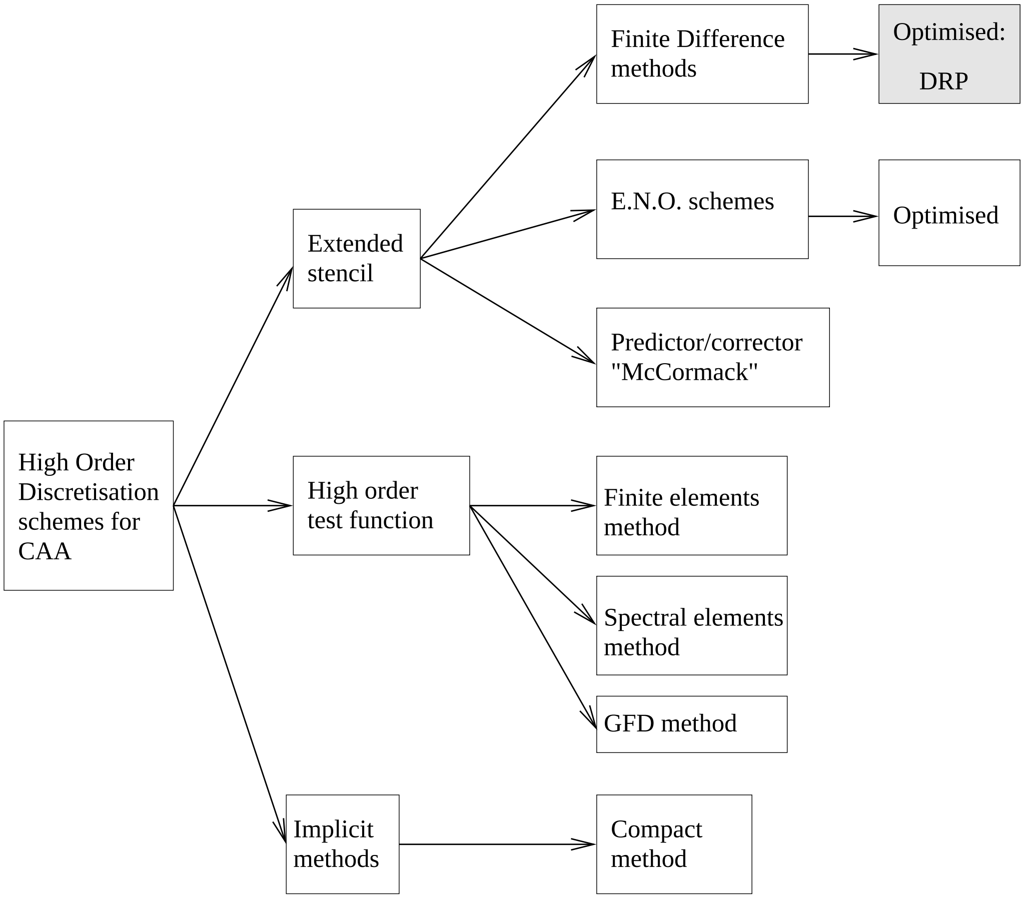

Figure 2.3: Popular high-order accurate spatial discretisations for CAA. In grey, chosen scheme for this study.

difficulties associated with large stencils are avoided. This type of scheme has been used with success to model downstream propagation in axisymmetric engine noise problems [52]. However, inverting the tri-diagonal matrix comes at a computational cost; Redonnet showed that using implicit finite difference is 2.5 times more costly, per spatial direction, than a similar explicit scheme, and that, for a given frequency, the marginal gain in PPW used does not compensate this [46]. So, in 3D cases, when the grid is not fixed but a specific wavelength must be resolved, an explicit scheme will be more computationally efficient, and should be used unless the problems introduced by large stencils are deemed to be more important.

Essentially Non-Oscillating (*ENO*) methods: specifically designed to represent shocks and discontinuities accurately; by reverting to a low-order approximation of the solution near them, while retaining a high-order accuracy in most of the domain [69], they avoid the oscillations associated with other high-order schemes. They have been specifically adapted for use in CAA [63, 70], and recently, more accurate "weighted" formulations have been developed [71]; but flux-splitting and an evaluation of the solution is required at each point in order to build an appropriate reconstruction polynomial, and this will come at a certain computational cost [30].

Finite or spectral elements: such elements are popular in CFD because they lead to robust and compact schemes that can be used, with finite volume formulations, to discretise complex geometries using unstructured grids [25]. It is possible to obtain a high-order accuracy with such schemes by increasing the order of the test functions inside each element. For example, wave envelope methods were widely used in early CAA studies [9, 55, 72]. But implicit finite element methods are computationally expensive to extend to 3D because of the quadrature process, resulting in large matrices that are very costly to invert [9]. There is however ongoing research on quadrature-free methods [73], and explicit methods such as the discontinuous-Galerkin techniques are increasingly popular.

The spectral-element method supersedes traditional spectral methods, which were only capable of handling simple geometries [37, 74]. Highly accurate acoustic scattering computations are then possible [37,38,75]. Stanescu [39] uses a parallelized spectral element code to compute the 3D scattering of tone noise by an airplane's engine inlet and wing. Difficulties with traditional tetrahedral-based unstructured grids has led to the development of spectral/hp element methods [76].

Other methods: The GFD scheme is a recently developed method that uses Green's functions, local solutions of the wave equation, as test functions for the discretisation [77]. By writing compatibility equations for all the points in the domain, a unique solution is found. Because the test functions are so well adapted to the problem, the resolution can be as low as 3 PPW. There is an ongoing research effort to adapt this scheme for inlet wave propagation problems [78].

The CIP scheme [79], developed for convection problems, seems very adapted, but its efficacy in a CAA context has not been evaluated yet.

Scheme choice

In this work, it was decided to assess the use of an **explicit finite difference scheme**. Computational efficiency is crucial, since the goal is to compute propagation in the mid-field faster than low-order schemes with a very fine resolution. Compact and implicit finite element methods were excluded, as they generally become relatively more expensive when extended to 3D. Finite difference schemes are associated with structured methods, and a uniform grid, with good resolution characteristics, can be retained in the whole domain. In the next chapter this approach will be explained in more detail, based on the fact that grid quality considerations become crucial for high-order accurate CAA problems. Finite difference schemes appear efficient and versatile [33,60], and it is the main technique used for many complex, demanding 2D [8,42,54,80] and 3D models [7,9,35,43,53,58].

The first derivative of a function f along the x axis is expressed, at a point x_0, as [25]:

$$\frac{\partial f}{\partial x}(x_0) \simeq \frac{1}{\Delta x}\sum_{j=-3}^{3} a_j f(x_0 + j\Delta x) \tag{2.5}$$

for a 7-point stencil. The a_j coefficients are determined through a Taylor expansion by specifying the order of the truncation error (in this case $\{a_j\} = \{-\frac{1}{60}, \frac{3}{20}, -\frac{3}{4}, 0, \frac{3}{4}, -\frac{3}{20}, \frac{1}{60}\}$).

Finite-element treatment of fully 3D CAA problems can be computed more easily thanks to parallel computation, for example see Ref. [39]. Finite difference schemes can also be sped up in the same way: this was studied in detail by Özyörük [9]. Morris and Shieh [81] computed a 3D scattering test problem using the following method: the hexahedral domain is separated in “slices”, each of which is assigned to a different processor. Both of these studies show that the computations scale well with the number of processors.

Optimised finite difference

In the context of acoustic applications, it is more illuminating to examine the wavenumber resolution characteristics of the scheme instead of focussing on the order of the truncation error [31, 32, 46, 68]. A Fourier transform of Eq. (2.5) can be used to show when the theoretical wavenumber α differs from the computed one $\bar{\alpha}$ [32]:

$$\alpha \simeq \frac{-i}{\Delta x} \sum_{j=-3}^{3} a_j \, e^{ij\alpha\Delta x} = \bar{\alpha} \tag{2.6}$$

If the group velocity c_g is not accurately resolved, then the waves will be predicted to propagate at the wrong speed. This means that the slope $\frac{d\bar{\alpha}}{d\alpha}$ also has to be very accurate [30]:

$$\frac{d\bar{\alpha}}{d\alpha} = \sum_{j=-N}^{M} j a_j \, e^{ij\alpha\Delta x} \simeq 1 \tag{2.7}$$

A significant resolution gain can be obtained by designing the a_j coefficients for an optimal accuracy over a certain wavenumber range, by relaxing the order constraint. More specifically, the widely-used “Dispersion-Relation Preserving” (*DRP*) scheme [30, 32] is employed in this study. It is a 7-point stencil method, optimised over a certain range, while only being formally 4^{th}-order accurate in terms of truncation error. The range is usually taken to be $|\alpha\Delta x| \leq 1.1$ after some researchers [57, 63] pointed out that the initial range of $|\alpha\Delta x| \leq \pi/2$ [32] was too stringent. The resulting coefficients can be found in Ref. [30]. Resolutions as low as 7 PPW can be used, while still obtaining a better representation of the wavenumber than with a standard 9-point stencil, as can be seen on Fig. 2.4. Using a similar but non-optimised scheme can lead to the need for 12 PPW [36], which represents a large increase in computational cost, especially for large 3D problems.

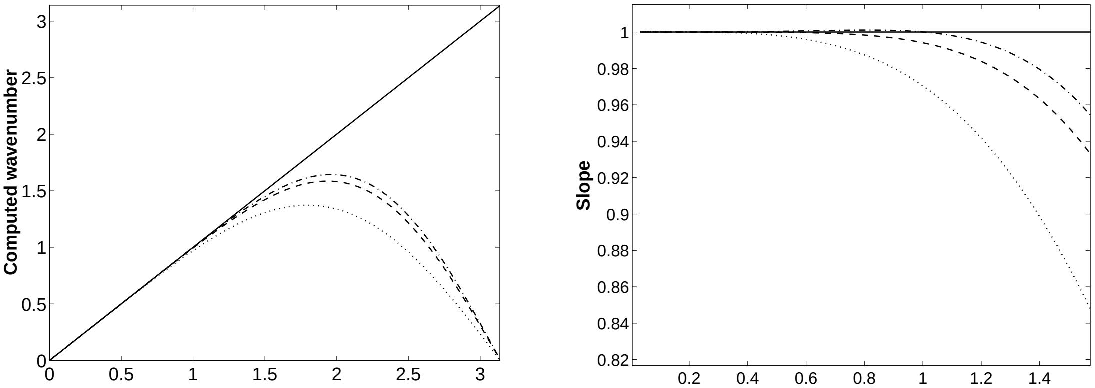

(a) $\bar{\alpha}\Delta x$ versus $\alpha\Delta x$.

(b) Slope $\dfrac{d\bar{\alpha}}{d\alpha}$ versus $\alpha\Delta x$.

Figure 2.4: Comparison of different finite difference schemes. — : exact solution, $\cdots$: standard 4^{th} order, $- - -$: 6^{th} order, $- \cdot -$: DRP scheme.

Because of its symmetric stencil, this finite difference scheme has no intrinsic dissipation. But, as was pointed out earlier, near discontinuities of any kind, spurious short waves, unresolved by the scheme, can appear and contaminate the solution[1]: this leads to instability and a failure of the computation. This can be controlled by adding dissipative terms that only suppress high-frequency waves: what is called "*artificial selective damping*" [30]. This technique is effective, and has been used in most applications of the DRP scheme. The amount of dissipation is controlled by a mesh Reynolds number R_Δ, as described in Section 2.2.4. Tam and Shen [57] even used a modified, pressure-sensitive version to compute

---

[1] This is because the fourth order finite difference method assumes solutions that are at least of class $\mathcal{C}^4$ (*i.e.* continuously differentiable 4 times). Alternatively, this can be seen as the scheme failing to resolve high-frequency components of the solution.

shocks [8] without resorting to a dedicated scheme such as the ENO. This success points towards a possible computation of non-linear steepening or N-waves, without the computational effort associated with shock-capturing methods.

Another approach is to modify the DRP scheme to make it inherently more stable; for example: through a staggered-grid approach [82], or by upwinding [83].

Boundaries

The extended stencils cause problems near outer or wall boundaries, where they cannot overrun. Instead of using smaller stencils, large 7-point, asymmetric *shifted* stencils can be used in the boundary region [30]. For 7-point stencils, this region is 3 mesh-point thick, as shown in Fig. 2.5. The following derivation will show that this treatment is still high-order accurate, but introduces some instability which will need to be suppressed.

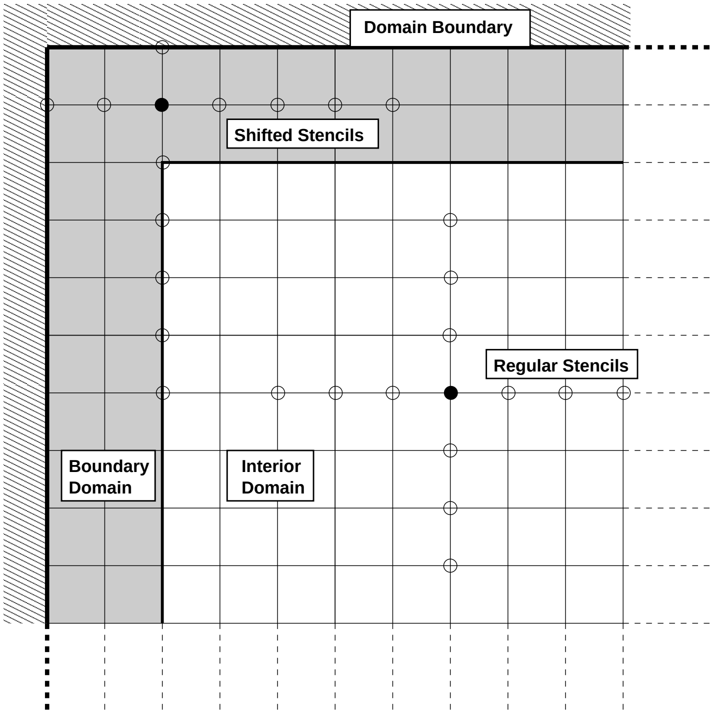

Figure 2.5: Representative shifted finite difference stencils in a corner region.

The numerical dispersion error is determined by the difference between the real group velocity $c_g = c_0$ of the waves, as given by the original equations, and the effective computed one $\bar{c_g}$ [30]. The latter is obtained from Eq. (2.7) as:

$$\bar{c_g} = c_0 \frac{d\bar{\alpha}}{d\alpha} \tag{2.8}$$

After a time t_p, this represents an error in position of $\delta x = (\bar{c_g} - c_0)t_p$. If a wave is propagated for a distance of N grid points, the non-dimensional error on the position $\overline{\delta x}$ is equal to :

$$\overline{\delta x} = \frac{\delta x}{\Delta x} = N\left(\Re\left(\frac{d\bar{\alpha}}{d\alpha}\right) - 1\right) = N\left(\Re\left(\sum_{j=-N}^{M} j a_j \, e^{ij\alpha\Delta x}\right) - 1\right) \tag{2.9}$$

A good criterion for the accuracy of numerical propagation would be that $\overline{\delta x} < 1$ (one grid length), in a given wavenumber range.

The numerical error induced by the shifted stencils will be evaluated for a simple 1D model of a wave reflecting off a wall, as represented in Fig. 2.6. For the sake of this derivation, the reflection is considered perfect, as the wall boundary condition will be considered in Chapter 3. Appropriately shifted stencils must be used close to the wall, as in Fig. 2.5. $\overline{\delta x}$ is computed for a total propagation of N grid points, with a wavenumber $\alpha = 2\pi/\lambda$ (case A). For comparison, the same calculation is made using smaller, non-optimised stencils, which are shortened instead of being shifted, using 4, 5 and 6 points (case B). It is also interesting to compute, as reference, the numerical error for a free-field propagation over N points, without any shifted stencils, for several schemes: the DRP first (case C), then standard 4^{th} (case D) and 2^{nd} (case E) order schemes.

As can be seen in Figs. 2.7 and 2.8, and in Table 2.1, the accuracy remains of high order for the wavenumber range of interest ($\alpha\Delta x < 1.0$ which is 6 PPW or more). $\overline{\delta x}$ remains under 1, which represents a dispersion error of less than one grid-length, while the low order schemes introduce significant errors even for large wavelengths. Using the smaller shifted stencils appears to lower the accuracy close to the 4^{th} order curve, and push $\overline{\delta x}$ over 1, which proves the importance of using large shifted stencils. It is however clear that the shifted stencils introduce

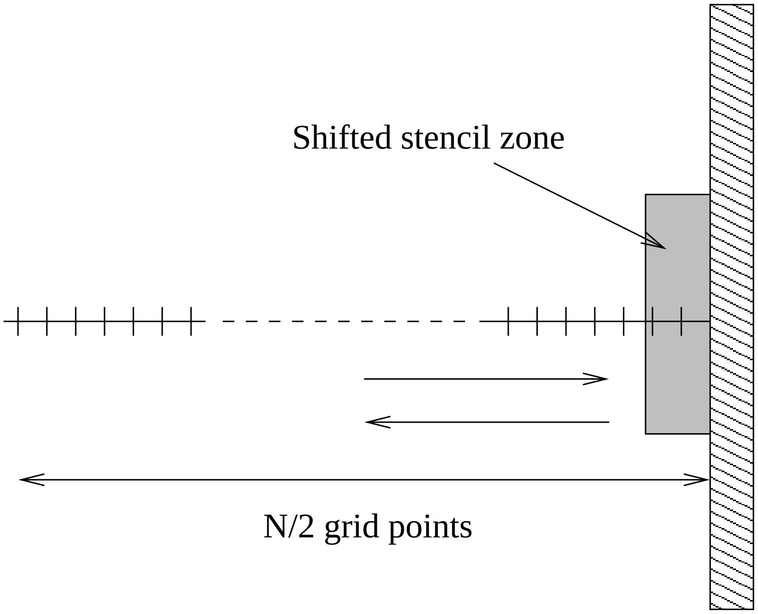

Figure 2.6: Schematic of shifted stencil accuracy derivation.

a higher error in the high wavenumber range ($\alpha\Delta x > 2.5$), and this can lead to numerical instability [84]. This instability comes from the asymmetric nature of the shifted stencils, and indicates the need for increased artificial selective damping next to the boundaries, to damp out the spurious short waves which are created [30].

α	N/λ	$\overline{\delta x}$: Case A	Case B	Case C	Case D	Case E
$2\pi/7$	6.43	0.53	1.39	0.14	4.25	16.94
$2\pi/10$	4.5	0.22	0.57	0.12	1.09	8.59
$2\pi/15$	3	0.02	0.14	0.04	0.22	3.89

Table 2.1: Non-dimensional dispersion error $\overline{\delta x}$ with N=45

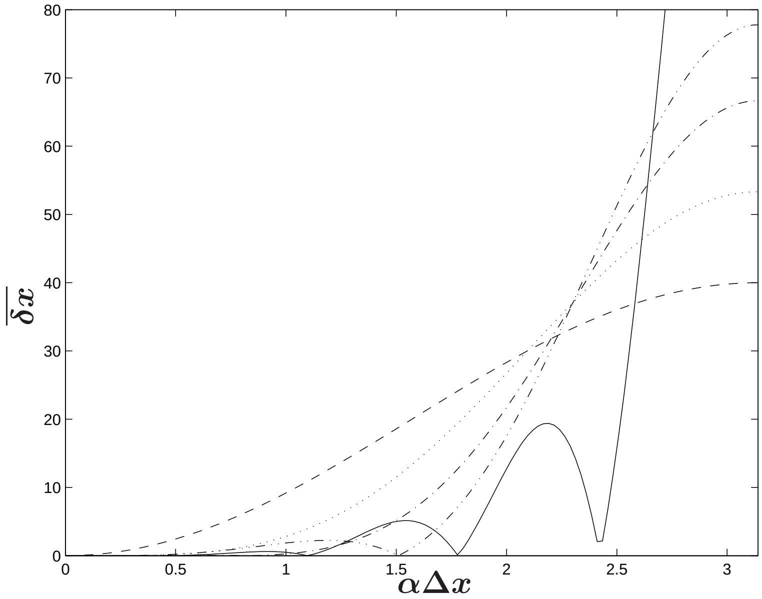

Figure 2.7: Non-dimensional dispersion error $\overline{\delta x}$ with N=20. Solid line: case A, - ·· -: case B, - · - -: case C, · · ·: case D, - - -: case E.

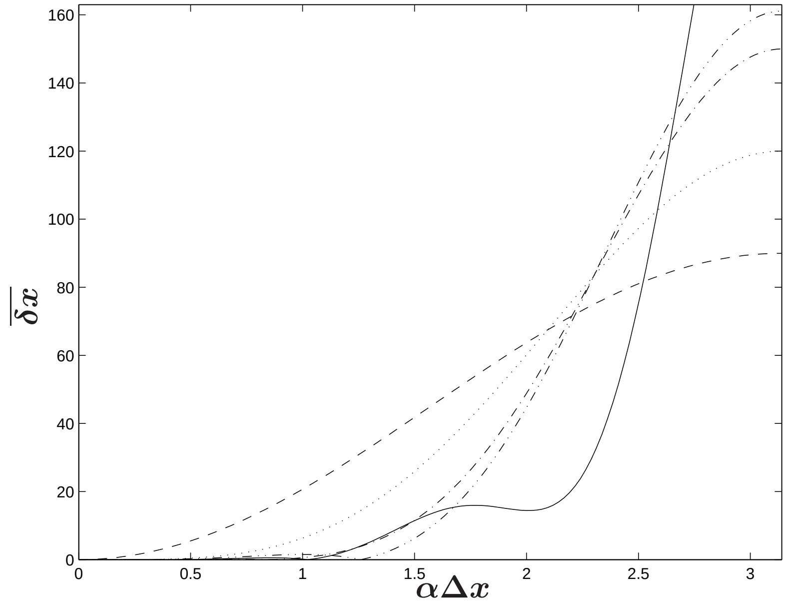

Figure 2.8: Same as Fig. 2.7, with N=45.

Inhomogeneous Grid

The finite difference scheme, in its basic form, requires a structured, uniform and orthogonal Cartesian grid in the whole domain. Even disregarding the problem of including wall boundaries, which will be discussed in Section 3.1.1, in some cases a range of different length scales is present throughout the computational domain. For example, when strong flow inhomogeneities are present, some areas will carry shorter acoustic wavelengths because of local Doppler effects. There are also strongly local viscous effects with boundary layers: using local grid refinements would be very efficient. It is then possible to have patched zones of different grid densities, while preserving a basic DRP scheme in each one of them by using a multiple-size mesh/multiple time-step method as investigated by Tam and Kurbatskii [85] and further by Berland [65]. It represents a very efficient scheme, as the time-marching is adapted to the grid-length in each zone. These issues will not be investigated in the current work, but it is worth noting that a finite difference approach does not prevent from dealing with them.

2.2.2 Temporal discretisation

Using a spatial scheme results in a discretised equation of the form

$$\frac{\partial \boldsymbol{Q'}}{\partial t} = \mathcal{F}(\boldsymbol{Q'}) \tag{2.10}$$

which needs to be advanced in time. The right-hand side vector $\mathcal{F}$ is often called the "residual". Here as well, a high level of accuracy is needed to efficiently represent the oscillatory nature of the acoustic signals. Except for the low-frequency range [86], explicit methods are best suited to solve Eq. (2.10) because the time step is restricted by accuracy, and not stability constraints, as will be explained in the next section.

There are two main methods used in CAA, both described in detail in Ref. [46]: Adams-Bashforth finite-difference type schemes, and the Runge-Kutta methods. Both types of schemes have been optimised for acoustics applications, for maximum accuracy in the frequency domain, similar to what was done for the DRP scheme.

The Optimised Adams-Bashforth (*OAB*) four levels time-marching scheme was described by Tam and Webb [32]. It uses, at the time level n, the residual values of the 3 preceding time steps:

$$\boldsymbol{Q'}^{n+1} = \boldsymbol{Q'}^{n} + \Delta t \sum_{j=0}^{3} b_j \, \mathcal{F}(\boldsymbol{Q'}^{n-j}) \tag{2.11}$$

where Δt is the time step chosen, and b_j are the optimised coefficients. This means that the three previous values of the residual need to be stored in memory.

A linearised version of the Runge-Kutta algorithm allows a low-storage implementation, while retaining its accuracy for linear problems. Hu *et al.* [87] designed optimised versions of these algorithms: "Low-Dissipation and -Dispersion Runge-Kutta" (*LDDRK*). If s is the number of Runge-Kutta stages, at each time step the quantities

$$\boldsymbol{K}_j = \Delta t \; \mathcal{F}(\boldsymbol{Q'}^{n} + \beta_j \, \boldsymbol{K}_{j-1}) \tag{2.12}$$

for $j = \{1 \ldots s\}$ are computed (with $\beta_1 = 0$). The optimised $\{\beta_j\}_{j=2 \ldots s}$ coefficients can be found in Ref. [87]. Then the final step is:

$$\boldsymbol{Q'}^{n+1} = \boldsymbol{Q'}^{n} + \boldsymbol{K}_s \tag{2.13}$$

In this study, $s = 4$ and $s = 5$ will be used. The unused $\boldsymbol{K}_j$ can be overwritten, so only two levels of storage are needed. For large 3D problems this might provide a significant gain. It should be noted that Stanescu [88] and Berland [65] have studied similar schemes that retain their high accuracy for non-linear problems.

The LDDRK integration has greater stability, lower memory usage and higher resolution than the modified Adams-Bashforth scheme, but needs s computations of the equation residuals per time step, whereas the latter only needs one. So, compared to the scheme above, this will *a priori* represent a gain in computational time only if the greater stability and accuracy allow time steps more than s times larger.

2.2.3 Stability

In this subsection, both the temporal and spatial discretisation are combined. For a uniform underlying flow, Redonnet [46] shows that once the scheme is space-accurate and time-accurate, the overall solution is accurate and the evolution of the variables in time will give the correct solution. In other words, if the wavenumber and the frequency are well approximated, then the wave will be correctly simulated.

The combinations of the optimised Adams-Bashforth and the LDDRK schemes with the DRP scheme are studied respectively in Refs. [32] and [87]. A theoretical study of their resolution of the simple one-dimensional wave equation is made: this gives an indication of their performance and stability. For the whole range of wavenumbers *represented* by the DRP scheme ($\overline{\alpha}\Delta x < 1.65$, *cf.* Fig. 2.4(a)) the temporal integration is *st*able if the time step is smaller than a certain value Δt_{st}. But in both cases, a smaller time step Δt_{ac} is needed for an *ac*curate evaluation of the frequency for the range of wavenumbers *resolved* by the scheme (7 PPW or more). Δt_{ac} is calculated by allowing, for the first scheme, a maximum error on the amplitude of 0.5dB for a propagation of 100 mesh spacings, and, for the LDDRK, a 10^{-3} maximum relative error for phase and amplitude.

The computed values of those limits are presented in Table 2.2. M represents the Mach number of the convective flow, if present. For the OAB scheme, the derivation of Ref. [32] was modified to take into account the new wavenumber optimisation range of ±1.1 (*cf.* Section 2.2.1). The limits of the LDDRK scheme are given in Ref. [87] as function of the the Courant-Friedrichs-Lewy number CFL= $c(1+M)\Delta t/\Delta x$. To compare how effective the different schemes are, the accuracy limit is divided by the number of stages s, which gives the number of residual evaluations per time step.

It is clear that the *accuracy constraint* on the time step ($\Delta t < \Delta t_{ac}$) is more demanding than the *stability constraint* ($\Delta t < \Delta t_{st}$) [9]. The large time steps allowed by implicit methods will not be needed, which justifies the choice of explicit time-marching. Furthermore, implicit methods have a larger computational cost, and often introduce a large numerical distortion for large time-steps [9].

In theory, to resolve a given wavenumber, all other considerations being equal,

M	Time integration Scheme	Δt_{st}	Δt_{ac}	$\Delta t_{ac}/s$
0	Optimised A.-B.	0.17	0.1	0.1
	4-stage LDDRK	1.73	0.73	0.18
	5-stage LDDRK	2.15	1.16	0.232
0.5	Optimised A.-B.	0.13	0.06	0.06
	4-stage LDDRK	1.15	0.49	0.12
	5-stage LDDRK	1.43	0.77	0.154

Table 2.2: Maximum time steps, using the DRP spatial scheme, to have stability and sufficiently low dispersion/dissipation.

the 4 stage Runge-Kutta scheme will be overall twice as effective as the OAB scheme. But if the time-step is restricted, for any reason, below 4 times the Δt_{ac} of the OAB scheme, using the LDDRK method leads to a higher overall computational time, so it should not be used, unless the memory saving is a more important consideration. In the following chapters, this is the case when spurious, unresolved short waves contaminate the solution when the curved wall boundary condition is used: smaller time steps are needed. Great care must be taken to suppress those waves next to any discontinuity or sudden change.

2.2.4 Implementation

The variables are non-dimensionalised according to the following parameters: length scale $\Delta x = \Delta y = \Delta z$, time scale $\frac{\Delta x}{c_0^\infty}$, velocity scale c_0^∞, pressure scale $\rho_0^\infty {c_0^\infty}^2$, density scale ρ_0^∞. The ∞ symbol refers to upstream, undisturbed quantities. This leads to identical LEE equations for the non-dimensional quantities [46]. From now on, unless specified otherwise, numerical results will refer to the non-dimensional quantities.

The resulting LEE equations, Eqns. (2.2)–(2.4), are discretised using the DRP spatial scheme, Eq. (2.5), on a uniform Cartesian grid. They are then integrated in time using either of the explicit schemes described in Section 2.2.2: Eq. (2.11) or Eqns. (2.12)–(2.13).

The artificial selective damping is implemented by modifying the residual equation (2.10) at point l, for the spatial direction x, by adding a dissipative term [30]:

$$\frac{\partial \boldsymbol{Q_l}'}{\partial t} = \mathcal{F}(\boldsymbol{Q_l}') - \frac{c_\infty}{\Delta x R_\Delta} \sum_{j=-3}^{3} d_j \, \boldsymbol{Q'_{l+j}} \tag{2.14}$$

with the artificial Reynolds number R_Δ controlling the amount of dissipation. The same is done for y and z. As Tam and Shen showed [57], although this is designed to eliminate the spurious short waves, there will still be a small effect on the frequencies of interest, and at length this might affect the quality of the solution by adding some numerical dissipation and dispersion. Therefore the amount of dissipation must be chosen as low as stability will allow. A low background value (typically $R_\Delta = 0.01$) is used in the whole domain, adding a Gaussian distribution (typically of amplitude $R_\Delta = 0.15$ and half-width 8) near the edge of the computational domain [33, 60].

2.3 Boundary conditions

Boundary conditions are a very important aspect of CAA problems, because they need to have the same high fidelity as the numerical schemes used to solve the problem in the main domain [30, 68]. Additionally, any error or spurious reflection will propagate in the main domain with little dissipation. There is often no universal solution functioning in every case, although a large amount of research is done in this area. The external boundaries must be able to let outgoing waves exit the computational domain, and, because of the engine geometries being studied, the modelling of solid walls and of the in-duct interface must also be considered.

2.3.1 Sound radiation

It is particularly crucial to implement the Sommerfeld condition: outgoing wave radiating towards infinity. Numerical simulations need to be run on a finite domain, but the outer limits must be transparent to outgoing waves, as if the domain extended to infinity. If wrongly expressed, artificial reflections occur at the boundaries. In the case of finite element methods, infinite elements [38, 55] can provide an appropriate boundary treatment. Otherwise, three main approaches are found in the CAA literature [30]:

Characteristics analysis is a popular approach in traditional steady-state CFD, rarely used in CAA investigations. It uses the propagational speed eigenvalues of the governing equations near the boundary (see Thompson [89] or Giles [90]). In practice, it is seldom used in a fully 3-dimensional implementation, and this can cause significant reflections when waves are not exactly normal to the boundary [9, 30].

Absorbing boundary layers prevent reflections by damping out any wave reaching the boundary. This can be done by stretching the grid in a "sponge zone", or by progressively reducing the order of the spatial discretisation (Redonnet [46]). But this can create instability, and introduce low-frequency, parasite waves. A suitable progressive damping can be introduced: Bogey [7]. Zhang [52] implemented a similar "buffer zone", using an explicit damping formulation, as did Stanescu [37, 39].

Another method in this category is the Perfectly Matched Layer (*PML*) [91]. This method, developed for computational electrodynamics, consists of adding, in the absorbtion zone, a dissipative term to the main equations after they have been split along all spatial directions. It avoids reflections at the interface by matching the eigensolutions in both domains. It has been used in many applications, for example Ref. [43]. However, Tam *et al.* [92] among others have shown that in certain cases in which the main flow is normal to the boundary, instability phenomena can generate parasite waves. Particularly, inside a duct with non-zero flow, the PML condition can actually amplify waves. There is an ongoing research on how to transform the PML equations to obtain unconditional stability, even for non-trivial mean flows [93].

Asymptotic boundary conditions: presented by Bayliss and Turkel [94], and Tam and Webb [32], they assume that the boundaries are far enough from all sources of sound (in the center of the domain) for an *asymptotic* form of the equations to be used. They were later extended to non-homogeneous mean flows by Tam and Dong [95]. It is also possible to formulate a non-linear version of the asymptotic conditions, as done by Tam and Shen [8].

They are fully three-dimensional, and were found to be efficient in many applications [7, 9, 33, 35, 96] with less than a few percent reflections at most. They come in two forms: "radiation" and "outflow", with the former allowing acoustic waves to exit, while the latter is found downstream of the mean flow in cases where convected entropy and vorticity modes of excitation need to exit as well. The 3D formulation of the radiation condition is given by Bogey [7] as:

$$\frac{1}{\bar{c_g}}\frac{\partial \boldsymbol{Q'}}{\partial t} + (\frac{\partial}{\partial r} + \frac{1}{r})\boldsymbol{Q'} = 0$$

$$\text{With:} \quad \bar{c_g} = \vec{\boldsymbol{v_0}}.\vec{e_r} + \sqrt{c_0^2 - (\vec{\boldsymbol{v_0}}.\vec{e_\theta})^2 - (\vec{\boldsymbol{v_0}}.\vec{e_\varphi})^2} \tag{2.15}$$

where r is the radial distance and $(\vec{e_r}, \vec{e_\theta}, \vec{e_\varphi})$ the unit vectors of the spherical coordinate system centered in the approximate location of the sources.

The efficiency of this asymptotic approximation depends on the distance between the sources of sound and the boundaries, although Tam and Webb [32] show that they still give good results if the source is 20 grid-lengths from the boundary. Using a larger domain leads to an increased computational effort, so for certain problems, absorbing boundary conditions might be more efficient in that respect [43, 91]. One solution would be to combine an asymptotic treatment with a damping layer, as it was necessary to do in some jet noise cases, where strong vortical disturbances are convected downstream [7, 96]. Some instability problems for long-time integration have also been reported [37], due to the spurious waves created by the presence of the boundary, but this can be remedied by the use of artificial selective damping [30]. In the following, the asymptotic radiation condition will be implemented.

2.3.2 Solid walls

Since the perturbations are assumed to be inviscid, the slip boundary condition needs to be enforced close to the wall. If the normal direction is indicated by $\vec{\eta}$, the condition is:

$$\vec{\boldsymbol{v'}}.\vec{\eta} = \frac{\partial p'}{\partial \eta} = 0 \tag{2.16}$$

The difficulties involved in numerically enforcing this condition will be examined in Chapter 3.

As described in Section 1.1.2, using porous, absorbing walls is a major technique of noise reduction. These liners can be modelled by a frequency-dependant impedance, often obtained experimentally. This makes their implementation in time-domain schemes difficult. Popular approaches include using z-transforms [35], differential equations [97] or a 1D model of the liner cavity [98]. Because of time constraints, none of these has been implemented in the current work, but the wall boundary condition described in chapter 3 will be assessed for compatibility with these models.

2.3.3 In-duct boundary condition

An important problem is how to numerically impose an incoming wave on the boundary situated inside the duct. This “matching plane” is the principal source of sound for the problem considered. It must therefore be accurate, and also allow scattered waves to exit the computational domain. The latter come from the reflections at the inlet mouth of the different acoustic modes, occurring because of the impedance mismatch between the inside of the duct and the free-field domain. This is more important close to cut-off conditions [99]. The modes can be obtained by a modal decomposition technique, such as that developed by Ovenden and Rienstra [100]. If the modes considered are not strongly cut-on, artificial reflections can occur if the incoming waves are simply imposed on the boundary, through a Riemann problem [37] or simply by imposing the values directly on the surface [9].

An alternative approach is to apply an appropriate radiation boundary condition to the outgoing waves only: by subtracting from the main unknowns vector $\boldsymbol{Q'}$ the desired incoming solution $\boldsymbol{Q'_{in}}$, the desired treatment is then applied to $\boldsymbol{Q'_{out}} = \boldsymbol{Q'} - \boldsymbol{Q'_{in}}$, as in Ref. [95]. Dong [101] proved that, in a perfectly thin cylindrical duct of finite length, aligned with the x axis, carrying a simple flow of Mach number M, the condition:

$$\left[\frac{\partial}{\partial t} + (M-1)\frac{\partial}{\partial x}\right]\boldsymbol{Q'_{out}} = 0 \tag{2.17}$$

allows incoming modes to enter and reflected modes to exit. It is accurate to the order of the square of the cut-off ratio. It has been used for example by Li *et al.* [96] with good results. Other researchers use a 1-D formulation of the asymptotic boundary conditions, on the matching surface, which is very close to Eq. (2.17) [102].

Zhang [52] studied different methods to be used in this fashion for the generation of modes in an annular duct for the downstream radiation of internal tone noise. Amongst these was an implicit formulation, which introduces a progressive damping, whilst generating the correct acoustic input $\boldsymbol{Q'_{in}}$. For each time step, the solution vector $\boldsymbol{Q'}$ is damped, at the end of the time integration process, to obtain the final vector $\boldsymbol{Q'_e}$ through the following formulation:

$$\boldsymbol{Q'_e} = \boldsymbol{Q'} - \sigma(\boldsymbol{Q'} - \boldsymbol{Q'_{in}}) \tag{2.18}$$

The absorbtion coefficient σ is given by

$$\sigma = \sigma_m \left(\frac{|x - L|}{L} \right)^{\beta} \tag{2.19}$$

where σ_m is the amplitude of the dissipation, L the length of the absorbtion zone and β a power coefficient. It compares favorably to several other absorbing boundary conditions, including PML and implicit formulations, generating very little spurious reflections over a large variety of wave angles [52]. It has already been pointed out that the PML formulation, applied inside a duct will lead to instability in the presence of mean flow, unless group velocities are carefully adjusted [92, 93].

A fully accurate, non-reflecting boundary condition for acoustics in bounded flows is still an open topic of research, and partial solutions often involve a complex analysis of all in- and out-going modes, with non-local treatments in space or time [103, 104], which will lead be computationally expensive.

Chapter 3

Three-dimensional wall treatment for noise propagation

Free-field sound propagation has been described in Chapter 2 but the accurate representation of wall boundaries is more delicate, and represents a major topic of research in CAA. The use of high-order discretisation schemes introduces many difficulties, mainly because they are very sensitive to the properties of the discretisation grid used, particularly compared to overly diffusive low-order methods. In this chapter, popular practices are reviewed, focusing on structured immersed boundary techniques, which allow the use of a uniform Cartesian grid. One of the main contribution of this research work is described: a novel algorithm to systematically treat immersed wall boundaries in 3D, specifically designed for acoustic problems.

3.1 Literature survey

3.1.1 Wall boundary condition and finite difference

Tam and Dong [105] described a well-posed way of enforcing the inviscid wall boundary condition: a row of virtual pressure values (called *ghost values*) is added just behind the wall, as shown in Fig. 3.1. They are only included in the stencils used to compute pressure derivatives, and their value is determined so as to enforce the condition of zero normal velocity on the wall surface, through the momentum equations. As described in Section 2.2.1 on page 47, shifted stencils are used near the wall.

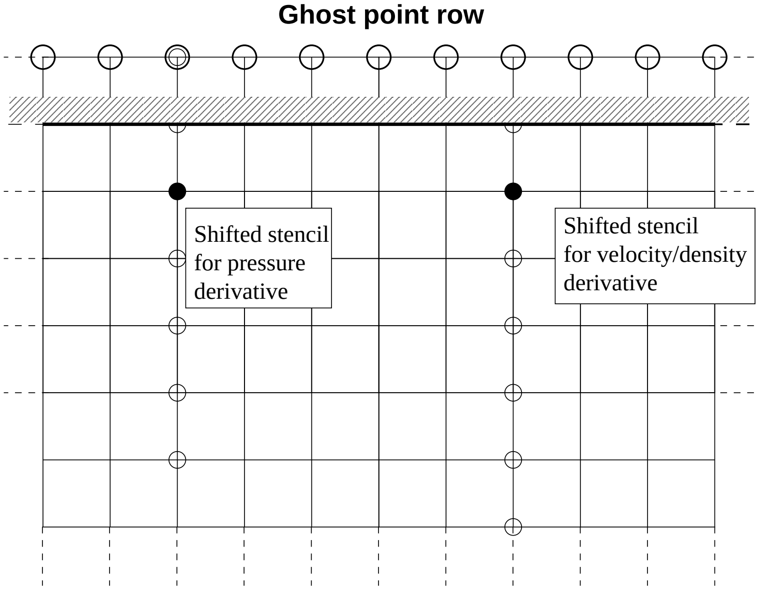

Figure 3.1: Finite difference stencils next to a straight wall.

In practice, the wall geometry does not coincide with grid lines, and finding efficient ways to accommodate this is currently a major topic of research in CAA. Using a staircase boundary [59, 81] is an easily implementable, but only zero-order accurate approximation [106]. In simple cases, cylindrical [9, 46] or spherical [71] coordinates systems can be used, although they can be highly skewed in the azimuthal direction, and introduce a singularity in the equations, creating instability problems [9].

A popular way to ensure that grid lines are orthogonal to the surface is to use a structured body-fitted grid. However, the generation of good quality grids is often complex and expensive, in some cases taking more time than solving the flow equations. It is a process that is hard to automate. Even the generation of unstructured grids can be very complex in 3D if high-order elements are sought [107]. If several different complex configurations need to be assessed in a product design phase, the time spent generating a grid becomes a problem; this is even more acute when automated optimisation searches are performed [102].

Standard grid-generation algorithms introduce excessive clustering near singular points when dealing with complex curved geometries (see Refs. [9] and [29]). Özyörük [9, 35] uses conformal grids, which are of a very good quality, but a large part of his work in Ref. [9] deals with the analytic generation of the grid in a specific case, so this is not a very flexible technique. This has led to the investigation of overset multiple grid ("chimera") techniques: connecting several simple grids together, each one adapted to the wall geometry or to free-field propagation [45, 108, 109]. This technique is well-suited to viscous problems, where the flow and noise of the boundary layer are important, as the strong gradients require more grid clustering next to the wall. But the interface between the different grids is delicate to handle, and losses can occur.

The particular sensitivity of high-order schemes to grid properties, compared to the generally more dissipative low-order schemes, is an important problem [46, 110–112]. Excessively deformed grids and sudden transitions can lead to crippling instability, if smoothness constraints are not respected. Additionally, noise propagation is intrinsically isotropic [2]. Traditionally generated grids have some preferred directions, which are often close to those of a convective flow, but this is not suitable to the nature of the sound waves. Artificial refraction and scattering will be introduced: non-physical clustering and warp can be present, even far from the walls. This is exacerbated by the increased sensitivity of high-order schemes, and contributes to the inaccurate evaluation of the wavenumber. These concerns have led some researchers to perform a complex optimisation of the scheme for optimum wavenumber accuracy on the specific deformed grid used [110].

In summary, the meshing techniques developed for traditional CFD, already quite challenging for complex 3D geometries, should be used with caution in the context of CAA, where more sensitive schemes are used and the waves propagate isotropically. In the current research, a structured approach is taken, which allows the use of the simple regular grids described in the following section.

3.1.2 Immersed boundary methods

The alternative to body-fitted grids or multi-domain implementations is to retain a regular, orthogonal grid and to implement the boundary condition at the intersections between the grid and the surface. The boundary is said to be *immersed* inside the grid system. There has been recent interest in this type of method, for example in the field of biological fluid mechanics. This was driven by the need to handle complex and even moving geometries, like blood vessels, without the need for a lengthy meshing procedure [113].

Various methods can be regrouped under the "immersed boundary" label: they use a reconstruction of the solution at the boundary of the solid surface, overlayed on a fixed regular grid. Virtual "ghost" points, situated close to the solid surface, exert a force determined to induce the desired boundary condition [106, 113–116]. "Cut-cell" methods are similar, but typically used with finite volume discretisations. They take into account the way the surface intersects the Cartesian cells to form smaller, irregular ones. This necessitates merging those smaller cells with the main ones, to avoid the small time steps associated with the former [117, 118].

These schemes were not designed to solve CAA problems, and use low-order spatial discretisations, with almost invariably the equivalent of a simple linear interpolation to estimate the values on the boundary from those in the surrounding fluid. For example, Fadlun *et al.* [106] use a linear interpolation between the desired boundary velocity and the surrounding known quantities. The resulting solution is correct because the global second-order accuracy is preserved, as is the case for many Cartesian boundary treatments [119]. Tran and Udaykumar [114] describe an immersed boundary method associated with a high-order ENO scheme. They use low-order extrapolation along the normal direction to determine the values of the ghost points. The order of the scheme is reduced locally by the boundary treatment, but a high order scheme is retained in most of the domain, so they claim an overall good accuracy should be maintained.

Lombard and Piraux [120] briefly review the *immersed interface* methods which are used to model acoustic behaviour in inhomogeneous media, and present a method designed specifically to deal with the discontinuities involved with inhomogeneous, solid/fluid interfaces. A Cartesian grid is used throughout and a polynomial reconstruction is made near the surface, to obtain a stable and overall second-order accurate solution.

3.1.3 Cartesian-grid preserving method for aeroacoustics

For the treatment of acoustic propagation problems, the relevant consideration is the spatial resolution needed to accurately represent the wavenumber of the acoustic signals [30]. It is important to retain a high-order accuracy to maintain small levels of dissipation and dispersion errors, and perform more efficiently than low-order schemes. With this in mind, Kurbatskii [121] designed an immersed boundary method for aeroacoustics that preserves the Cartesian grid in the whole domain. The method uses a description of how the surface intersects with the grid lines. A systematic algorithm determines on which segment of the boundary to implement the boundary condition, using an exhaustive classification of the different geometrical situations around the ghost points [2]. The result, in a typical situation, is represented in Fig. 3.2.

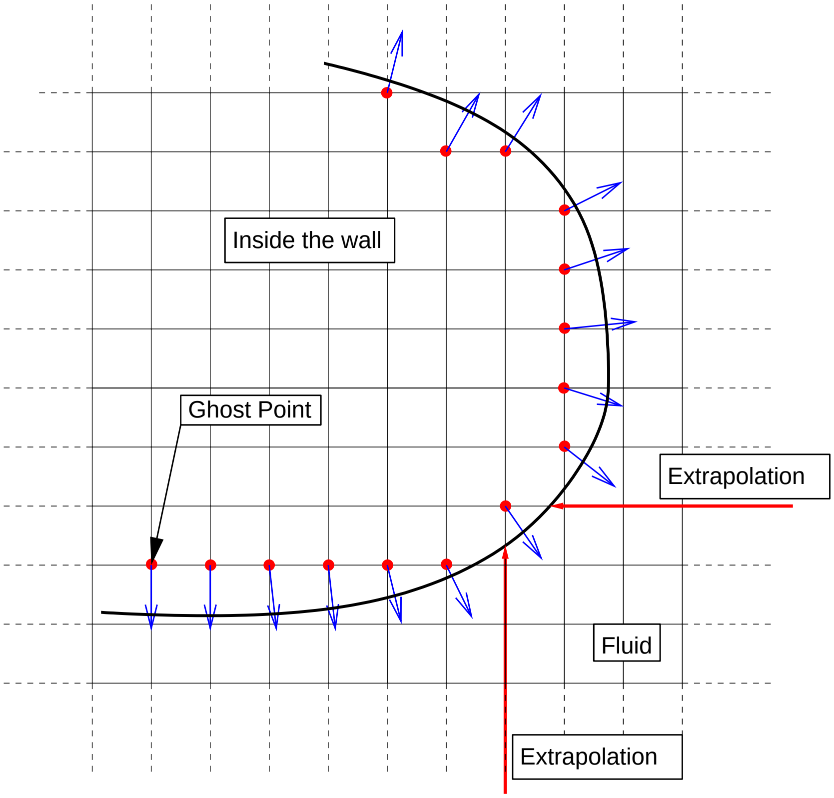

Figure 3.2: Ghost points and the corresponding normal vectors behind a smooth, slightly curved wall. The extrapolation procedure is schematised in bold.

Pressure gradient values are extrapolated, from inside the fluid, to the enforcement point on the surface to determine ghost values of pressure. Tam and Kurbatskii [84] found that it is necessary to use an optimised high-order extrapolation scheme, to obtain good accuracy for the desired wavenumber range, and to suppress the instability caused by spurious short wavelengths. This wavenumber-optimised approach performs better than a traditional B-Spline method [109].

3.2 3D algorithm for CAA

Modelling 3D walls is a challenge but it is important because few real intake or bypass ducts are axisymmetric, for aerodynamic or acoustic design reasons, and it was pointed out in Section 1.1.2 that many noise generation and propagation mechanisms are three-dimensional, so an axisymmetric analysis can be insufficient. Additionally, the explicit finite difference method then has a distinct advantage over implicit schemes for which the computational effort increases dramatically when going from 2D to 3D.

A 3D cut-cell method was developed by Yang *et al.* [117], but it approximates the discretised surface with quadrilaterals to obtain an estimate of the normals and the volume fraction of solid/liquid in each cut cell, which might be too inaccurate. Casalino [78] has taken a 3D immersed boundary approach, but in conjunction with the GFD method. Complex, moving 3D boundaries can be represented by a level set method, together with an immersed boundary approach, although obtaining the level set representation can be complex [79]. The method of Fadlun *et al.* [106] is also 3D, but like most of schemes of this type found in the literature, uses a low-order local reconstruction of the solution near the wall.

Because of the demands of acoustic problems, a higher order of accuracy would be needed, so in this section an algorithm for 3D wall geometries is presented, developed for CAA as part of the present research.

3.2.1 Description of the 3D immersed boundary algorithm

The method developed in this work is based on an extension of Kurbatskii's 2D method described above, involving some additional challenges because of the complexity of 3D geometries, and some different algorithmic and computational issues. The main difficulty is that performing a 3D analysis means a much larger number of situations need to be assessed and classified compared to 2D geometries. But obtaining a systematic and efficient method is worth the effort in design and programming.

The intersection of the wall surface with the regular Cartesian grid-lines, along the x, y and z axes, and the nature of each grid point (in or out of the wall), are supposed to be known. In all the cases studied in this work, this is straightforward because a mathematical description of the surface is known. Such a description is used in parametric optimisation of a surface's shape [102]. However, in many practical engineering applications, the surface of an object is discretised by a Computer Assisted Design (*CAD*) program as an unstructured collection of triangles. From this, the desired description can be extracted using techniques inspired by research in computer graphics, such as those given by Aftosmis *et al.* [122] or Yang *et al.* [117].

First, some assumptions will be made: the curvature *radii* of the surface(s) are assumed to be large relative to the grid spacing; the surface is also assumed to be smooth and regular. This is justified not only by the nature of the geometries to be modelled, engine inlets, but also because in scattering problems, details of the surface have little impact if their characteristic length is much smaller than the wavelength considered: they are in effect not "seen" by the waves. And here, only wavelengths of more than 7 grid-lengths are considered. This is different from the general 2D method of Ref. [120] which requires a smooth surface for the reconstruction scheme. The surfaces can be convex or concave, connected or not.

Overall, the method requires the solution of a matrix equation, obtained in a pre-processing phase, to implement the slip boundary condition. The latter is enforced, for each ghost point, on a neighbouring surface element. The method also allows the use of parallel machines to speed up the computation, as the computation of the ghost values, made before the residuals are computed (and which could also be parallelised), would not interfere.

Choosing a normal direction

Ghost points are *exterior* grid-points (in the wall) which are immediately surrounded by one or more fluid points. For each of these points, the associated ghost value of pressure is determined by applying the inviscid wall boundary condition on an enforcement point E situated on the discretised surface. A correct normal direction, along which it is situated, must be chosen in each case. A discretisation of the normals is made: there are several facets surrounding each ghost point, but only one direction must be chosen, as representative of the local nature of the surface as possible, as illustrated in Fig. 3.2. The approach used in 2D by Kurbatskii, summarised in Fig. 3.3, picks a normal according to the local situation: a systematic algorithmic can be implemented, replacing the meshing process [2].

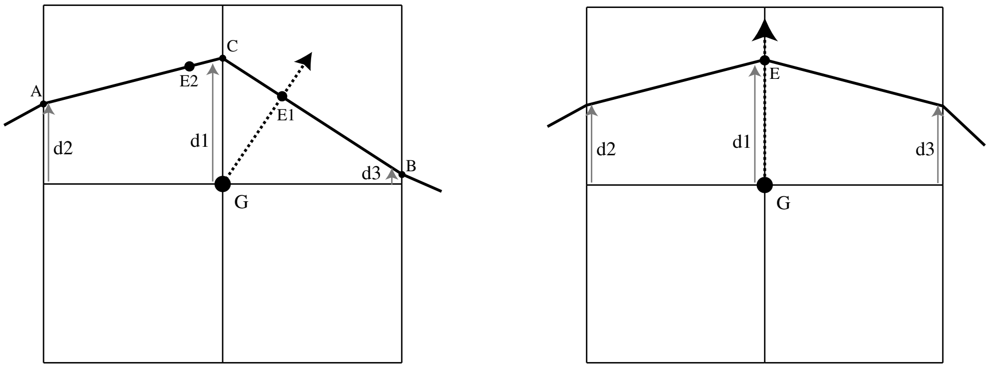

(a) Convex situation.

(b) Symmetric situation.

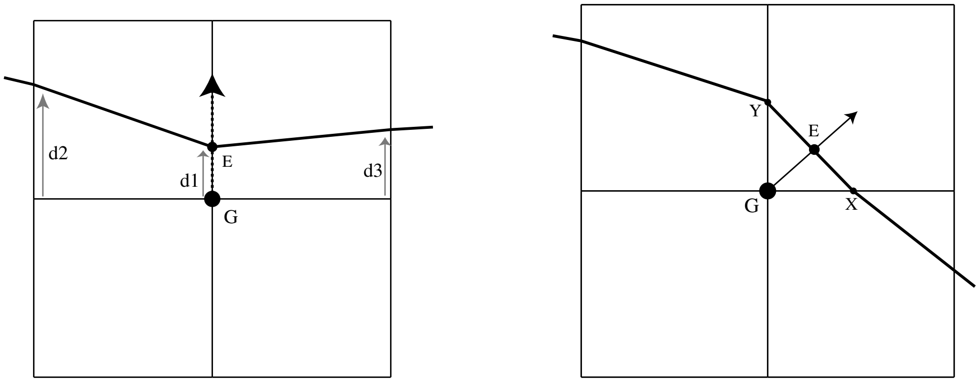

(c) Concave situation.

(d) Double intersection case.

Figure 3.3: Typical situations in the 2D algorithm of Ref. [2].

Overall, when there is a locally convex situation, such as in Fig. 3.3(a), the boundary condition is enforced on the segment or vector with the shortest distance to the ghost point ($\overrightarrow{CB}$ in this example). If the surface is symmetric (Fig. 3.3(b)), or locally convex (Fig. 3.3(c)), then the normal direction will coincide with one of the axes. This cannot be the case if there are two intersections on both axes: Fig. 3.3(d).

Situations similar to those of Figs. 3.3(a)–3.3(c) arise often, and for the these cases, the vector on which the enforcement point E is obtained by projection can be determined by comparing the intersections coordinates d1, d2 and d3 (*cf.* Fig. 3.3(a)), according to the following rule:

- E=orthogonal projection of G on $\overrightarrow{CA}$
  IF $d_2 \neq 0$ AND $d_2 < d_1$ AND ($d_2 < d_3$ OR d_3=0)
- E=orthogonal projection of G on $\overrightarrow{CB}$
  IF $d_3 \neq 0$ AND $d_3 < d_1$ AND ($d_3 < d_2$ OR d_2=0)
- E=C in all other cases

$d2$ or $d3$ being set to zero if there are no intersections. For the situations similar to Fig. 3.3(d), the projection is simply made on the vector $\overrightarrow{XY}$.

There are other cases in the method of Ref. [2] where sharp corners and highly curved surfaces are present, and are modelled using multiple ghost points with several normal directions. But this will not be considered in the current 3D method because of the assumptions made in the previous section.

In the 3D extension described therein, a similar approach will be taken. Each ghost point is surrounded by eight 3D cells, and the wall surface intersects each of them in several points, which are rarely co-planar. The discretised surface can be considered as an assembly of triangles, connecting the intersection points three by three.

According to the situation around the ghost-point considered, there are three different possibilities. The boundary condition will be either enforced on a triangular facet, on a segment, or on a point: see Fig. 3.4. These configurations, and the reason why they are used, are similar to the 2D situations of Fig. 3.3. In the general case (Fig. 3.4(a)), the projection will be made on a triangular facet defined by 2 vectors $\vec{a} = \overrightarrow{OA}$ and $\vec{b} = \overrightarrow{OB}$, as described in Fig. 3.4(b). The relevant triangle is the one closest to G. The enforcement point E is the projection of the ghost point G on the facet, and this defines the normal direction. In the case of Fig. 3.4(c), one of the vectors ($\vec{a}$ or $\vec{b}$) is null, and the triangle reduces to a line. In the last case (Fig. 3.4(d)), both vectors are null and the triangle is reduced to the single point O, the normal direction coinciding with a coordinate axis.

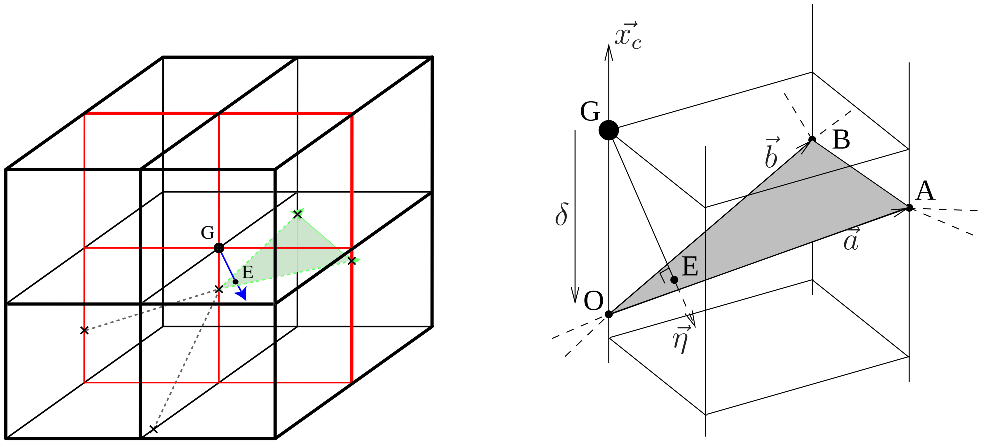

(a) Enforcement on a triangular facet. (b) Parameters in the general case.

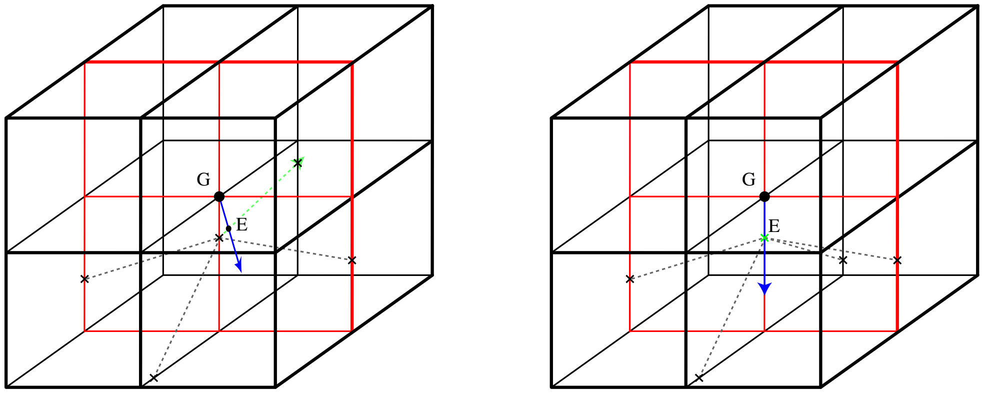

(c) Enforcement on a segment. (d) Enforcement on a point.

Figure 3.4: Typical situations in the 2D algorithm of Ref. [2] and corresponding normal.

The subsequent interpolation and extrapolations used to obtain the pressure gradient at point E will be described below, but first, the systematic algorithm which determines vectors $\vec{a}$ and $\vec{b}$ (or their absence) will be outlined in the following section. Generally, when the facet geometry is convex, the closest triangle facet is chosen, but in concave or symmetric cases, the choice is more complex.

Determining the local surface geometry type

First, an analysis is done in the (G,$\vec{x}$,$\vec{y}$) plane (in blue in Figs. 3.6–3.8): G is classified according to the nature of the immediately surrounding points. This particular plane was chosen arbitrarily, but it will be observed later that this does not introduce anisotropy in the normal directions. This initial analysis limits the number of subsequent possibilities, particularly given the low curvature hypothesis made above. A base point O is also determined: this fixes the origin of the $\vec{a}$ and $\vec{b}$ vectors, and the $\vec{x_c}$ axis on which it is situated.

Depending on these results, $\vec{a}$ and $\vec{b}$ (or their absence) are then chosen using the procedure described below. The presence of $\vec{a}$ or $\vec{b}$ determines points A or B, used for extrapolation. If absent, the triangle reduces to a line or a point as explained above.

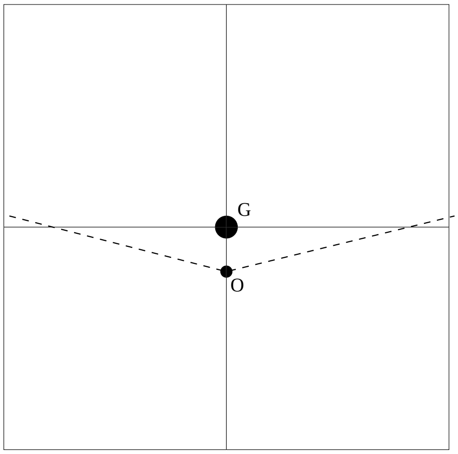

Figure 3.5: Examples of double intersection situation.

The 2D analysis rule of page 69 (illustrated in Figs. 3.3(a)–3.3(c)) will be used several times to choose a vector according to the intersection coordinates on neighbouring axes: a vector ($\vec{a}$ or $\vec{b}$) or a point (null vector) is chosen. In cases where there are double intersections on the same axis, as in Fig. 3.5, a symmetric configuration will be chosen (null vector), since sharp points are not modelled.

Each point G (coordinates (l, m, n)) is first classified according to the number N_e of exterior points immediately surrounding it on the x and y axes (coordinates $(l \pm 1, m \pm 1, n)$). This is related to the number of surface/grid lines intersections immediately surrounding G. In Fig. 3.6–Fig. 3.8, these exterior points are represented by squares, and intersection points by crosses. Four types of situations are found:

Type 1: $N_e = 3$
There is only one intersection next to G, which immediately determines the point O and the $\vec{x_c}$ axis (either $\vec{x}$ or $\vec{y}$). Then, a 2D analysis is made in the (G,$\vec{x}$,$\vec{y}$) plane to choose $\vec{a}$, comparing the intersection deltas along the $\vec{x_c}$ axis, for both neighbouring ghost points situated on the other axis (*i.e.* $\vec{x}$ if $\vec{x_c}$=$\vec{y}$). After this:

- If there is an intersection on the $\vec{z}$ axis, it is used as point B and $\vec{b} = \overrightarrow{OB}$. For example see Fig. 3.6(a).
- If not, a 2D analysis is done in the (G,$\vec{x_c}$,$\vec{z}$) plane to determine $\vec{b}$, using the two neighbouring ghost point along $\vec{z}$. For example see Fig. 3.6(b).

Type 2: $N_e = 2$
Here, there are two intersections, on the axes neighbouring G. A choice of the point O must be made, between O_x ($\vec{x_c} = \vec{x}$) and O_y ($\vec{x_c} = \vec{y}$). The following method is used:

- If there is an intersection on the $\vec{z}$ axis, it is used as point B, and O=O_x is arbitrarily chosen , and then $\vec{b} = \overrightarrow{OB}$, and $\vec{a} = \overrightarrow{O_xO_y}$. For example, see Fig. 3.7(a).
- If not, a 2D analysis is made in *both* the (G,$\vec{x}$,$\vec{z}$) and (G,$\vec{y}$,$\vec{z}$) planes. If two potential $\vec{b}$ vectors are found, the triangle with the shortest distance to G must be chosen: the one with the highest difference $|d_1 - d_{2/3}|$. If the chosen point B is in plane (G,$\vec{y}$,$\vec{z}$) then O=O_y, and *vice-versa*. For example, see Fig. 3.7(b), where O=O_y.

Type 3: $N_e = 4$
There is no intersection in the (G,$\vec{x}$,$\vec{y}$) plane. For example, see Fig. 3.8. There is

(at most)one intersection on the $\vec{z}$ axis: this determines the point O. Then, two 2D analysis are made:

- one in the (G,$\vec{x}$,$\vec{z}$) plane to determine $\vec{a}$
- one in the (G,$\vec{y}$,$\vec{z}$) plane to determine $\vec{b}$

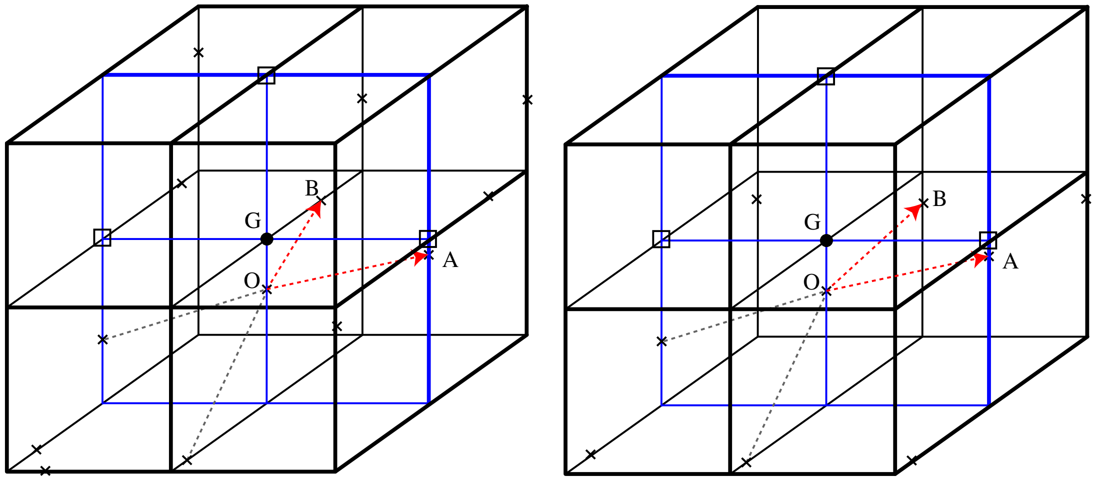

(a) Type 1a (b) Type 1b

Figure 3.6: Examples of 3D type 1 situation around a ghost point G (general case of a triangular facet).

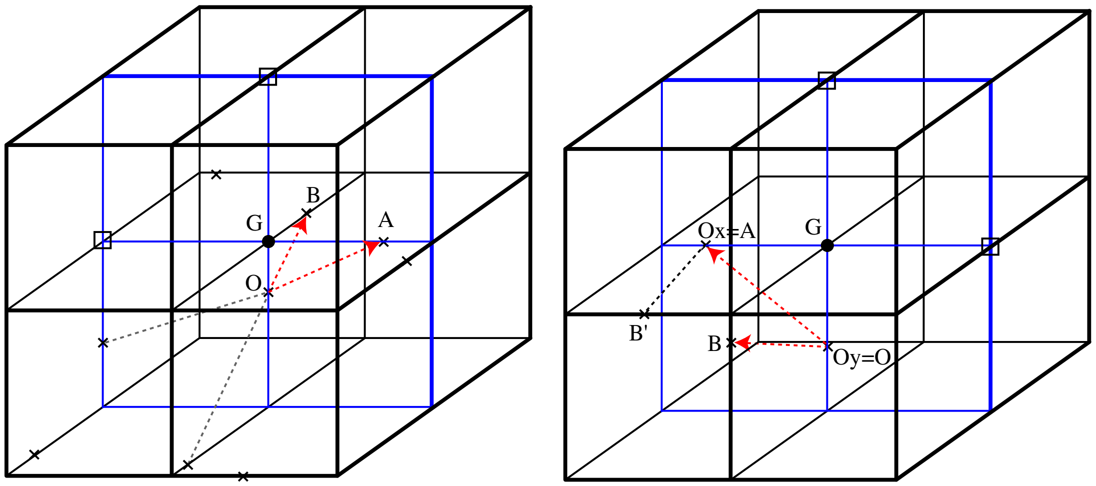

(a) Type 2a (b) Type 2b

Figure 3.7: Examples of 3D type 2 situation around a ghost point G (general case of a triangular facet).

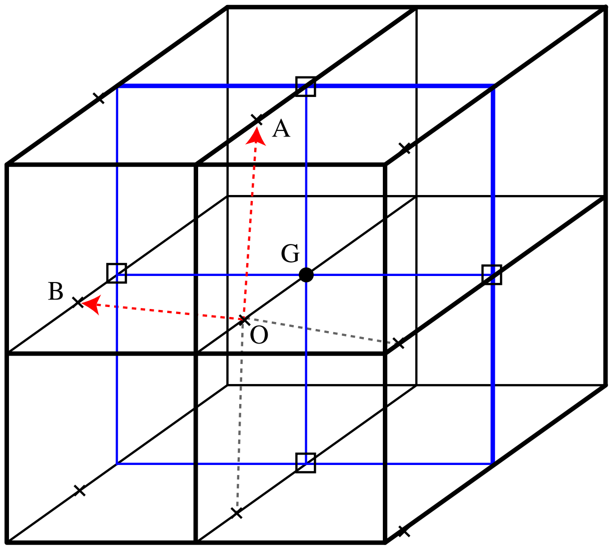

Figure 3.8: Examples of 3D type 3 situation around a ghost point G (general case of a triangular facet).

Interpolation and Extrapolation

In the general case, $\vec{a}$ and $\vec{b}$ have been determined; the normal vector $\vec{\eta}$ is then obtained by the normalized vector-product:

$$\vec{\eta} = \frac{\vec{a} \times \vec{b}}{\| \vec{a} \times \vec{b} \|} \tag{3.1}$$

The orientation of $\vec{\eta}$ is not important here, since only an orthogonality condition is needed. The vector $\vec{\eta}$ intersects the OAB triangle at point E, where the boundary condition (Eq. (2.16)) is expressed.

The following method was inspired by ray-tracing algorithms in the field of computer graphics [123]. The enforcement point E, orthogonal projection of the ghost point G on the OAB triangle, is described by Λ_a and Λ_b parameters, the natural coordinates of E in the triangle:

$$\overrightarrow{OE} = \Lambda_a \vec{a} + \Lambda_b \vec{b} \tag{3.2}$$

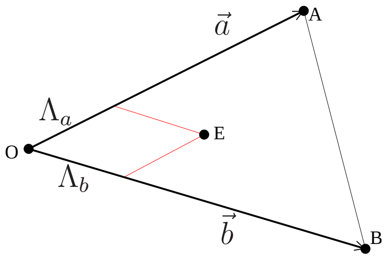

Figure 3.9: The OAB triangle with interpolation parameters.

Those parameters, as represented in Fig. 3.9, represent the interpolation quantities needed to obtain the pressure derivative, and thus the velocity, at point E, from values inside the fluid. Indeed, any function f, defined on the triangle, can be approximated as:

$$f(E) \simeq \Lambda_a f(A) + \Lambda_b f(B) + (1 - \Lambda_a - \Lambda_b) f(O) \tag{3.3}$$

The values of these parameters are obtained by expressing the orthogonality condition with the unit normal vector $\vec{\eta}$ (Eq. (3.1)) as:

$$(GE) \perp OAB \quad \Leftrightarrow \quad \overrightarrow{GE} \times \vec{\eta} = (\overrightarrow{GO} + \overrightarrow{OE}) \times \vec{\eta} = \vec{0} \tag{3.4}$$

Defining $a_c = \vec{a}.\vec{x_c}$ and $b_c = \vec{b}.\vec{x_c}$, and using Eq. (3.2) leads, after solving a simple linear system, to:

$$\Lambda_a = \frac{\delta(b_c(\vec{a}.\vec{b}) - a_c|\vec{b}|^2)}{|\vec{a}|^2|\vec{b}|^2 - (\vec{a}.\vec{b})^2} \tag{3.5}$$

$$\Lambda_b = \frac{\delta(a_c(\vec{a}.\vec{b}) - b_c|\vec{a}|^2)}{|\vec{a}|^2|\vec{b}|^2 - (\vec{a}.\vec{b})^2} \tag{3.6}$$

When the triangle reduces to a single segment, point E then becomes the orthogonal projection of the ghost point G on either $\vec{a}$ or $\vec{b}$ (and Eq. (3.6) remains valid). In other cases, the enforcement point is simply coincident with O, on the $\vec{x_c}$ axis (and $\vec{\eta} = \vec{x_c}$).

The values of the pressure derivatives at points A, B and O are then needed; they are estimated from values inside the fluid with the same carefully designed extrapolation used in the 2D method. It uses the values at 7 points along the appropriate coordinate axis, and is optimised for maximum accuracy in the range of wavelength of interest ($\lambda \geq 7$). An extrapolation based on high-order Lagrange polynomial is unsuitable as it leads to instability, because of numerical errors in the high wavenumber range [84].

When the slip boundary condition of Eq. (2.16) is fully developed, using Eq. (3.3) and the appropriate extrapolations, the following equation is obtained:

$$\begin{aligned}
\frac{\partial p}{\partial n}(E) &= \frac{\partial p}{\partial x}(E)\eta_x + \frac{\partial p}{\partial y}(E)\eta_y + \frac{\partial p}{\partial z}(E)\eta_z = 0 \\
&= \left(\Lambda_a \frac{\partial p}{\partial x}(A) + \Lambda_b \frac{\partial p}{\partial x}(B) + (1 - \Lambda_a - \Lambda_b)\frac{\partial p}{\partial x}(O)\right)\eta_x + \dots \\
&= \left(\Lambda_a \sum_{1}^{7} \kappa_i(A) \frac{\partial p}{\partial x}(P_i^A) + \dots \quad \textit{etc.} \qquad\qquad\qquad \right)\eta_x + \dots
\end{aligned}$$

where $\{P_i^A\}_{i=1\to 7}$ are the extrapolation points related to point A, with the corresponding optimised extrapolation weights κ_i [84]. For each of these, the derivative $\frac{\partial p}{\partial x_j}(P_i)$ is expressed with the adequate DRP discretisation stencil, according to their proximity to the boundaries. These stencils mostly include points in the fluid, but also sometimes ghost points. Therefore the different ghost values are interdependent, and this will lead to a linear system that should be expressed in matrix form. By putting all the terms involving ghost values on the Left-Hand Side (*LHS*) of the equation, and all the other terms on the Right-Hand Side (*RHS*), the following is obtained:

$$\tilde{A}\,\tilde{p}_g = \tilde{b} \tag{3.7}$$

The matrix $\tilde{A}$ represents the interdependence of the ghost values of pressure $\tilde{p}_g$. The vector $\tilde{b}$ is related to the pressure values in the fluid surrounding the wall surface through the array $\tilde{C}$ (see Section 3.2.3). $\tilde{A}$ only needs to be inverted once, at the start, and then the vector $\tilde{p}_g = \tilde{A}^{-1}\,\tilde{b}$ is calculated at each time step, giving the values of the pressure at all the ghost points. The implementation of arrays $\tilde{A}$ and $\tilde{C}$ will be described in Section 3.2.3.

3.2.2 Discretisation errors

Before the overall resulting accuracy obtained by the current method is assessed, in the next chapter, through numerical experiments, it is interesting to verify if the surface normal is correctly evaluated by the above algorithm. If the norm $\|\vec{\boldsymbol{V}}\|$ of a vector is defined as $\sqrt{V_x^2 + V_y^2 + V_z^2}$, the maximum error, over all ghost points, on the normal vector $\vec{\boldsymbol{\eta}}$ is computed as:

$$E_\eta = \max(\|\overrightarrow{\eta_{\text{real}}} - \overrightarrow{\eta_{\text{comp.}}}\|) \tag{3.8}$$

For a sphere of radius $a = 20\Delta x$, $E_\eta = 3.2 \times 10^{-2}$ is obtained; this represents (at most) an angle of less than 1° between the true normal direction and the computed one. Furthermore, as can be seen in Fig. 3.10, this error decreases strongly as the sphere radius increases. This shows that the 3D algorithm used to pick the appropriate triangle is effective, and does converge towards a correct estimation of the normal, as a function of the curvature radius. Furthermore, an examination of the errors and the normals, over the whole surface, showed that starting with an analysis in the ($\vec{x}$,$\vec{y}$) plane does not introduce an artificial asymmetry in this computation.

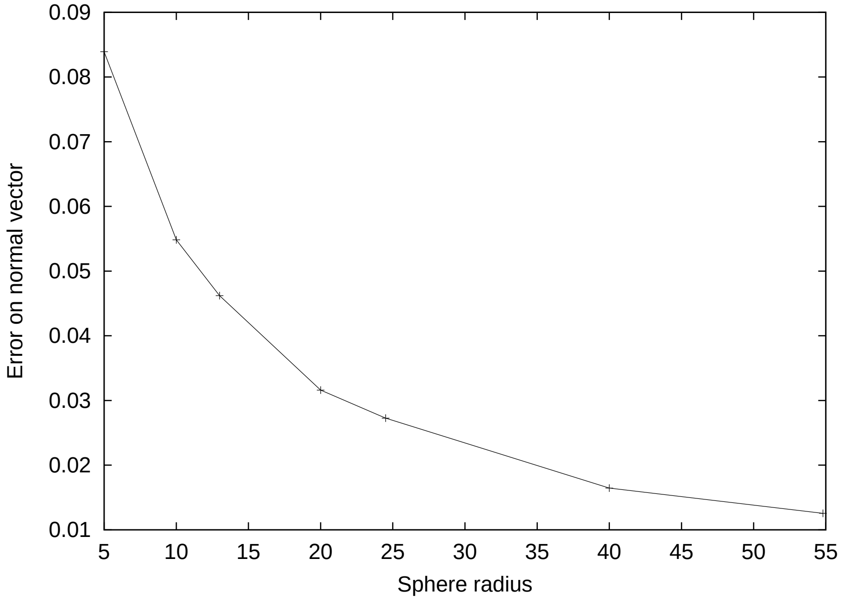

Figure 3.10: Plot of E_η for a sphere as a function of the radius.

It is possible to estimate the error introduced by the triangular discretisation of the real curved surface, in the same fashion as was done by Kurbatskii in 2D [121]. It should be noted that this type of error is common to most numerical discretisation schemes, except for some finite element formulations that take into account the surface's curvature. In a grid cell of dimension Δ, the worst case scenario, shown in Fig. 3.11, is considered. The osculating sphere S, of radius R=CP, the local curvature radius, is tangential to the surface considered at point P. The ratio $\frac{\Delta}{\mathrm{R}}$ has been assumed to be small. So it is possible to obtain an estimation of the distance $\delta = PE$ between the point where the boundary condition should be applied (P) and the point where it actually is (E).

Some simple trigonometry gives:

$$\delta = PE \approx \frac{1}{6}\frac{\Delta^2}{\mathrm{R}} \tag{3.9}$$

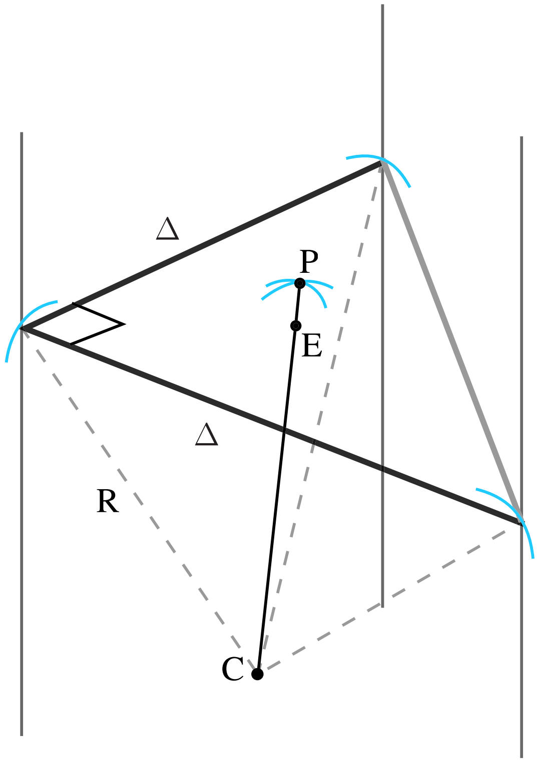

Figure 3.11: Curvature and discretisation (the curvature is exaggerated here).

This is slightly larger than the 2D case, where the ratio was 1/8. For a wave function of wavelength λ, the average error on amplitude over a period [121] is:

$$E_{\text{disc}} = \frac{1}{2}\frac{2\pi}{\lambda}\delta \simeq \frac{\pi}{6}\frac{\Delta}{\lambda}\frac{\Delta}{\mathrm{R}} \tag{3.10}$$

In the case of the maximum resolution of the DRP scheme ($\frac{\Delta}{\lambda} = 1/7$), and a typical curvature of $\frac{\mathrm{R}}{\Delta} = 10$, $E_{\text{disc}} \approx 0.0075$. Therefore intrinsic discretisation errors can be expected to be slightly larger than in the 2D case, where $E_{\text{disc}} \approx 0.0056$ for the same conditions.

Apart from these issues, the main source of error comes from the extrapolation and interpolation schemes. It will be observed in chapters 4 and 5 that, in 3D, the errors become too important. A high-order 7-point extrapolation is used, but for most ghost points, *three* will need to be done, instead of two maximum in 2D, and errors can accumulate. Additionally, a linear interpolation is used within the triangle: *cf.* Eq. (3.3). This can be justified for practical reasons, and by the small (sub-grid) distances involved. A similar approach was successful in the 2D method, but it might contribute to a reduced order of accuracy.

3.2.3 Computational issues

To solve the simple matrix problem of Eq. (3.7) for 2D problems, a standard Gauss-Jordan pivoting algorithm [62] can be used. This cannot be done for large 3D problems, with more than several thousand ghost points, because of escalating memory and computational costs. The specific features of the $\tilde{A}$ matrix can be exploited: it is very sparse because it describes the inter-dependencies between different ghost points that arise when the wall boundary condition is expressed, and only neighbouring ghost points are related. In typical cases, it is less than 1% full. Furthermore, since the indexing of the different ghost points is not directly related to their spatial proximity, the matrix lacks any particular structure. It was therefore chosen to only store in memory the non-zero values of $\tilde{A}$, along with their position, using the special FORTRAN data structure of Fig. 3.12.

As speed was not essential in the pre-processing phase, a simple iterative method was chosen to invert the matrix: the preconditioned bi-conjugate gradient method [62]. This algorithm only requires the result of the multiplication of A (or its transpose) by a vector x, which can easily be done with the data structure chosen, using only the *non-zero* values of $\tilde{A}$. The resulting inverse matrix is also stored in the sparse data structure of Fig. 3.12, after discarding negligible values (less than 10^{-8}). This saves time computing the ghost values $\tilde{p}_g = \tilde{A}^{-1}\,\tilde{b}$.

```
TYPE  sprsa
      INTEGER :: length      % number of elements
      DOUBLE PRECISION, DIMENSION(:) :: val    % value of element
      INTEGER, DIMENSION(:) :: row    % row of element
      INTEGER, DIMENSION(:) :: col    % column of element
END TYPE sprsa
```

Figure 3.12: Fortran data structure for $\tilde{A}$ (and its inverse).

The array $\tilde{C}$ is used to represent the contribution of non-ghost points to the RHS of equation Eq. (3.7). When expressing the boundary condition for the ghost point of index f and value $\tilde{p}_f$, the RHS value $\tilde{b}_f$ is obtained by summing the contribution of every point in the fluid zone, of coordinates (i, j, k), with the weight coefficient $\tilde{C}_{ijkf}$. This is done each time the residuals need to be computed. Formally, this is expressed as:

$$\forall f, \quad \tilde{b}_f = \sum_{i,j,k} \tilde{C}_{ijkf}\, p_{ijk} \tag{3.11}$$

A naive computation of Eq. (3.11) would be very inefficient: in practice, only points in the close neighbourhood of the relevant ghost point have a contribution. Therefore the storage of the values and the summation of Eq. (3.11) should be done only for the non-zero values of $\tilde{C}$. To this end, a new FORTRAN data structure is needed: Fig. 3.13.

```
TYPE sprs
        INTEGER :: length     % number of elements
        REAL, DIMENSION(:,:) :: val    % value of element
        INTEGER, DIMENSION(:,:) :: row % x-coordinate for element
        INTEGER, DIMENSION(:,:) :: col % y-coordinate for element
        INTEGER, DIMENSION(:,:) :: dep % z-coordinate for element
END TYPE sprs
```

Figure 3.13: Fortran data structure for $\tilde{C}$. The additional array column is for the ghost value index, f in Eq. (3.11).

3.2.4 Artificial dissipation

In addition to the shifted stencils next to the boundary (Section 2.2.1), the discontinuity of the sudden fluid-wall transition and the extrapolation procedure represent important sources of instability. Strong artificial selective damping must be introduced to dampen the parasite short waves, as was done on the domain's boundaries. A Gaussian distribution of artificial Reynolds number, of amplitude R^w_Δ and half-width $8\Delta x$, is introduced around all wall surfaces.

It is important to carefully balance the dissipation. If the damping terms are added to the pressure equation, and the ghost values are included in the damping stencils, they could be excessively dissipated [2, 121], which would lead to under-predicted reflected waves. If a strong value of R^w_Δ is used, this might introduce undesirable dispersion and dissipation errors [57]. A good compromise is presented by Kurbatskii [121]: the ghost values are included in the dissipation stencils used for the pressure equation, except in the small, 3-point stencils, closest to the wall. This allows the use of low values of R^w_Δ, typically 0.3–0.4, which leads to more accurate results, as will be seen in the next chapter.

3.3 Locally concave geometry cases

In some cases, encountered in Chapter 5, the surface is sometimes locally concave and the curvature radius becomes relatively small. The extrapolation procedure described above cannot be used because, as represented in Fig. 3.14, the 7-point extrapolation along the axes will exit the fluid domain. It would be preferable to perform an extrapolation along the surface normal, as this direction naturally points away from the concavity of the surface. This would replace the multiple extrapolations along up to three axial directions by a single normal one.

Indeed, several low-order immersed boundary methods take this approach. For example, Tran and Udaykumar [114] determine the ghost point values using 2 points along the direction normal to the surface; as these points are generally not coinciding with grid points, their value is interpolated from the neighbouring points. Gilmanov *et al.* [115] have a similar approach.

This type of technique was investigated in the context of the present study, as described (for a 2D situation) in Fig. 3.15. The gradient at point E is deduced from the values at points A_i. These are obtained from the surrounding grid points by trilinear interpolation [62] if the A_i point inside a normal fluid cell (points A_2–A_4 in Fig. 3.15), or by distance-weighted interpolation [114] if the cell is cut by the solid surface (point A_1). Each pressure derivative is computed with the DRP stencil but, as is made clear in Fig. 3.14, shifted or restricted derivative stencils must sometimes be used. Extensive numerical investigations were made, using a known plane wave solution. The only stable option in this case was to use a

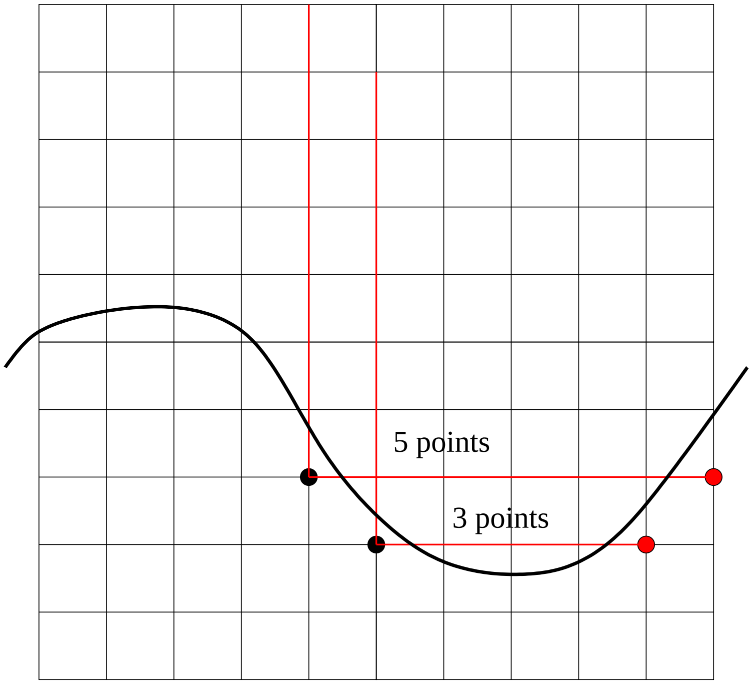

Figure 3.14: Locally concave surface situation.

4-point extrapolation, as shown in Fig. 3.15.

Although the fact that only one extrapolation is performed should lead to better accuracy, this appears to be compensated by the interpolations around the A$_i$ points, which are only low-order and involve a greater number of points. The multidimensional, optimised high-order interpolation of Tam [109] was also used instead of the low-order approach above, but it led to instability, probably because of the high number of points used, which meant that the high-frequency numerical errors would add up. Özyörük [9], in a similar situation, notes that a low-order extrapolation was needed to avoid instability. The method of optimised extrapolation along the Cartesian axes seems quite unique in having been designed for high-order accuracy while remaining stable.

The method of Bin, Cheong and Lee deduces the normal pressure gradient at point E directly, from the pressure *values* of the points A$_i$ and the ghost point, through a Taylor formulation [124]. The pressure values are computed by a high-order accurate, optimised interpolation. It seems promising in the current context, but its results could not be replicated in the present study for lack of time.

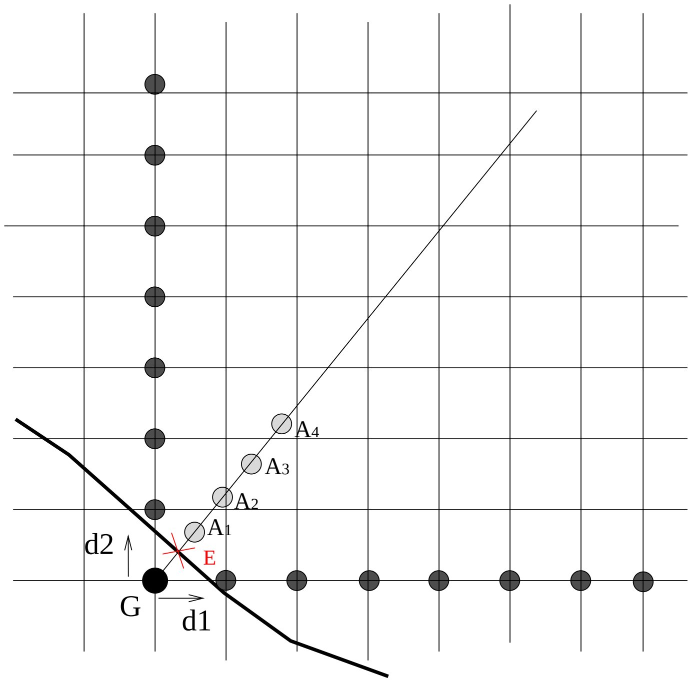

Figure 3.15: Extrapolation along the normal direction (in 2D).

Concluding remarks

A new immersed boundary algorithm was developed to meet the challenge of representing 3D wall boundaries without the need for any meshing techniques, while retaining a large order accuracy throughout most of the domain. This was done by extending an existing 2D method, designing an appropriate systematic algorithm to deal with all possible geometries (with some assumptions on the curvature of the surface). This posed several computational problems which were dealt with. For ghost points in locally concave areas, an alternative, low-order normal extrapolation is used. This method will be validated in chapter 4 on simple benchmark cases, and applied to more complex geometries in Chapter 5.

Chapter 4

Validation cases

In Chapter 2, a high-order CAA numerical scheme was described, and in Chapter 3, the wall boundary was examined in more detail and a new 3D treatment was developed. These methods are now implemented and tested on various benchmark acoustic problems. Such test cases, often with known exact analytical solutions, can be found in references [32, 33, 60, 61, 87]. Some of the methods used here, particularly in 2D, were already thoroughly validated in the literature, therefore it is only their implementation which is tested. Other cases are evaluated qualitatively. Free-field propagation problems are first considered, both in 2D and 3D, including the effects of the underlying mean flow. The optimised Runge-Kutta and Adams-Bashforth time integration methods are directly compared, which has not been done in detail in the CAA literature. The solid wall boundary condition is then implemented, first for simple straight walls, and then with curved immersed boundaries. The new 3D algorithm is assessed on a standard test case before the more complex applications of Chapter 5, and the effects of adding a convective mean flow around these immersed boundary are investigated.

4.1 Free-field Propagation

4.1.1 2D propagation

Acoustic pulse

The propagation of a Gaussian pulse is computed, with the basic 2-D LEE code, by prescribing the initial conditions as:

$$t = 0 : \quad \rho' = p' = 0.01 e^{-\frac{\ln 2}{b^2} r^2} \quad \text{and} \quad u' = v' = 0 \tag{4.1}$$

where r is the radial distance to the domain's center. This allows comparison with the exact solution of Tam and Webb in Ref. [32]. The half-width of the Gaussian pulse is set at $b = 4$. This is first done for zero mean flow ($u_0 = v_0 = 0$, and $\rho_0 = p_0 = 1$).

The computational domain used throughout is a Cartesian, regular, 200 x 200 grid. The computation is first made with the optimised Adams-Bashforth (*OAB*) method, with a small time step ($\Delta t = 0.05$), up to $t = 77$. Excellent agreement is found, as shown in Fig. 4.1. The pulse exits the computational domain with negligible reflection ($< 0.5\%$ of the total amplitude), confirming that the asymptotic radiation boundary conditions are effective.

The LDDRK time-marching schemes can also be used alongside the OAB one. In both cases, the ideal accuracy limits of Table 2.2 on page 54 were tested: $\Delta t = 0.1$ for the OAB, $\Delta t = 0.7$ for the 4-stage LDDRK and $\Delta t = 1.1$ for the 4-stage LDDRK. The LDDRK schemes were, overall, respectively 4 and 6 times faster than the OAB scheme, and they used less memory. As shown in Fig. 4.2, excellent agreement is found, with a slightly worse result for the OAB scheme, probably because the corresponding accuracy constraint is not as stringent as for the LDDRK scheme. Additionally, the theoretical stability limits of Section 2.2.3 were found to be a good indicator for this 2D problem, although for the LDDRK schemes, they were slightly lower in practice: the 4-level scheme becomes unstable from $\Delta t = 1.4$, and the 5-level scheme from $\Delta t = 1.7$. But in all cases, for the frequencies of interest, the accuracy constraint is indeed more stringent.

The same test case is done with a uniformly convective mean flow, along the x direction, as input: $u_0 = M_x = 0.5$ and $v_0 = 0$. The agreement is again excellent,

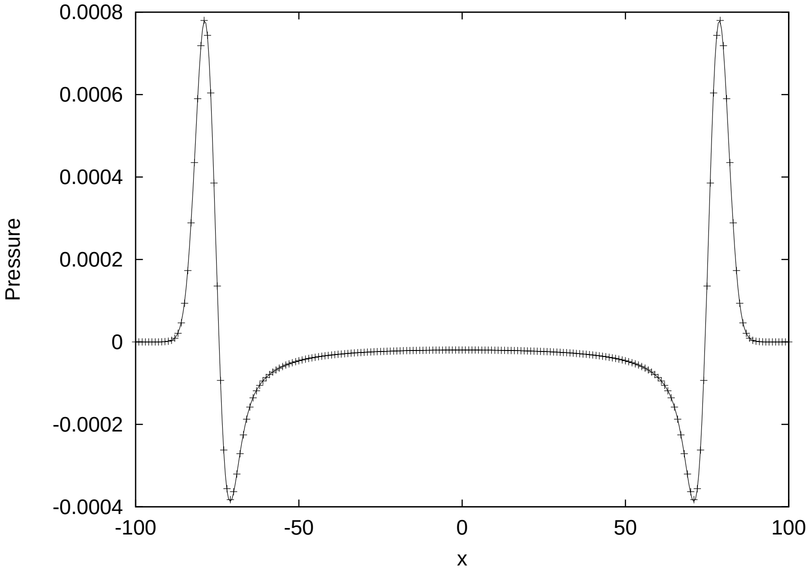

Figure 4.1: Validation of simple linear scheme with a Gaussian pulse. $M = 0$. Cut along y=0. —: exact solution, + +: OAB scheme with $\Delta t = 0.05$.

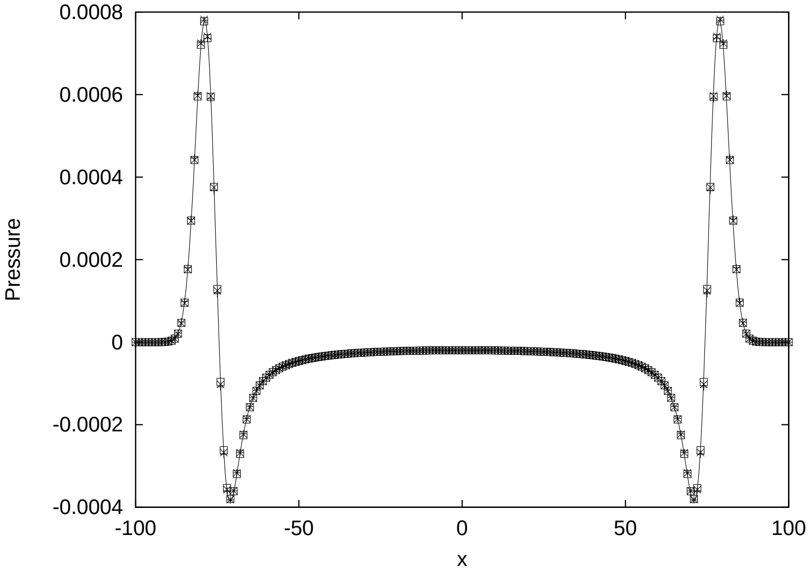

Figure 4.2: Same as Fig. 4.1, with —: exact solution, +: OAB $\Delta t = 0.1$, ×: 4-stage LDDRK $\Delta t = 0.7$, □: 5-stage LDDRK $\Delta t = 1.1$.

as shown in Fig. 4.3. The presence of the flow does reduce the stability and accuracy limits, as predicted in Section 2.2.3.

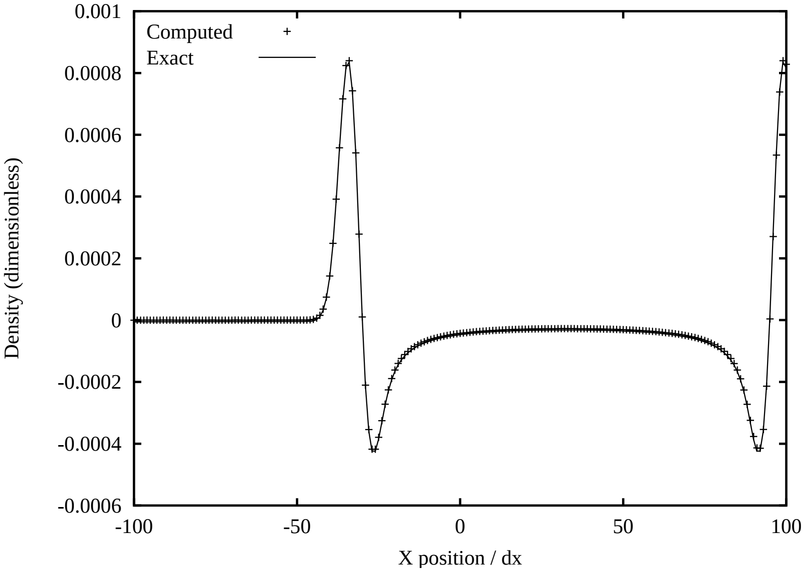

Figure 4.3: Validation of simple linear scheme with a Gaussian pulse. $M_x = +0.5$. Cut along y=0.

Acoustic oscillating source

Fig. 4.4 shows the propagation of a monopole acoustic source: the term of the source vector $\boldsymbol{S}$ (in Eq. (2.2) on page 35) related to the pressure equation is an oscillating term with a smooth Gaussian distribution of amplitude:

$$\boldsymbol{S}_4 = -0.01 e^{-\frac{\ln 2}{8} r_s^2} \cos \omega t \tag{4.2}$$

where r_s is the distance from the center of source which is at the origin of the domain. ω is the circular frequency of the source. The computation is first done with the OAB scheme using $\Delta t = 0.05$, as shown in Fig. 4.4. It is also compared to an analytical solution (Morris [125]), and no significant dispersion or dissipation error can be seen, even for 7 PPW and a propagation over 13 wavelengths.

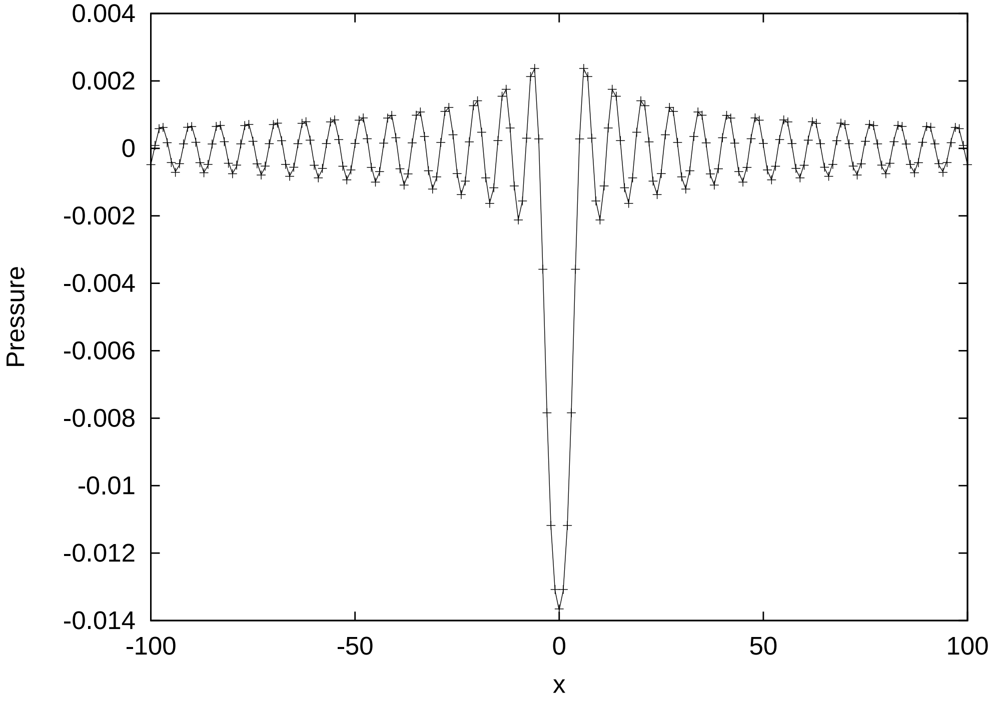

Figure 4.4: Propagation of an acoustic monopole source in 2D ($\lambda = 7$) placed at the domain's center. $+$: OAB scheme with $\Delta t = 0.05$, — : analytical solution. Cut along $y = 0$ line.

The time step is then increased within the theoretical accuracy limits of the different schemes, and the results are shown in Fig. 4.5. Good results are obtained as above, except in the source region for the 5-stage LDDRK because of the large time-steps involved.

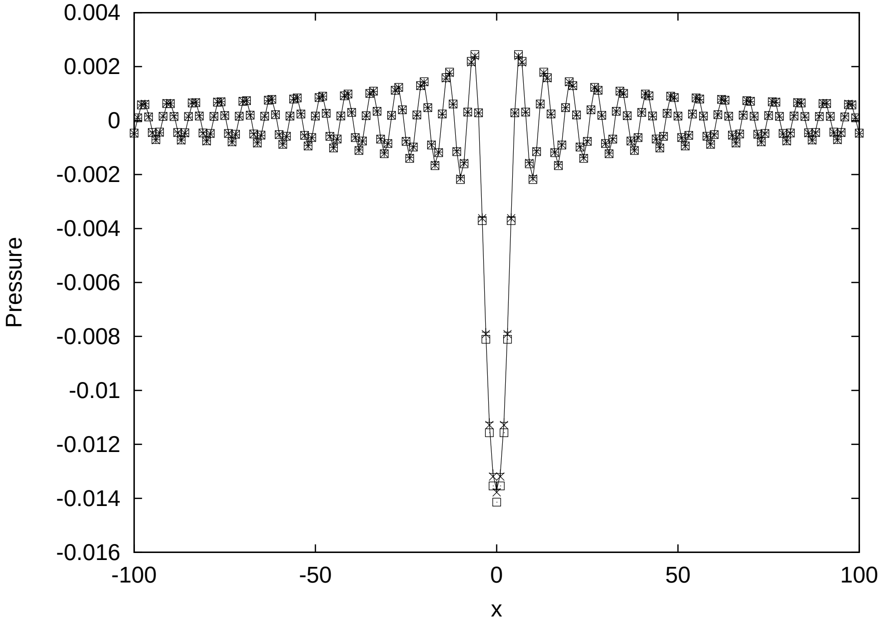

Figure 4.5: Same as Fig. 4.4, with —: exact solution, +: OAB with $\Delta t = 0.1$, ×: 4-stage LDDRK with $\Delta t = 0.5$, □: 5-stage LDDRK with $\Delta t = 1.0$.

A uniform mean flow ($M_x = 0.3$) in the positive x direction is added, and the source is set to oscillate with a period T=15. The acoustic pressure contours are plotted in Fig. 4.6. A pseudo-Doppler effect is apparent: the wavelength is modified by a factor ($1 \pm M$), in this case from 7.5 to 22.5, according to the upstream/dowstream direction of propagation of the waves, as in Refs. [54] and [46].

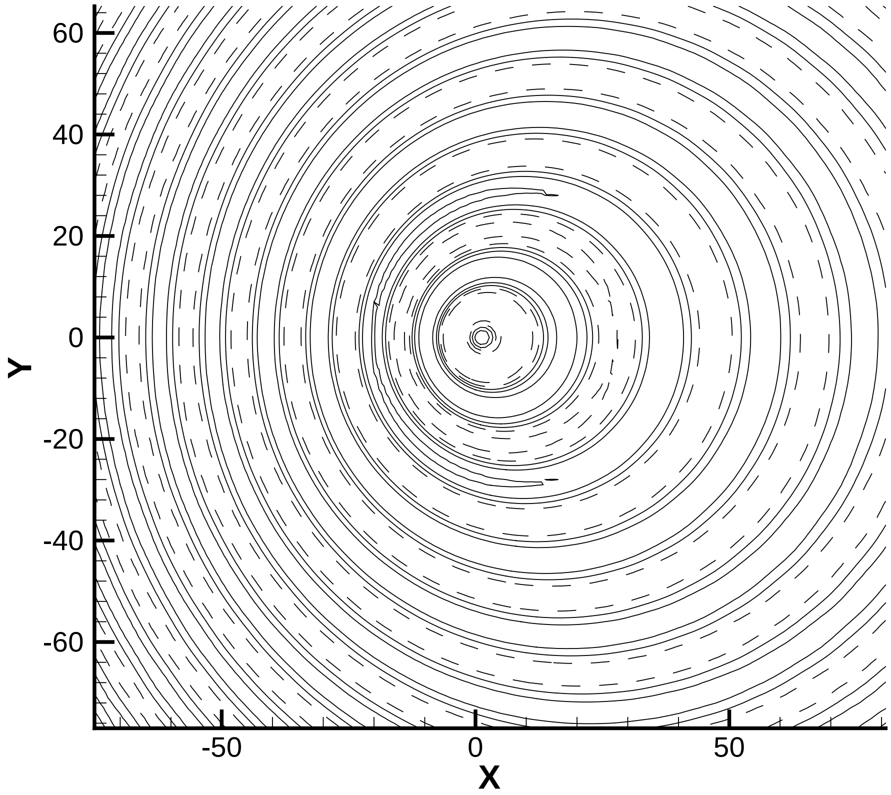

Figure 4.6: Monopole oscillator (T=15) in center of computational domain. $M_x = +0.3$. Pressure contours: 0, $\pm 5\,10^{-3}$, $\pm 2\,10^{-3}$. Negative contours are in dotted lines.

4.1.2 Non-uniform mean flow effects

If the mean flow is not static or uniformly convective, the full LEE need to be used, including the inhomogeneous flow term $\boldsymbol{H}$, from Eq. (2.4). This represents complex refraction effects in the propagation, crucial in fan noise problems, and which are difficult to evaluate other than with computational methods.

To illustrate this effect qualitatively, a symmetric horizontally sheared flow, similar to those used by Bogey *et al.* [7], of maximum Mach number M_s, is given as input (Fig. 4.7):

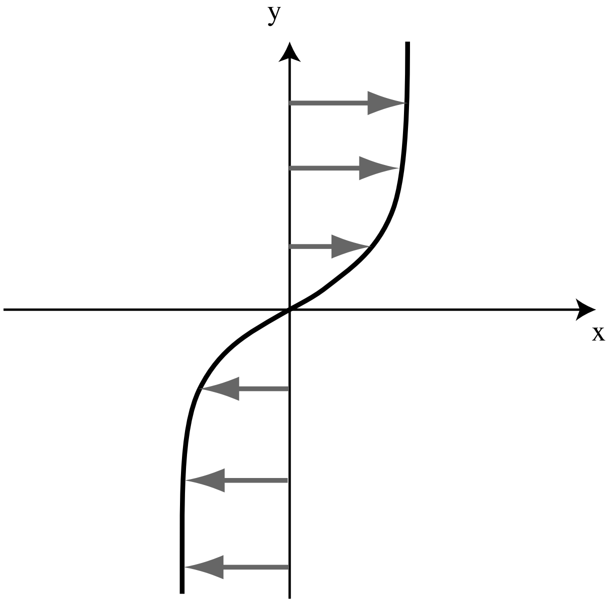

Figure 4.7: Simple shear flow used as a mean flow input.

$$u_0 = M_s \tanh(y/2) \tag{4.3}$$

Because of the nature of the mean flow, its spatial derivatives are computed using a simple 3-point stencil, as is the case with traditional CFD methods. Using the large stencils used for the acoustic part would introduce unnecessary instability. As shown in Fig. 4.8, a monopole situated in the center radiates with the expected symmetric double Pseudo-Doppler effect, similar to the results obtained by Bogey for example [7, 56].

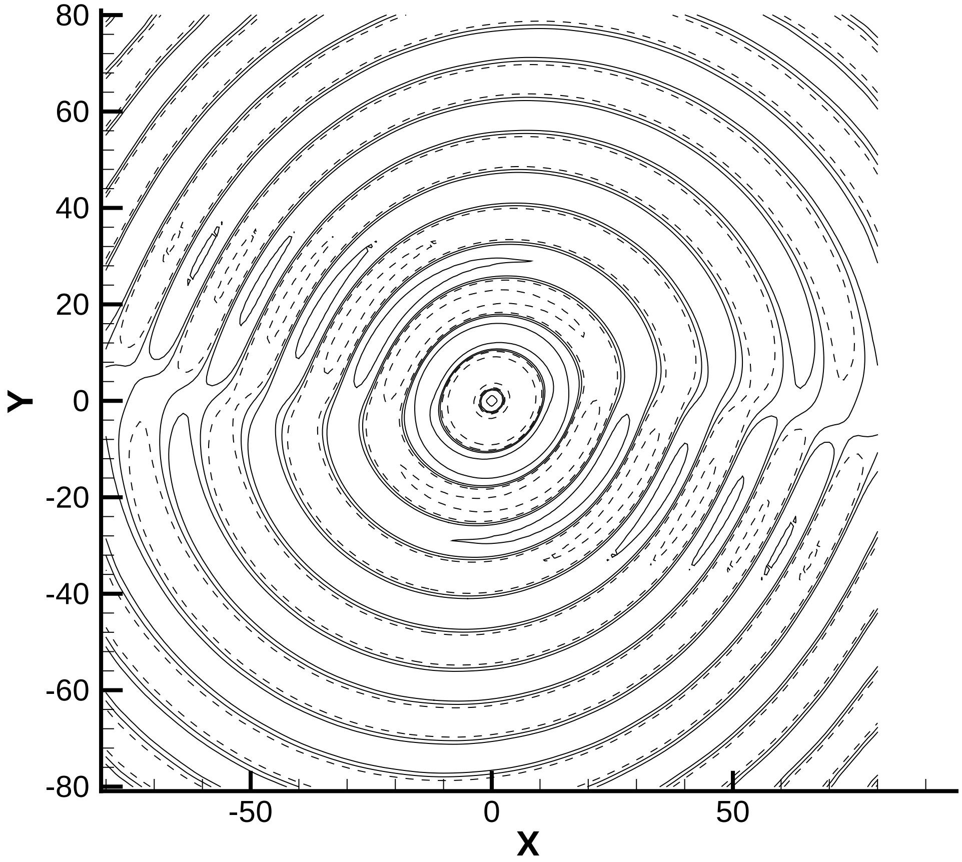

Figure 4.8: Shear flow ($M_s = 0.125$) modifying a monopole's radiation. Pressure contours: 0, $\pm 5\,10^{-3}$, $\pm 2\,.\,10^{-3}$. Negative contours are in dotted lines.

4.1.3 3D propagation

The scheme was then extended to 3D, implementing the full LEEs (Eq. (2.2)–(2.4)) on a similar Cartesian grid. The extension is relatively straightforward, which is one of the main advantages of using a finite difference discretisation.

A monopole case similar to the one studied in Section 4.1.1 was done: Eq. (4.2) can be used, r now being the radial distance to the origin. The results are compared to the analytical solution of Morris [126], as shown in Fig. 4.9, and an excellent agreement was found. The same parameters, and choices of scheme and time-step, as the 2D case were found to give an accurate solution.

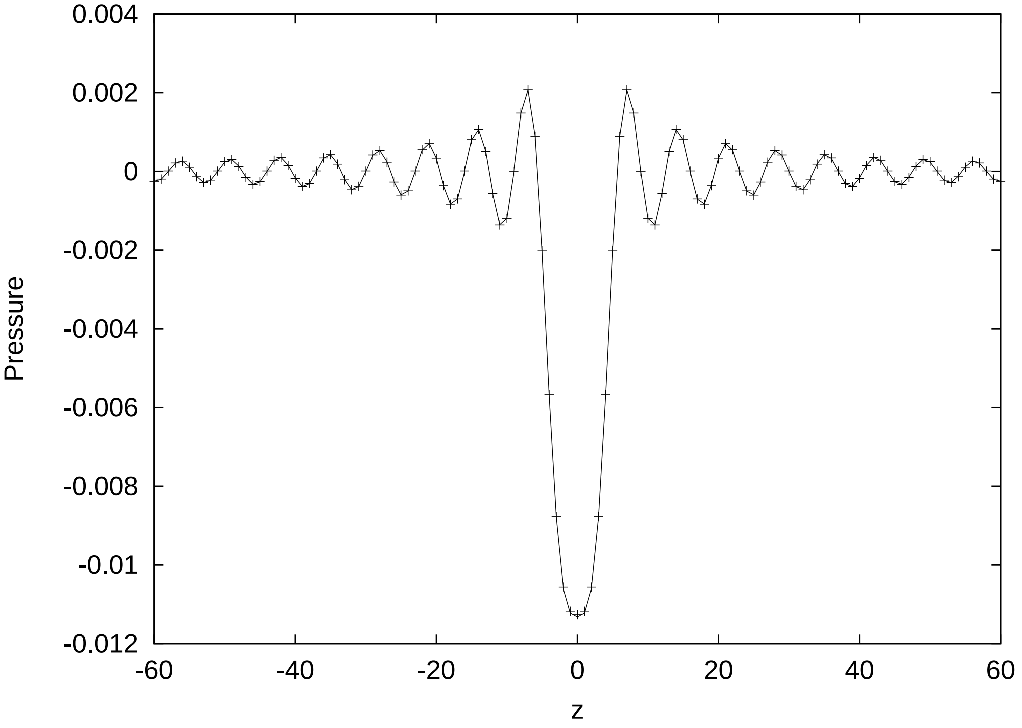

Figure 4.9: Propagation of an acoustic monopole source (dimensionless wavelength $\lambda = 7$) placed at the domain's center in 3D. Plot along $x = y = 0$ line, —: analytical solution, + + +: computed solution.

4.2 Wall boundary in 2D

4.2.1 Straight wall boundaries

The wall boundary condition was then implemented, in the simple case of straight walls coinciding with grid lines, as described in Fig. 3.1 on page 62. For example, the left-side boundary of the domain can be set as a solid wall. In that case, the boundary condition

$$\frac{\partial p'}{\partial x} = 0 \tag{4.4}$$

is expressed on the boundary using the appropriate shifted boundary stencils, and the ghost pressure value is deduced [105].

An oscillating monopole source (Eq. (4.2)) is placed next to the wall. After marching to a periodic state, a characteristic interference pattern caused by the reflection is observed. A reference solution is obtained by replacing the wall with its equivalent: another monopole source, image by symmetry of the original one.

The source signal has a period of $T = 7$ which means that a resolution of 7 PPW is used: Fig. 4.10. An excellent match is obtained, with the OAB scheme and $\Delta t = 0.05$ or $\Delta t = 0.1$, or with the LDDRK with $\Delta t = 0.5$; however, using larger time steps than this leads to noticeable errors, and then instability. Since the large time steps allowed by the 5-stage LDDRK method cannot be used, the 4-stage one is now the optimal temporal scheme, nearly 3 times faster overall than the OAB with $\Delta t = 0.1$.

It is possible to get a good representation of the interference patterns caused by the presence of the wall, by computing, over one signal period T, the Sound Pressure Level (*SPL*) from the Root-Mean-Square (*RMS*) pressure p_{rms} [48].

$$SPL = 20\log_{10}(p_{\mathrm{rms}}/p_{\mathrm{ref}}) = 20\log_{10}\left(\sqrt{\frac{1}{T}\int_{t_0}^{t_0+T} p'^2(t)\,dt}\Bigg/ p_{\mathrm{ref}}\right) \tag{4.5}$$

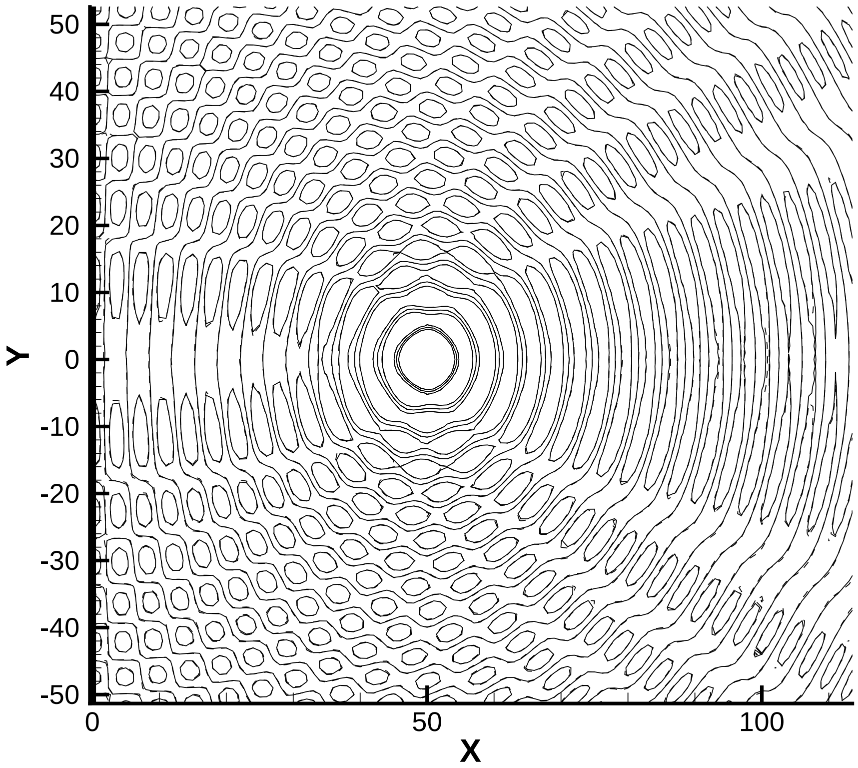

Figure 4.10: Interference pattern created by a wall ($x = 0$) next to an oscillating monopole ($x = 50$), with a wavelength of $\lambda = 7$. Contours of pressure: 0 and ±0.01, — computed value, - - reference solution.

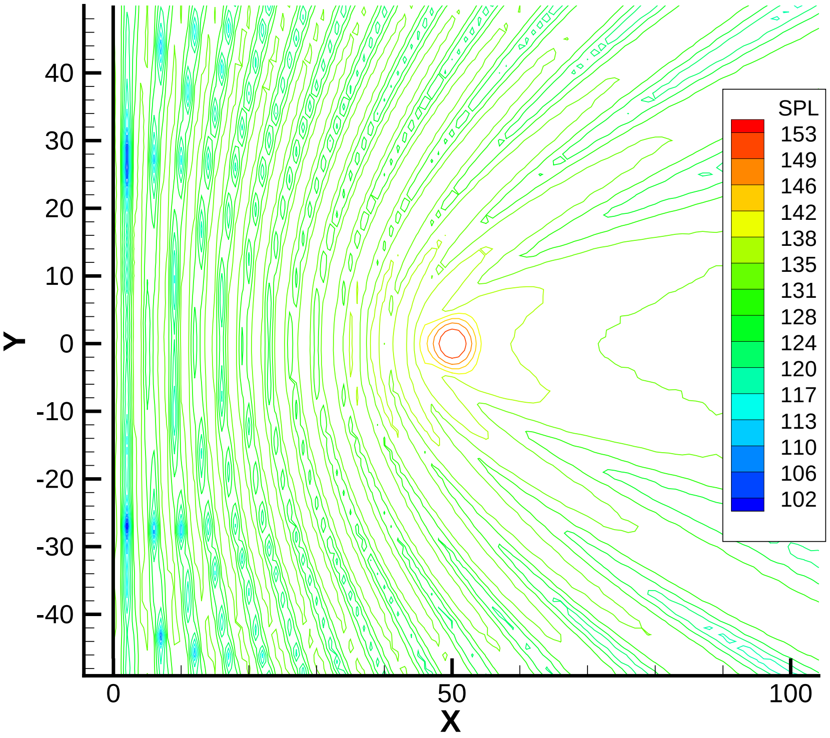

Figure 4.11: Sound pressure levels for the result of Fig. 4.10.

The reference pressure p_{ref} is typically chosen as $2\,.\,10^{-5}$ Pa, and t_0 is an arbitrary starting time. The resulting SPL is plotted in Fig. 4.11: this makes the interference pattern introduced by the wall clearly visible. This phenomenon is similar to the "ground effect" that disturbs noise measurements made close to the ground [1].

As was done in Refs. [105] and [46], an acoustic pulse (described by Eq. (4.1)) is placed next to the straight wall, with a flow parallel to it. It can be seen being reflected and convected downstream at the same time in Fig. 4.12(a) and Fig. 4.12(b). A reference solution was also produced in this case by using a symmetric pulse, and there is excellent agreement with the one computed with the wall boundary: Fig. 4.12(c).

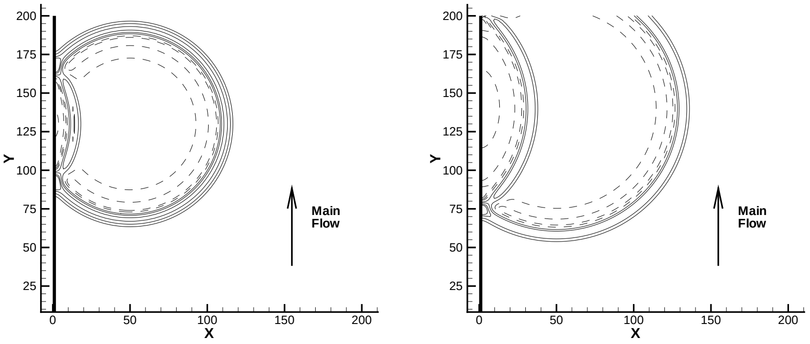

(a) $t = 60$ (b) $t = 80$

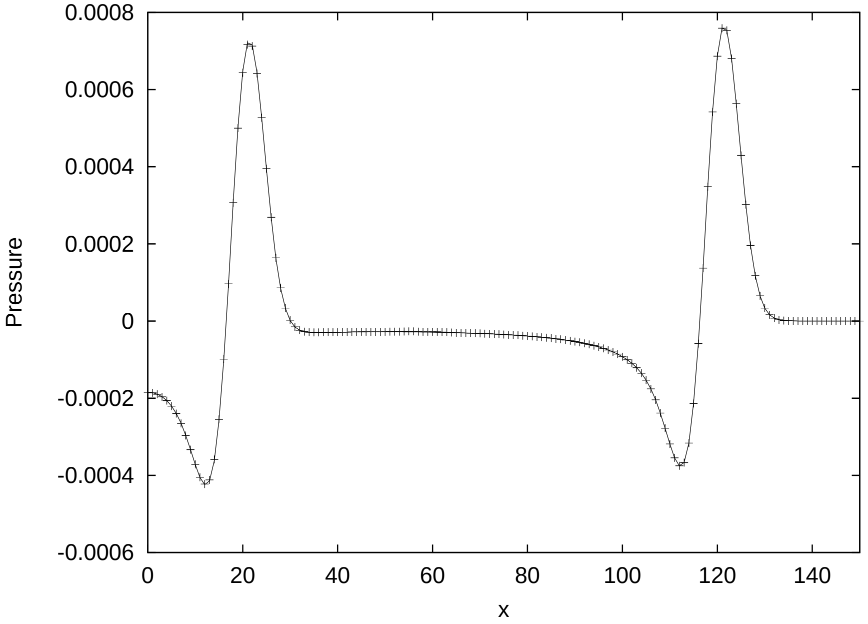

(c) $t = 80$, plot along $y = 100$, —: reference solution, + + +: computed solution.

Figure 4.12: Reflection of an acoustic pulse by a wall along the left boundary. Mean flow Mach number $M_y = 0.5$. a) and b): Density contours, —: $10^{-3}, 8.10^{-4}, 5.10^{-4}, 2.5.10^{-4}$ and - - -: $-10^{-4}, -3.10^{-4}, -4.10^{-4}$.

4.2.2 Curved wall boundaries

The 2D curved wall method of Kurbatskii was then implemented. This method has been validated thoroughly for a variety of different cases, even at high-order resolutions ($\lambda = 8\Delta x$) [121]. To prove that the implementation was correctly done, problem 1 from category 1 in the second CAA workshop on benchmark problems [60] was considered; it consists of computing the scattering of the oscillating acoustic source of Section 4.1.1 by a solid cylinder of radius a.

An interesting characteristic of the resolution is the dimensionless wavenumber, or Helmholtz number:

$$\tilde{\alpha} = 2\pi a/\lambda \tag{4.6}$$

The computation is first done with a resolution of 7 PPW with $a = 20$, which gives $\tilde{\alpha} \simeq 18$, which represents a challenging test case. Using an insufficient level of dissipation close to the wall boundary leads to crippling instability, as shown in Fig. 4.13(a). If the optimal selective dissipation technique described in Section 3.2.4 (with R^w_Δ in the range 0.3–0.4) is used then a correct solution is obtained: Fig. 4.13(b). Once the computed solution has reached a periodic state, the interference pattern caused by the scattering is apparent, as well as the "shadow zone": the silent zone created by the masking of the cylinder. Furthermore, the waves appear to exit the boundaries with no noticeable reflections. A plot of the SPL is shown in Fig. 4.14, making the features of the scattered field more clearly apparent.

In Fig. 4.15, the computed solution, cut along the $y = 0$ line, is compared to an analytical solution by Morris [125]. It is clear that an excellent agreement is obtained, even at this relatively low grid density.

Extensive numerical testing was performed for various test cases, to further validate the method and to confirm the parameters of the artificial selective numerical dissipation, as described in Section 3.2.4. The optimal set-up was found in agreement with Kurbatskii [121]: the dissipation terms are applied to all equations, but the smallest, 3-point dissipation stencils do not include the ghost values of pressure. The same distribution of R^w_Δ is used regardless of the Helmholtz number of the problem. If the dissipation is not applied to the pressure equation, then a larger R^w_Δ amplitude (> 0.7) needs to be used to ensure stability, which leads,

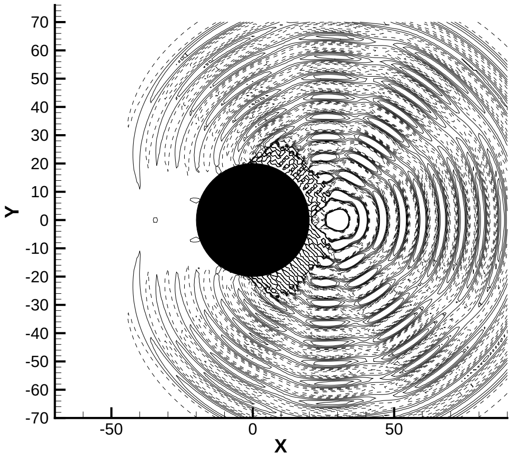

(a) Low dissipation leading to instability.

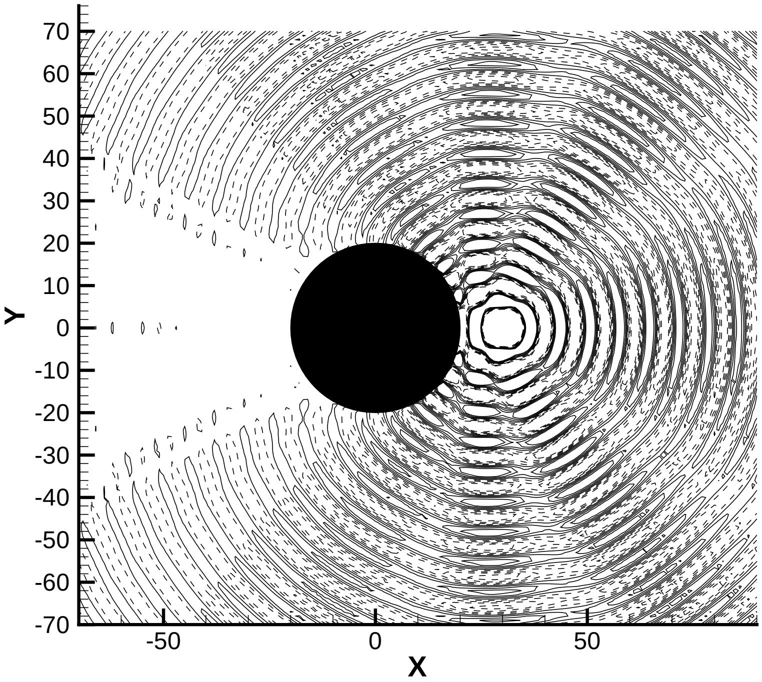

(b) Optimised extrapolation leading to a periodic solution.

Figure 4.13: Monopole oscillator scattering on an infinite cylinder, $\tilde{\alpha} \simeq 18$. 8 contours of pressure between $\pm 10^{-3}$. Negative contours are in dotted lines.

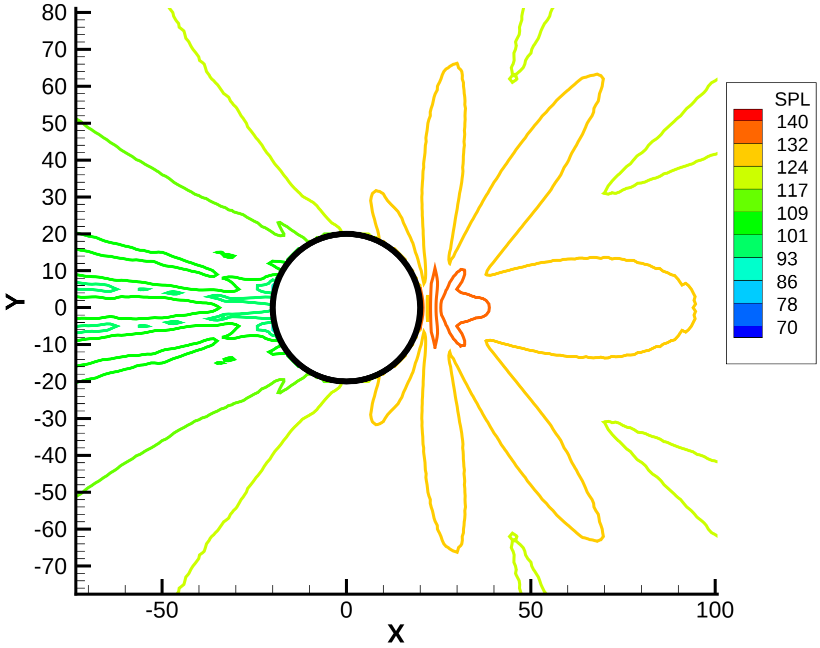

Figure 4.14: Sound pressure levels of the computed solution of Fig. 4.13.

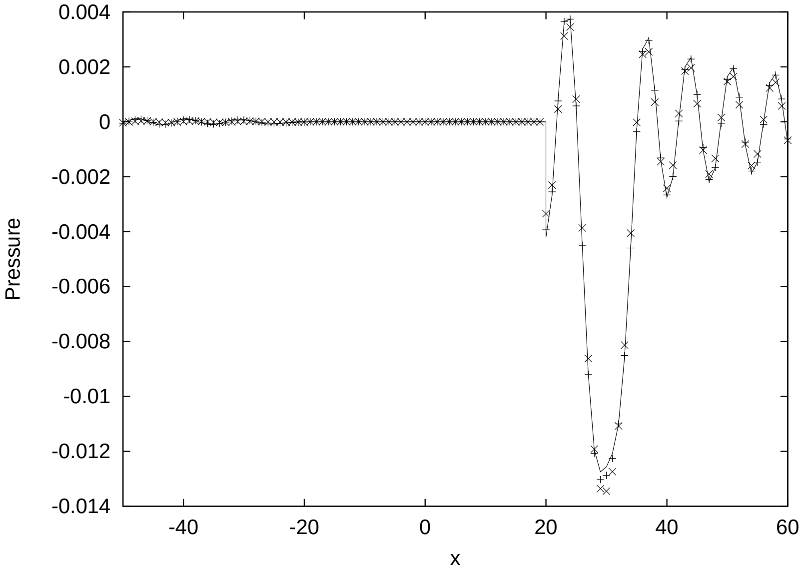

Figure 4.15: Cut along the $y = 0$ line of a source of $\lambda = 7$ at $x = 30$, scattered by a cylinder of radius $a = 20$. — : analytical solution; computed solution: + + + with optimal dissipation, × × × with large R_{Δ}^{w} coefficient.

noticeably in Fig. 4.15, to a dissipated and dispersed solution; more particularly in the shadow zone, because the sound waves must travel along the whole surface of the cylinder.

The simulation was run with the (4-stage) LDDRK scheme, with time-steps no larger than $\Delta t = 0.3$, with no apparent difference with the result obtained with a OAB scheme ($\Delta t = 0.1$), but the latter scheme runs faster overall because it only evaluates one residual per time step, and gives slightly more accuracy and stability. The instability introduced by the curved wall surface makes the use of large time steps impossible, and makes the OAB scheme the optimal scheme to use. One could argue that this does in effect reduce the effective temporal order of the scheme. In the studies of Refs. [121] and [46], very small time steps ($\Delta t = 0.05$) were also used in all cases. In the work of Özyörük [9], although high CFL numbers are used (typically 0.5) with a Runge-Kutta method, this results in small time steps (384 per period) because of the deformed grid: it is necessary to use the smallest time step allowed by the grid metrics over the whole domain. With the current approach, the instability is limited to the vicinity of the wall boundaries, and not present in most of the domain where a simple uniform grid is used. Chapter 3 presented many of the other advantages of such an approach.

4.2.3 Flow around the wall surface

The effect of a mean flow surrounding the immersed boundary will now be investigated (this was not done in Ref. [121]). In the general case, a steady solution of the flow in the presence of the wall boundary can be obtained simply by using a traditional CFD program; this can then be interpolated on the Cartesian grid obtained. In the case of a 2D inviscid potential flow around a cylinder of radius a, the solution can be expressed simply in the 2D cylindrical coordinate system (r, θ) centered on the cylinder [127]:

$$v_r = U_\infty \left(1 - \left(\frac{a}{r}\right)^2\right) \cos\theta \tag{4.7}$$

$$v_\theta = -U_\infty \left(1 + \left(\frac{a}{r}\right)^2\right) \sin\theta \tag{4.8}$$

$$p = p_\infty + 1/2\rho U_\infty^2 (1 - 4\sin^2\theta) \tag{4.9}$$

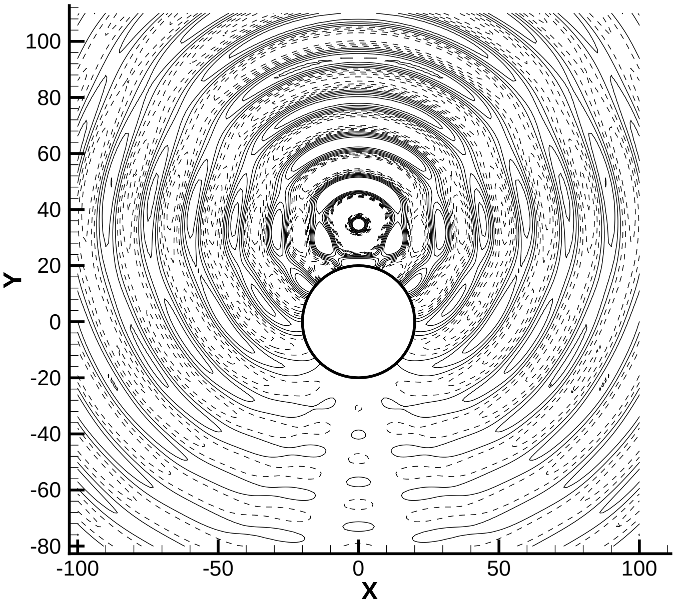

(a) Without Flow.

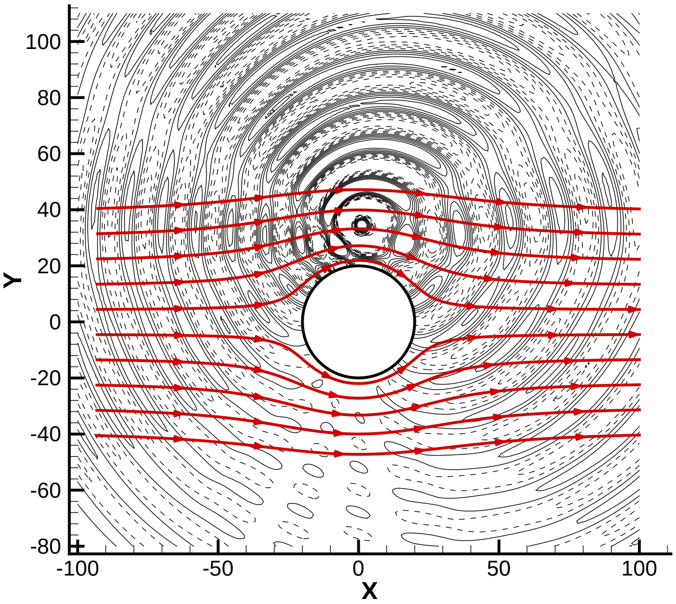

(b) With Flow. The streamlines of the steady flow (Eq. (4.7)–(4.9)) are shown in red.

Figure 4.16: Effect of the of a Mach 0.2 flow around the cylinder. 10 contours of pressure between $\pm 5\,10^{-3}$. Negative contours are in dotted lines.

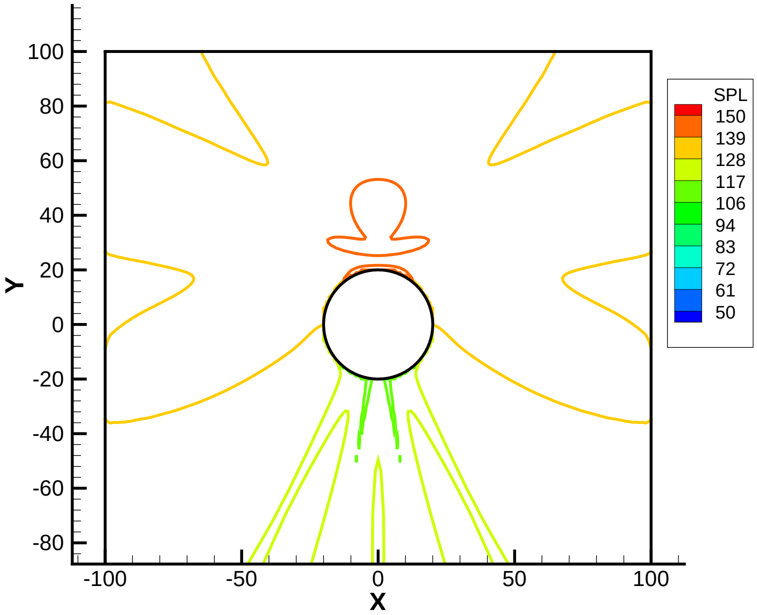

(a) Without Flow.

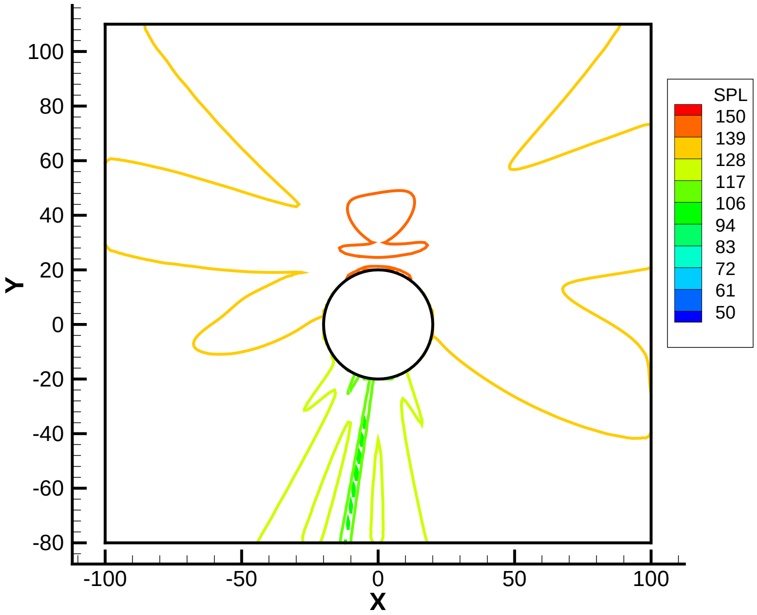

(b) With Flow.

Figure 4.17: Effect of the Mach 0.2 flow around the cylinder on the SPL.

U_∞ is the undisturbed velocity upstream of the cylinder. This flow modifies the propagation and the scattering of the sound in complex ways; Redonnet [46] studied this effect for a monopole source, placed downstream and below the cylinder. A similar study was done with the current code and is shown in Fig. 4.16, with a mach number of 0.2 modifying the scattering of a monopole source ($\lambda = 15$). The refraction effect of the flow is clearly apparent on the SPL plot of Fig. 4.17. Furthermore, in both cases, the contours are very smooth near the boundaries: the sound exits the boundary with no noticeable artificial reflections. In Fig. 4.18, the pseudo-Doppler effects on the wavelength are apparent. A computation made with double the resolution is superimposed, giving a similar result, which shows the converged behaviour of the discretisation scheme: there appears to be less dissipation and dispersion errors at this increased resolution. For Mach numbers higher than 0.3, some instability appears on the downstream side of the circular boundary, probably caused by the convection effects which accentuate its unstable character.

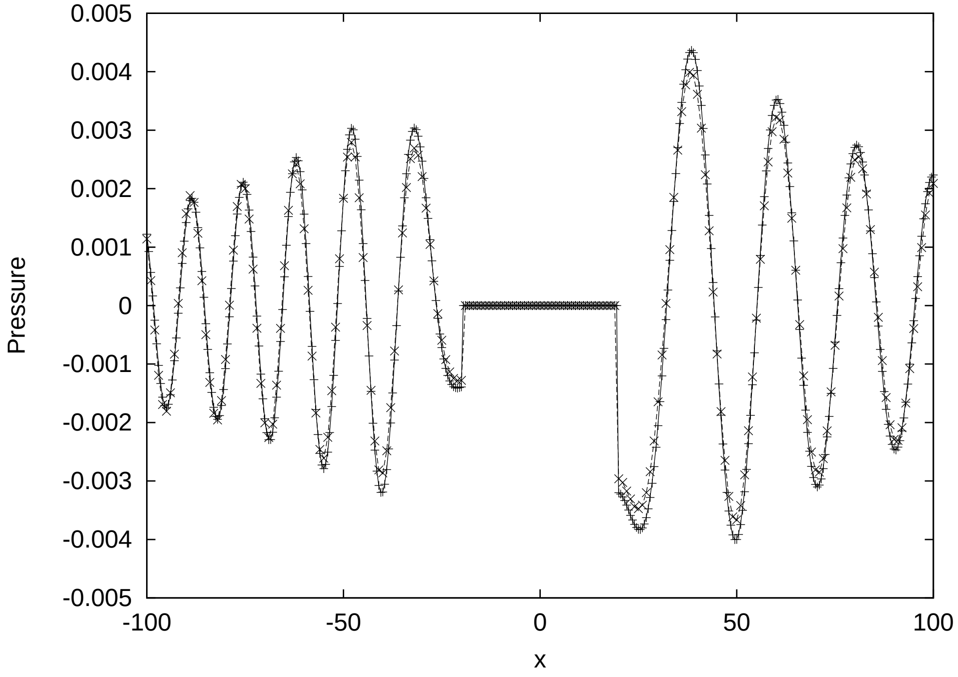

Figure 4.18: Plot along $y = 0$ of the solution of Fig. 4.16: $- - \times - -$, and the computation with double resolution: —+—.

4.3 Wall boundary in 3D

4.3.1 Scattering from a sphere

The 3D method described in Section 3.2 was implemented. Basic tests have already been performed in Section 3.2.2, making sure that the normals were correctly evaluated and that no artificial asymmetry was introduced by the surface analysis algorithm.

A scattering problem [126], similar to problems 3 and 4 of category 1 in the second conference on acoustic benchmark tests [60], is used to validate the boundary condition. In this case, a sphere scatters, in 3D, a monopole acoustic source situated on the z axis. This problem has been used to validate other 3D methods: Zhuang and Chen [83] use an adapted spherical coordinate system, with excellent results, but this cannot be used in more complex cases. Morris [81] used a simple staircase boundary.

After some iterations, a periodic state is obtained. The effects of the scattering are apparent on Fig. 4.19: the interference pattern from the reflected signal and the shadow zone behind the sphere. Fig. 4.20 and Fig. 4.21 show the computed solution, compared to the analytic one, for different parameters. A range of resolutions is studied, as described by the dimensionless wavenumber $\tilde{\alpha} = 2\pi a/\lambda$, where a is the radius of the sphere. The case of Fig. 4.20(a) has $\tilde{\alpha} = 6.8$; in Fig. 4.20(b) $\tilde{\alpha} = 12.6$; finally in Fig. 4.21, where the spatial resolution is 7 PPW, $\tilde{\alpha}$ goes up to 17.9. This performs a convergence study of this problem.

In all cases, there is excellent agreement in the zone closest to the source. But, examining the solution on the x axis (Fig. 4.21(b)), or, more strikingly, in the shadow zone behind the solid, it appears that increasing dissipation errors seem to accumulate as the waves are diffracted around the wall surface. This is similar to what was observed in 2D, but with an increased magnitude. This is probably because three extrapolations need to be done for most ghost points, instead of a maximum of two for the 2D method. The unavoidable error introduced by discretising the curved surface, more important in 3D as was shown in Section 3.2.2, is also probably a factor. The wave, as it travels along the wall, is more dissipated than it is dispersed, which is consistent with general results by Lockard concerning high-order methods [63]. The relative proximity of the domain boundaries could be problematic, but increasing the domain's size only has a marginal effect, and mostly in the region closest to the source ($z > 0$).

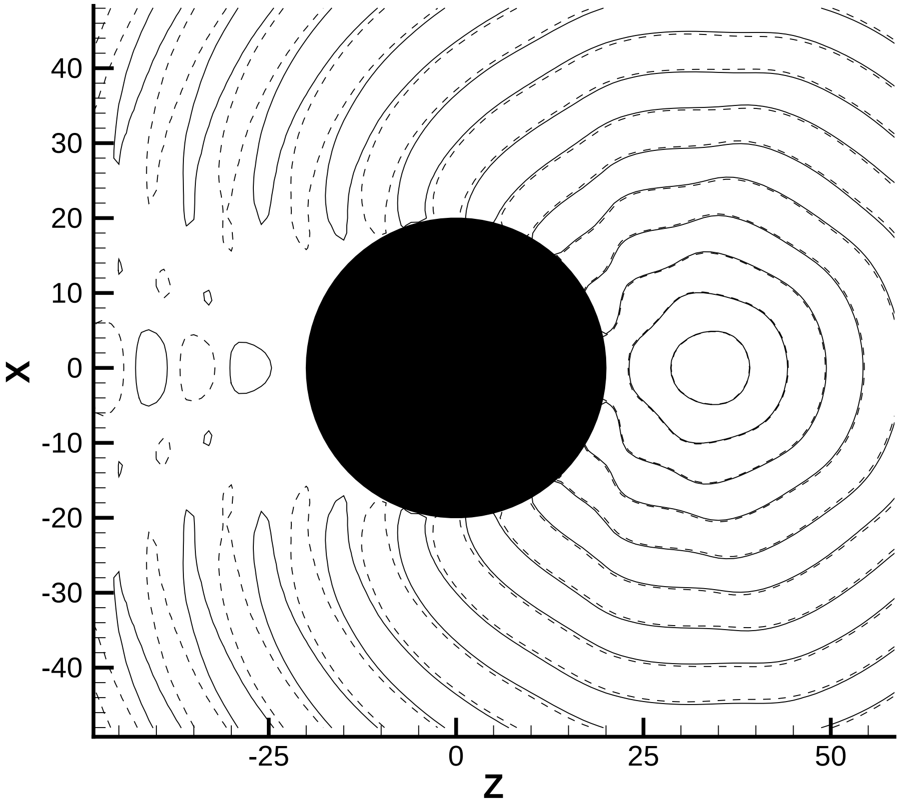

Figure 4.19: 3D scattering of a source ($z = 34$, wavelength of $\lambda = 10$) by a sphere of radius $a = 20$. Plot in the $y = 0$ plane, of acoustic pressure contours: $\pm 10^{-4}$, the dashed lines represent negative values.

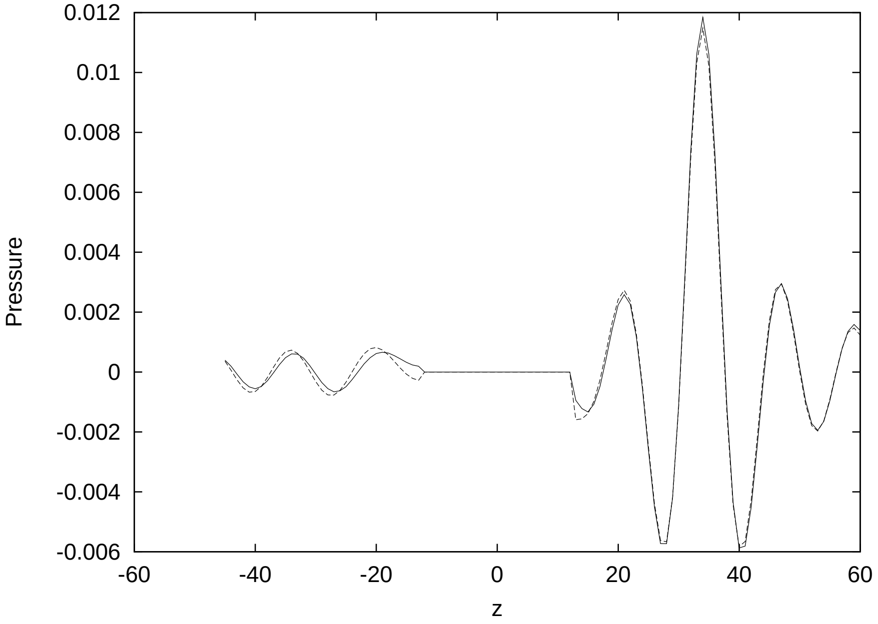

(a) Sphere of radius $a = 13$, source at $z = 34$, of wavelength $\lambda = 12$: $\tilde{\alpha} = 6.8$.

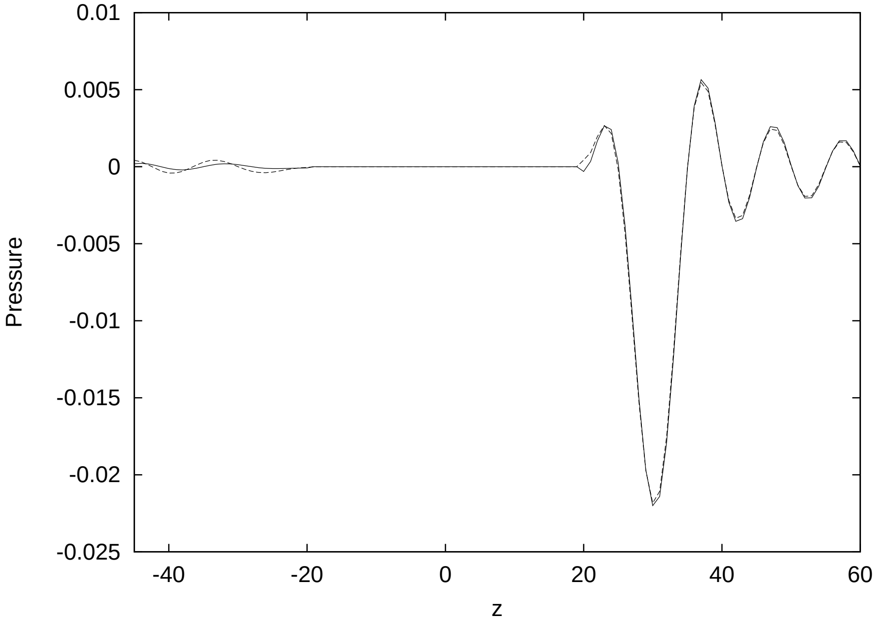

(b) Sphere of radius $a = 20$, source at $z = 30$, of wavelength $\lambda = 10$: $\tilde{\alpha} = 12.6$.

Figure 4.20: 3D scattering of a Gaussian monopole source by a sphere. Plot at time $t = 100$, along the z axis. — computed values, $- - -$ analytical solution.

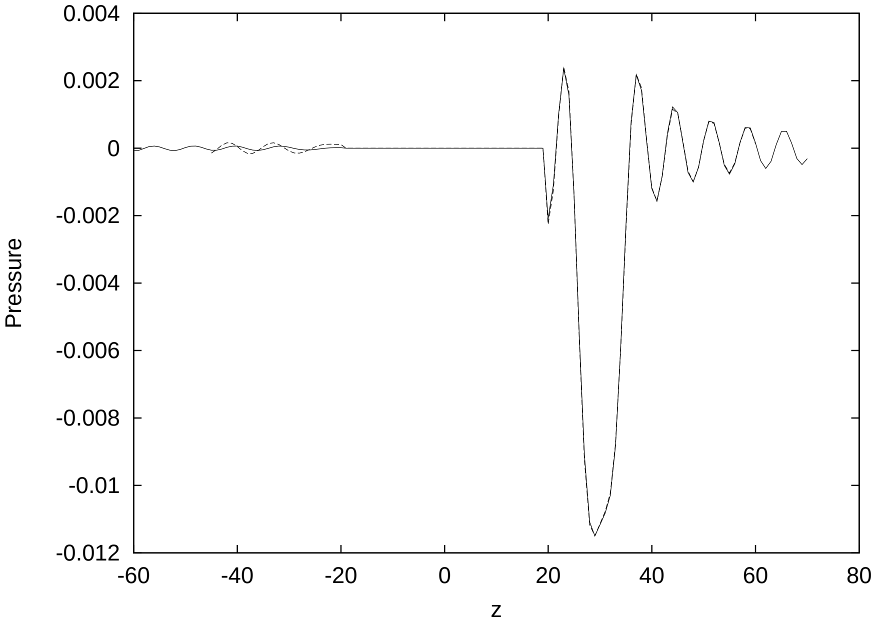

(a) Plot along the z axis.

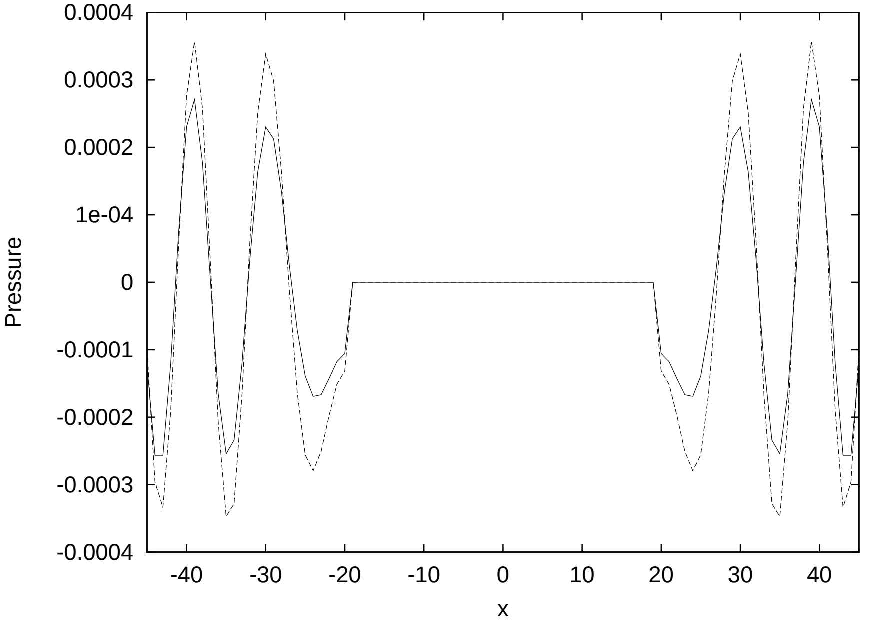

(b) Plot along the x axis.

Figure 4.21: 3D scattering of a Gaussian monopole source ($z = 30$, wavelength of $\lambda = 7$) by a sphere of radius $a = 20$: $\tilde{\alpha} = 17.9$. Plot at time $t = 100$. — computed values, $- - -$ analytical solution.

Computations were also performed with double and half the spatial resolution, for a fixed geometry, with a sphere of radius $a = 20$ and sources of wavelength $\lambda = 15$: Fig. 4.22. Because of computational limitations, the domain could not be extended as far, which results in artificial reflections degrading the solution. But the area of interest in this case is the shadow zone. The dispersion and dissipation errors appear to diminish, but not completely.

The results of Figs. 4.20 and 4.21 and the slow convergence exhibited indicate that, although the full high-order accuracy could not be obtained here, it is still quite important. Overall, the error diminishes as $\tilde{\alpha}$ decreases, which indicates some convergence of the algorithm according to this parameter; furthermore, the overall quality of the solution in all cases is satisfactory. But the new 3D wall boundary condition is not validated beyond any doubt at this stage.

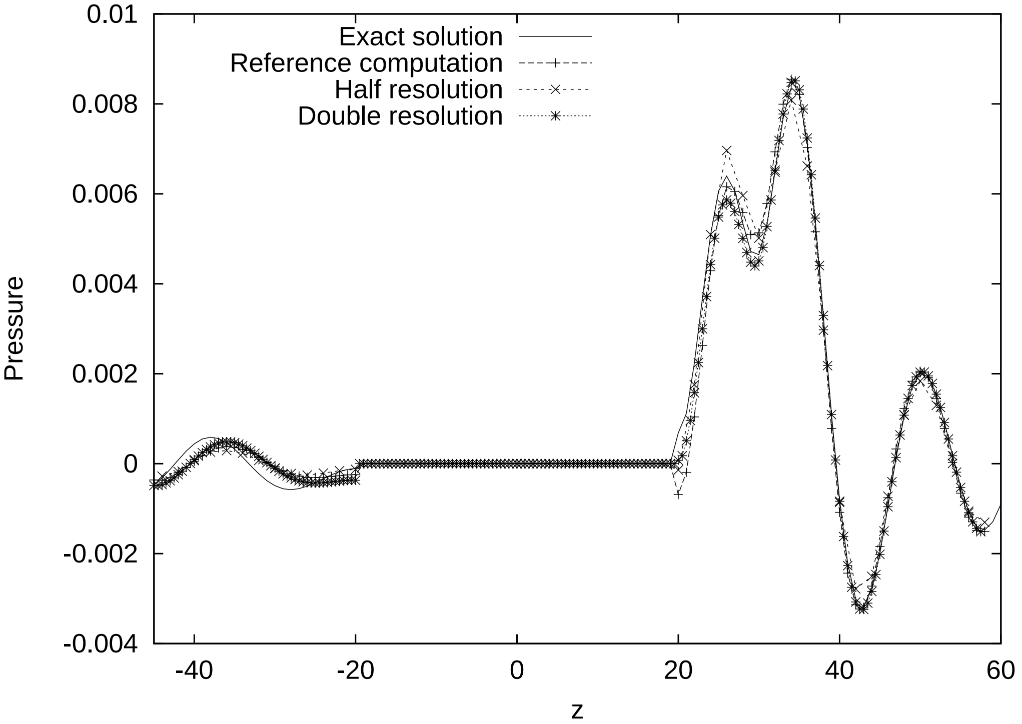

Figure 4.22: Computation with several resolutions of the 3D scattering by the sphere. Same parameters as Fig. 4.21 with $\lambda = 15$.

4.3.2 Mean flow effects

In Fig. 4.23(a), an undisturbed source of wavelength $\lambda = 15$ is situated next to a sphere of radius $a = 20$. An inviscid potential flow is then added around the solid boundary, as in Section 4.2.3. In this case as well, the flow has a far-field velocity U_∞ with a Mach number of 0.2. Supposing a symmetry around z, the solution can be expressed in the polar coordinates (r, θ) of the $y = 0$ plane [128]:

$$v_r = \quad U_\infty \left(1 - \left(\frac{a}{r}\right)^3\right) \cos\theta \tag{4.10}$$

$$v_\theta = -U_\infty \left(1 + \left(\frac{a^3}{2r^3}\right)\right) \sin\theta \tag{4.11}$$

$$p = p_\infty + a^3 U_\infty^2 \frac{4r^3 - 5a^3 + 3(4r^3 - a^3)\cos 2\theta}{16r^6} \tag{4.12}$$

The full 3D LEE equations are solved, using smaller time steps of $\Delta t = 0.04$, to maintain a large enough CFL number (*cf.* Section 2.2.3). The effect that the velocity gradient has on the acoustic propagation is apparent in Fig. 4.23(b), and qualitatively similar to that of the 2D case. In this case as well, only low mach numbers flows should be modelled, to avoid instability.

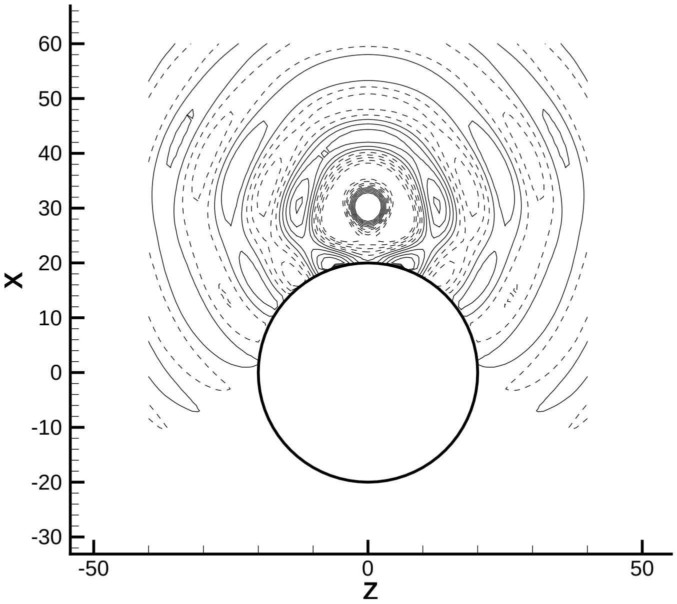

(a) Without Flow.

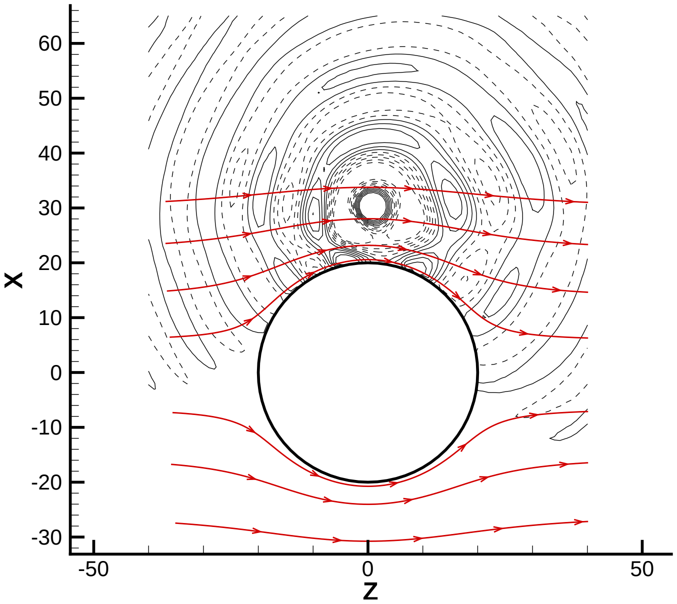

(b) With Flow. Streamlines of the steady flow are shown in red.

Figure 4.23: Effect of the of a Mach 0.2 flow around the sphere. 10 contours of pressure between $\pm 4\,10^{-3}$. Negative contours are in dotted lines.

Concluding remarks

First of all, the implementation of the chosen numerical scheme was investigated and verified using standard test cases found in the literature, as summarised in Table 4.1. Its high accuracy was confirmed, and observations made by other authors were replicated. A detailed analysis of two time integration schemes was made, establishing that for simple cases, the theoretical stability and accuracy limits are verified and that the frequency-optimised Runge-Kutta scheme was the optimal choice. But when more complex cases including wall boundaries were considered, smaller time steps needed to be used to prevent instability, and the 4-level OAB scheme became the best option.

The 2D immersed boundary method of Kurbatskii was implemented, and many results were replicated. It was also observed that the mean flow effects are compatible with this boundary condition, for flows of low Mach numbers, which could be a problematic limitation. The new 3D algorithm described in Chapter 3 was implemented, and tested on a standard benchmark problem. The high-order accuracy that the immersed boundary condition possessed in 2D could not be fully replicated in 3D, mainly because of extra inaccuracies in the extrapolation process. The overall scheme remains high-order accurate in most of the domain. The more representative applications in the following chapter will provide more interesting validations, and assess the efficiency of the method compared to traditional CFD schemes.

Type	2D	3D
Pulse	p. 86	
Monopole	p. 88	p. 94
Straight walls	p. 95	
Curved walls	p. 99	p. 106

Table 4.1: Summary of the main validations cases used in this chapter.

Chapter 5

Study of representative industrial cases

The CAA LEE code described in Chapter 2, together with the 3D wall boundary method described in Chapter 3, were applied in Chapter 4. This methodology will now be referred to as the High-Order Propagation (*HOP*) method. In this chapter, the HOP method is applied to representative industrial geometries. The plane wave propagation case from Chapter 2 is first solved, illustrating the gains obtained when a high-order discretisation is used. Then, the problem of sound propagation from engine inlets, of great importance as described in Chapter 1, is studied to further evaluate the wall algorithm of Chapter 3. The propagation of several different acoustic modes is computed for two different axisymmetric inlet geometries: one based on the JT15D engine, and the other on an elliptic profile. The HOP results are compared with simple analytical results, and with results obtained by a 2D frequency-domain CAA code and by a traditional CFD code. Finally, a fully 3D problem is studied, investigating the effects of inlet scarfing with a simple model.

5.1 Preliminary study

5.1.1 Simple plane wave propagation

The problem described in Section 2.2.1 will now be modelled with the HOP method to compare the results to those obtained using the low-order code described in Section 1.2.2: namely AU3D. The following parameters are used here: $\Delta x = \Delta y = \Delta z = 0.07$m, so that the computational grid has the dimensions 80×28×28 to model the finely meshed region of the grid of Fig. 2.2. The wave has a circular frequency of $\omega = 2\pi/7$ which means that the maximum resolution of 7 PPW is used, and the simulation is run for 10 periods. The mean flow is perfectly at rest. The HOP computations were ran with $\Delta t = 0.05$ to obtain 140 time-steps per period, as in the AU3D computations.

This is essentially a wave-guide problem, as symmetric boundary conditions are imposed on all boundaries parallel to the direction of propagation. The condition used, on the positive x boundary, to impose incoming waves is crucial for the quality of the solution, as was described in Section 2.3.3. The computations were initially done with the non-reflecting formulation of Eq. (2.17), which was applied in the 3-point wide boundary region. Such an approach introduces a discontinuity in the transition from this boundary zone to the main domain, which in turn creates spurious short waves contaminating the solution, and thus instability. Therefore, the explicit absorbing boundary condition of Zhang *et al.* [52], Eq. (2.18), was used. It is very well suited for use with the current type of high-order method, because of the very smooth transition between the absorbtion zone and the main domain; furthermore, it does not require the computation of any approximate derivatives (another potential source of inaccuracy). Numerical tests were performed to establish the quality of the results with σ_m at least equal to 0.4, $\beta = 3$ for a smooth transition and the absorbtion zone being at least 10 grid-lengths wide (see Eq. (2.19)).

Fig. 5.1 is a good illustration of the advantages of using a high-order discretisation. It shows the new solution superposed over the results of Section 2.2.1 (Fig. 2.2), and even at this low resolution, there is an excellent match with the theoretical solution and no significant dissipation or dispersion. The AU3D results, here and in the rest of this Chapter, show the acoustic pressure p', normalised by the reference pressure of $p_{ref} = 10000$ Pascals. A slight steepening of the solution can be observed at the maximum resolution, because of the non-linear character of the model. The HOP results, of arbitrary amplitude, were scaled to match high-resolution AU3D ones at the input plane.

The running times obtained with the AU3D code were reduced by 12% to take into account the stretched grid zone which has been added to prevent artificial reflections (the running time being a linear function of the number of points in the grid). They are shown in Table 5.1, together with HOP run-times, the dispersion or phase error given as a percentage of the wavelength and the amplitude error. The overall running time for HOP was around an order of magnitude smaller than that of the traditional CFD method.

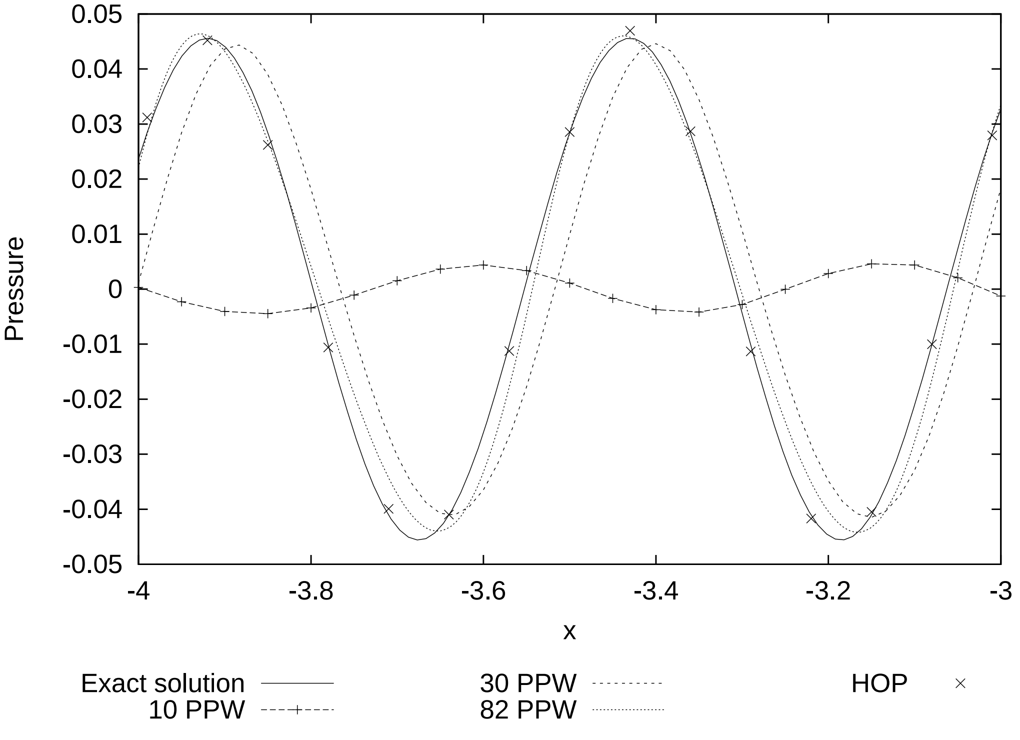

Figure 5.1: Plane wave propagation, acoustic pressure plot along centerline. Comparison of the different AU3D solutions, the 7 PPW HOP result and an analytical solution.

Method	Running time (minutes)	Ratio	Phase error	Amplitude error
HOP, 7 PPW	11	1.0	0%	< 1 %
AU3D, 10 PPW	26	2.4	60%	90 %
AU3D, 30 PPW	92	8.4	6%	2.5%
AU3D, 82 PPW	270	24.0	< 2%	< 1%

Table 5.1: Computational times for the simple plane wave case, scaled for direct comparison, and accuracy obtained.

The AU3D code uses a dual time-stepping technique [26]; the outer iteration level, using a Newton method, determines the time accuracy of the code. Computations were done using 3 outer iterations per time step, to ensure a good convergence. Only doing 1 of these iterations cuts computing time nearly by half, but, as can be seen in Fig. 5.2, this leads to a significant degradation of the solution in terms of dissipation and, more importantly, dispersion, even though relatively small time steps are used.

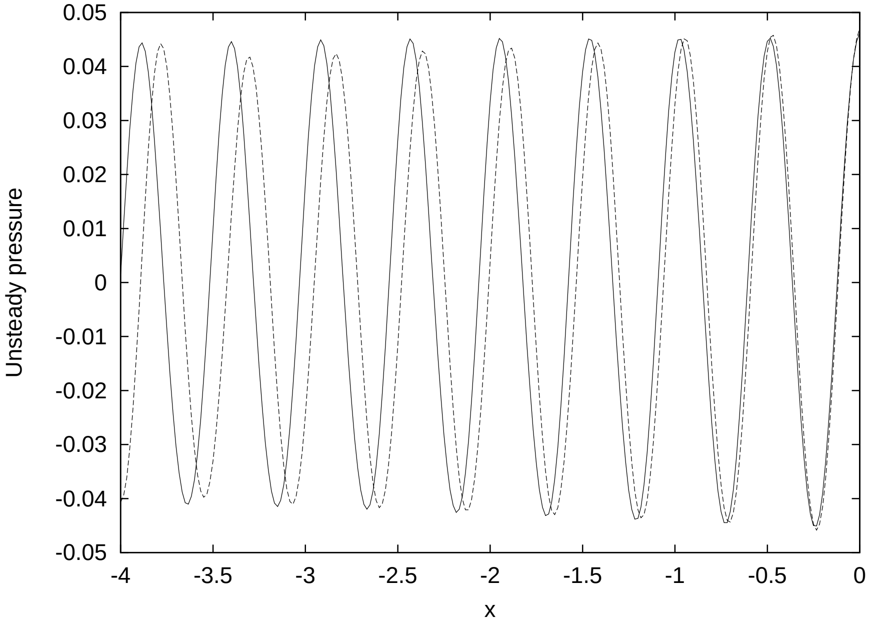

Figure 5.2: Acoustic pressure plot along centerline for 30 PPW case, with: ——— 3 Newton iterations per time step, - - - 1 Newton iteration.

The time step used in HOP can be increased from $\Delta t = 0.05$ to 0.1 for example, while retaining an accurate solution, thus doubling the computational gains. However, as was explained in Chapter 4, this would be incompatible with the curved boundary condition used in the rest of the study, and create instability. This means that the gains obtained mainly come from the different spatial schemes, as the time-step size used is of the same order. Nevertheless, the superiority of the HOP method is still apparent. The observations made on this simple case will be used for the more complex cases below.

5.1.2 Spinning modes of an infinite cylinder

Some of the essential nomenclature and conventions used in the rest of this chapter will be now be clarified, by considering the eigensolutions of the convected wave equation in an infinite cylindrical duct [9, 13]. These "spinning modes" are typical of the sound field generated by the fan or rotor-stator interactions in the core of the engine. Up to now, the source of sound $\boldsymbol{Q'_{in}}$, to be numerically propagated through the inlet or the bypass sections, was assumed to be known or given by a non-linear CFD computation. For the purpose of the study and validation of the methodology, in the following sections the source will be directly imposed as one or several modes, whose analytical formulation is described below.

Let r_w be the radius of an infinite cylinder, centered on the $\vec{x}$ axis, in which the mode propagates, c_d the local speed of sound, M_d the Mach number of an eventual uniform convective flow. The acoustic pressure p' is expressed, in the cylindrical coordinates (x, r, θ) of the duct, as a sum of modes

$$p' = \Re\left(\sum_{n,m,\mu} \hat{p}_{nm\mu}\right) \tag{5.1}$$

each of the form:

$$\hat{p}_{nm\mu} = A_{nm\mu} J_m(\alpha_{m\mu} r) e^{i[\alpha_{x,m\mu} x + m\theta + \phi]} e^{-i\omega n t} \tag{5.2}$$

with $A_{nm\mu}$ being the amplitude and ϕ an optional phase. A mode is usually referenced by the (m, μ) pair, the azimuthal and the radial mode orders respectively, and n is the time harmonic index. J_m is the bessel function of the first kind, of order m. $\alpha_{m\mu}$ is the *radial* wavenumber, determined as the μ^{th} eigenvalue that satisfies ${J_m}'(kr) = 0$ at $r = r_w$. In an engine inlet, the circular frequency ω depends on the rotating frequency of the fan, generally characterised by the Blade Passing Frequency (BPF), which depends on the operating conditions [9]. $\alpha_{x,m\mu}$ is the *axial* wavenumber. For waves propagating in the negative x-direction, upstream in the traditional convention, it is given by:

$$\alpha_{x,m\mu} = \frac{-M_d\alpha - \sqrt{\alpha^2 - (1 - M_d^2)\alpha_{m\mu}^2}}{1 - M_d^2} \tag{5.3}$$

where $\alpha = \frac{n\omega}{c_d}$ is the wavenumber. Depending on the Mach number M_d and the ratio $(\alpha_{m\mu}/\alpha)$, the axial wavenumber $\alpha_{x,m\mu}$ can sometimes be purely imaginary: the mode is then *cut off*, *i.e.* it decays as it propagates; otherwise, it is *cut on*, and it will effectively propagate. A cut-off ratio is then usually defined as

$$\xi = \sqrt{(1 - M_d^2)}\alpha_{m\mu}/\alpha \tag{5.4}$$

and will be less than 1 for propagating modes only. Modern aircraft engines are designed so that most of the modes generated from the rotor/stator interactions will be cut off under typical operating conditions.

In the case of an annular duct, described by an inner radius r_i and outer radius r_o, a similar set of modes can be obtained [52]. To satisfy both boundary conditions, the radial eigenfunction J_m is replaced by a sum of Bessel functions of the first and second kind:

$$J_m(\alpha_{m\mu}r) \longrightarrow J_m({\alpha'}_{m\mu}r) + \zeta Y_m({\alpha'}_{m\mu}r) \tag{5.5}$$

where ζ and the corresponding new radial wavenumber ${\alpha'}_{m\mu}$ are determined by solving the equation:

$$\zeta = \frac{{J'}_m({\alpha'}_{m\mu}r_o)}{{Y'}_m(\alpha_{m\mu}r_o)} = \frac{{J'}_m({\alpha'}_{m\mu}r_i)}{{Y'}_m({\alpha'}_{m\mu}r_i)} \tag{5.6}$$

5.2 First case study: JT15D inlet

5.2.1 Description

The JT15D is a small Pratt & Whitney turbofan engine, with a bellmouth inlet, whose acoustic behaviour has been studied extensively both experimentally (NASA in static and flight configurations), and numerically to validate sound propagation models [9, 41, 42, 72]. It was designed so that, for normal operations, the acoustic modes generated by the rotor-stator interaction are cut-off and do not propagate out of the inlet. In experimental settings, a certain number of rods are added in the mouth to create a disturbance, whose interaction with the fan is designed to generate a cut-on azimuthal mode. This allows a precise control of the inlet acoustics.

As in Refs. [9] and [42], a simplified version of the axisymmetric bell-mouth inlet, used for static testing, will be modelled here. A schematic diagram of the approximate geometry, taken from Ref. [72], is shown in Fig. 5.3. The profile of the centerbody can be approximated by the polynomial:

$$r = 1.228(L - x) - 0.0575(L - x)^2 + 0.001025(L - x)^3 \tag{5.7}$$

where all quantities are expressed in cm.

The following problems could be solved with a 2D or 2.5D method, but the full geometry will be considered to demonstrate the feasibility of large 3D computations. Since HOP does not include a far-field integration method, it was not possible to perform a comparison with experimental results in this study. In the following sections, there will be a direct comparison, in the mid-field region, of HOP with both a high-order CAA and a low-order CFD code. Qualitative comparison with theoretical predictions of the propagation will also be made. This will allow further validation of the current code in realistic 3D situations, and give an evaluation of the gain obtained when using the current high-order approach.

The current boundary treatment can deal with the centerbody; however, it will first be omitted, as in Ref. [9], to simplify the problem and allow comparisons with analytical results. In that case, the source plane is placed 23cm from the inlet mouth, as indicated by the **D** line in Fig. 5.3. The resulting problem is

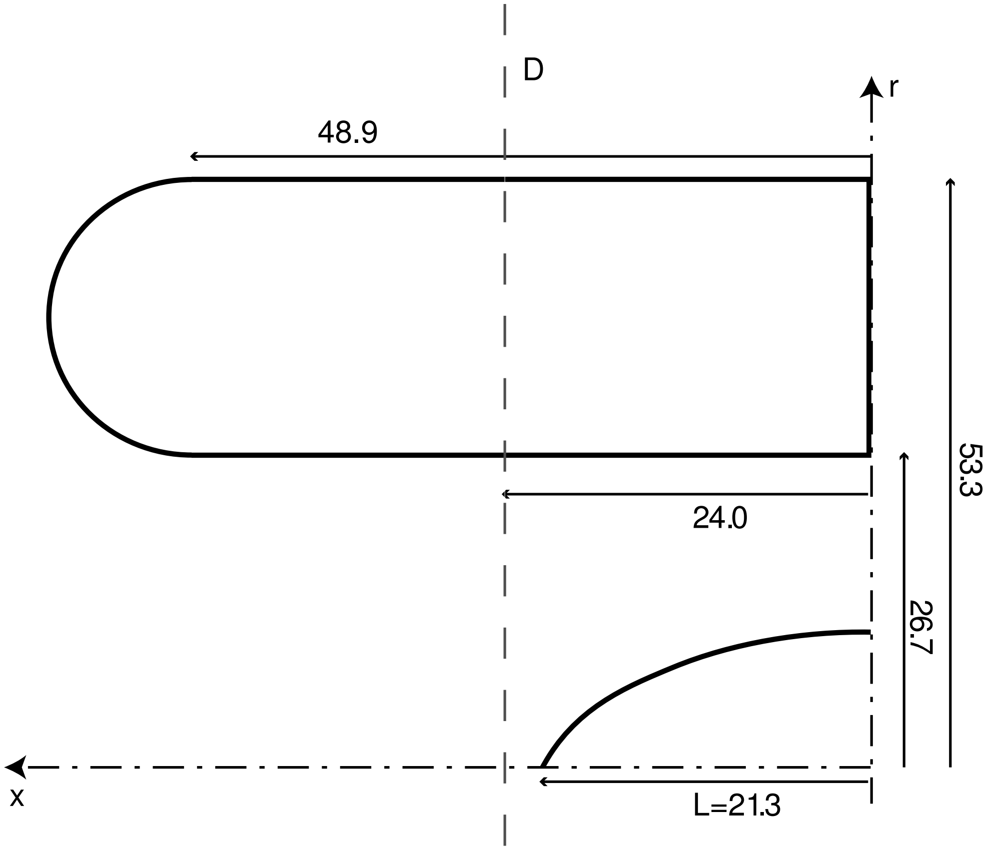

Figure 5.3: Simplified schematic of the geometry of the JT15D static inlet. Approximate measurements are in cm.

discretised with HOP using a uniform, regular Cartesian grid with $\Delta x = \Delta y = \Delta z = 0.012$m. It contains 111×111×116 points, including 15940 ghost points, 24 of which need to be evaluated with the 4-point normal extrapolation described in Section 3.3: this is 0.15% of all points, so it should not noticeably affect the accuracy. The incoming waves are imposed with an absorbing boundary condition because, as in Section 5.1.1, using the condition of Eq. (2.17) led to the generation of spurious waves. For similar reasons, and in all the following cases, the initial wave amplitude is smoothly increased from zero to its final value over $t = 25$.

5.2.2 Azimuthal modes

The propagation out of the inlet of several azimuthal, or "spinning", acoustic modes, as described by Eq. (5.2), is first computed, to study a type of 3D propagation found in typical fan noise problems (see Chapter 1). The nomenclature of Section 5.1.2 will be used throughout. The computation was made until a periodic regime is obtained, as is shown in Fig. 5.4. Several modes are studied, with different azimuthal orders, wavelengths and increasing cut-off ratios: Table 5.2. A frequency of 3150Hz ($\lambda = 10.6$ cm) is typical of the sound produced at normal engine operating conditions [41, 72], and the associated large Helmholtz number ($\tilde{\alpha} = \alpha a = 2\pi a/\lambda \simeq 16$) would represents a challenging computational problem for a low-order method. For atmospheric ambient conditions, it is represented by 8.84 points-per-wavelength with the HOP model.

Strongly cut-on modes

The main features of the radiation pattern can first be theoretically estimated. Lordi and Homicz [129] obtained an approximate analytical solution for the radiation to the far-field of acoustic modes from an infinitely thin cylinder of finite length. The full result is complex, but the authors show that, for well cut-on modes, most of the radiation is centered on a "principal lobe", whose direction is the same as the polar mode angle inside the duct[1]. If θ is the angle measured

---

[1] Non-planar modes are equivalent to a sum of several plane waves propagating at a certain angle, which depends on the wavenumber and the modal order [22, 48].

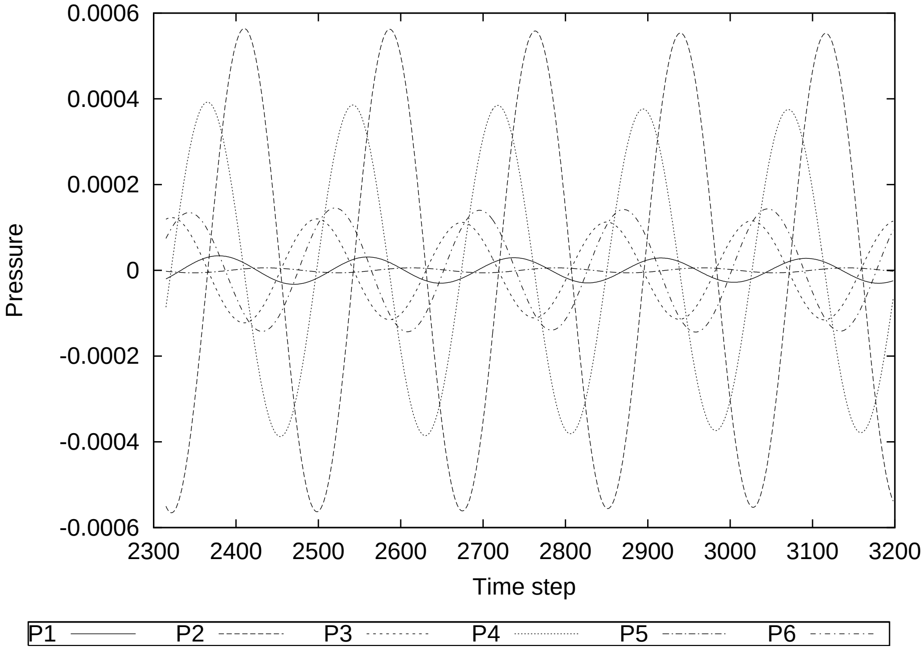

(a) Dimensionless acoustic pressure obtained by HOP in several points across the computational domain.

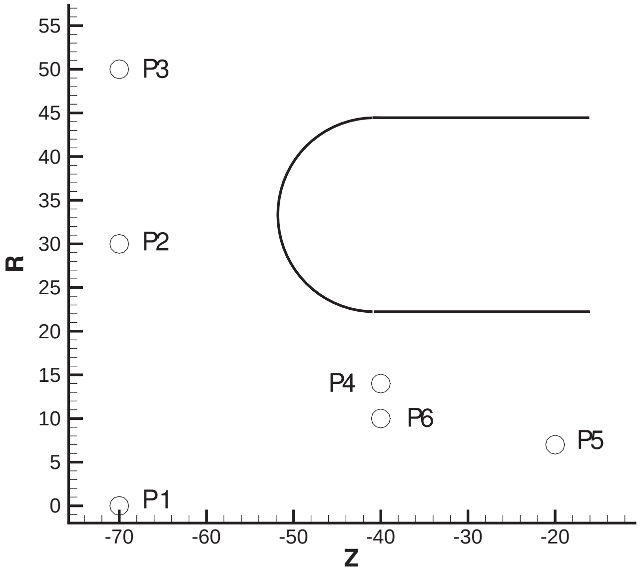

(b) Coordinates of the points in the HOP computational domain.

Figure 5.4: Convergence of the solution to a periodic state, for the (8,1) mode (3150 Hz).

from the inlet mouth, for no-flow cases this direction θ_p will be such as:

$$\alpha \cos\theta_p = \alpha_{x,m\mu} = \sqrt{\alpha^2 - \alpha_{m\mu}^2} \tag{5.8}$$

(using the nomenclature of Section 5.1.2). The resulting theoretical far-field directivity of the main lobes is shown in Table 5.2 for several modes of increasing cut-off ratio, along with the corresponding Helmholtz number $\tilde{\alpha}$. As the cut-off ratio (ξ in Eq. (5.4)) increases, the angle of radiation gets more important, the principal lobe moves away from the centerline.

Mode, λ (cm)	(4,1), 18	(8,1), 12	(8,1), 10.6	(13,1), 10.6
$\tilde{\alpha}$	9.3	14	15.8	15.8
PPW	15	10	8.8	8.8
θ_p (degrees)	35	44	38	71
Cut-off ratio ξ	0.57	0.69	0.61	0.95

Table 5.2: Modal parameters for the modes studied.

To validate the mid-field results, the propagation of several spinning modes with HOP was compared to results[2] obtained by ACTRAN, a commercially available linear CAA code [130]. It uses high-order finite and infinite elements, and assumes an irrotational flow. It has been thoroughly validated, for example by comparing the propagation of spinning modes from an unflanged, infinitely thin cylindrical duct with a benchmark analytical solution [55]. An axisymmetric model of the JT15D inlet was solved in the frequency domain with quadratic elements and 15^{th} order infinite elements at the boundary, to allow the waves to exit the domain with minimal reflections. All the modes in the following cases have a unit modal amplitude: $A_{nm\mu} = 1$ in Eq. (5.2).

The propagation of the (8,1) and (4,1) modes, at 3150 Hz ($\lambda = 10.6$ cm) and 1855.5 Hz ($\lambda = 18$ cm), is shown in Figs. 5.5 and 5.6 respectively. The results obtained with HOP (rotated for comparison) are shown next to the real part of the complex pressure obtained by the frequency-domain ACTRAN method. It appears that, in the HOP computation, the acoustic mode is artificially dissipated

---

[2] Provided by Naoki Tsuchiya from the Institute of Sound and Vibration, University of Southampton, U.K.

as it propagates along the wall. However, apart from the presence of a low level of pressure along the centerline in both HOP results, in both cases the solution behaves similarly after it is diffracted by the inlet mouth, with good agreement in the directivity pattern.

These observations are now confirmed by examining the radiation patterns for both methods in more detail, for the first three modes of Table 5.2. A good measure of the directivity of the modal radiation is given by the amplitude of the complex pressure obtained by ACTRAN, which can be compared to the root-mean-square (*RMS*) of the pressure signal in HOP, computed in the last period of oscillation (see Fig. 5.4(a)). These quantities, taken along an arc of radius 60 cm centered on the inlet mouth at z=48.9 cm, are plotted in Fig. 5.7. The RMS values from the HOP computation were scaled by $\sqrt{2}$ to match the pressure amplitudes given by ACTRAN. The modes appear highly dissipated after propagation. This dissipation is more important as the cut-off ratio and the modal angle increase. There is also a spurious amount of radiation along the centerline ($\theta < 15$ degrees), representing an artificial scattering into other radial modes. The match in *directivity*, however, is very good for the main lobe, where most of the acoustic energy is present. These results are also consistent with the theoretical directivity trend of Table 5.2.

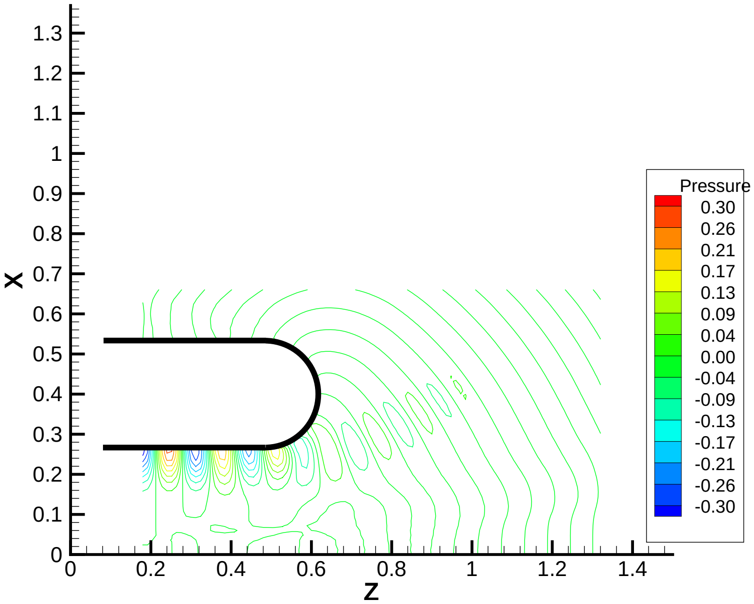

(a) HOP scheme, acoustic pressure.

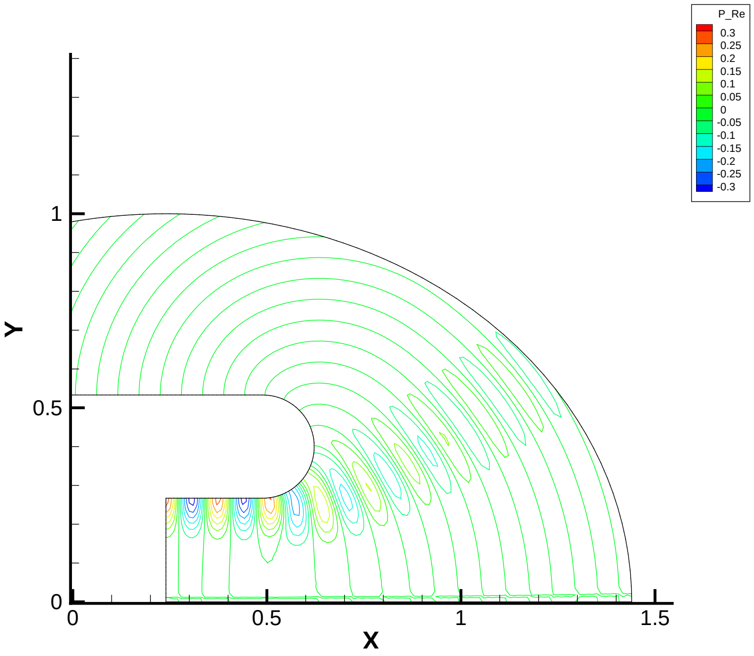

(b) ACTRAN, real part of the complex pressure.

Figure 5.5: Pressure contours (unit modal amplitude) in a symmetry plan for the (8,1) mode at 3150Hz.

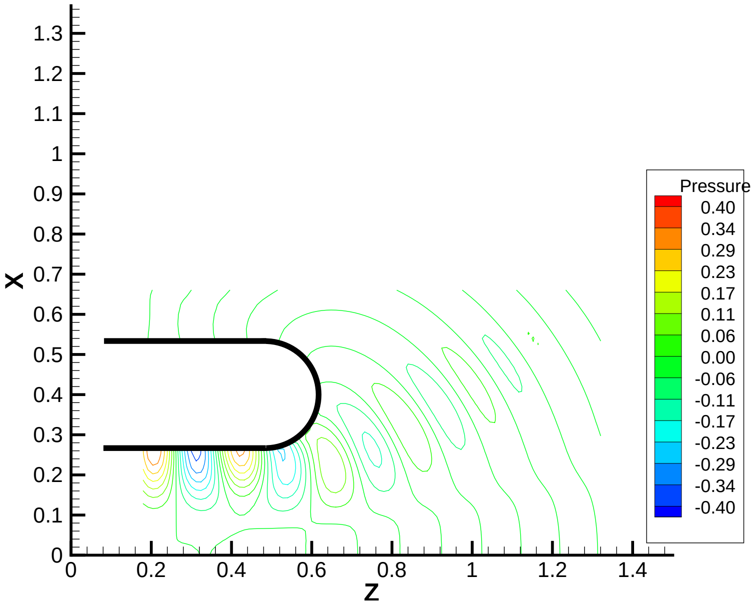

(a) HOP scheme, acoustic pressure.

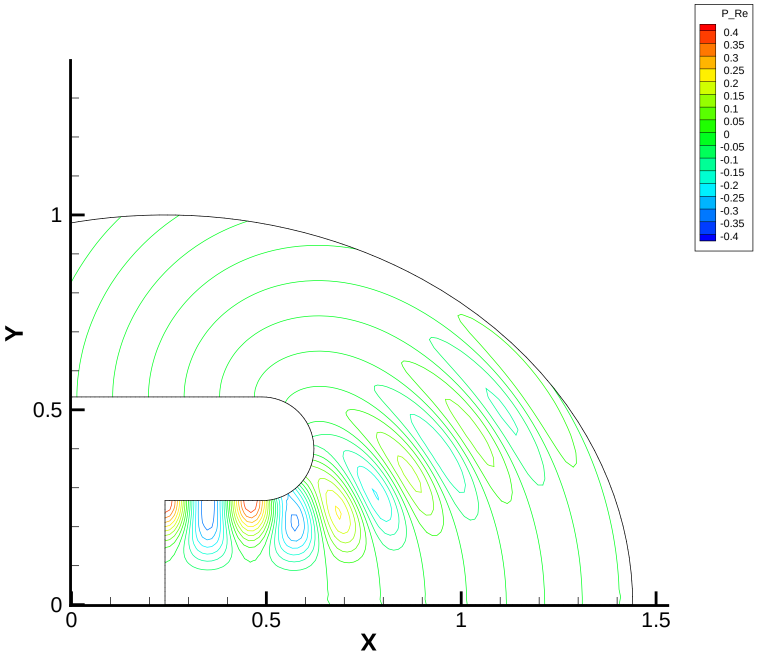

(b) ACTRAN, real part of the complex pressure.

Figure 5.6: Pressure contours (unit modal amplitude) in a symmetry plan for the (4,1) mode at 1855.55Hz.

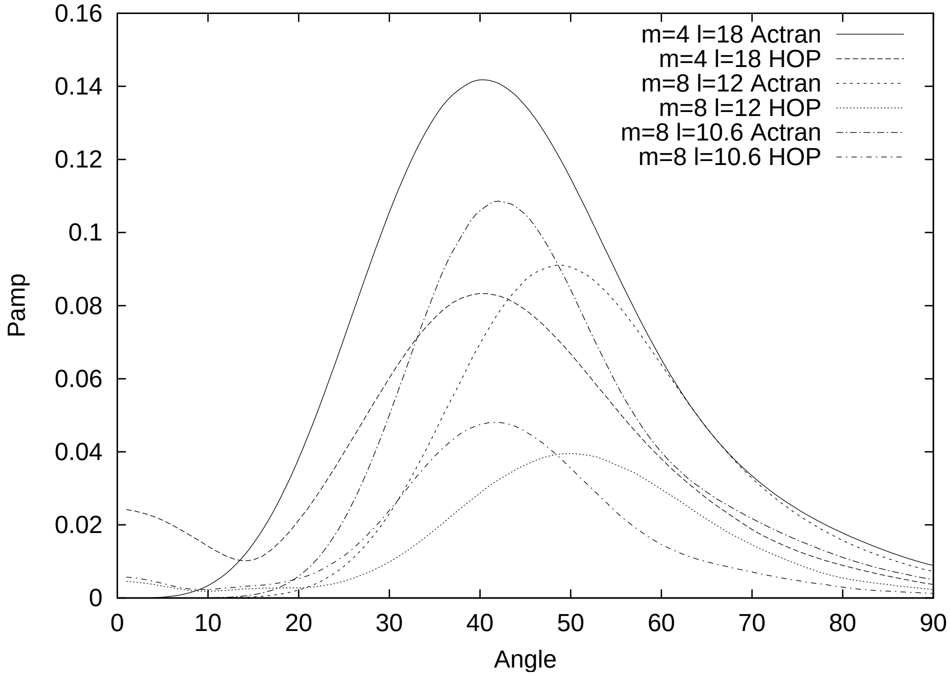

Figure 5.7: Directivity plot for the (8,1) mode with $\lambda = 10.6$ cm and 12 cm, and the (4,1) mode with $\lambda = 18$ cm.

Mode near cut-off and flow effects

A mode closer to cut-off will now be considered. In some experimental studies of the JT15D inlet, 41 rods were placed upstream of the fan to force the generation of the (13,1) propagating mode [72]. For a typical BPF of 3150Hz, this mode is very close to cut-off ($\xi = 0.95$). In this case, the analysis of Lordi and Homicz [129] indicates that the main radiation lobe will be larger, and situated far away from the centerline (*cf.* Table 5.2).

This nearly cut-off mode was computed with HOP, and this solution is compared to the ACTRAN result in Fig. 5.8. The resulting directivity, scaled in the same manner as the results of Fig. 5.7, is shown in Fig. 5.9 (no flow results). Compared to the previous results, the dissipation occurring during the propagation along the wall is more pronounced, probably because the mode is so close to cut-off. This also means that the spurious centerline radiation becomes relatively more important. However, the resulting directivity is mainly well estimated, with the main lobe centered on the same very large polar angle.

A steady flow is now added in both computations. For the inlet case considered, a flow at rest in the far-field and with a Mach number of 0.18 at the fan-face is also typical of static engine operating conditions [42]. This steady flow is computed with the AU3D code, and the result is non-dimensionalised and interpolated on the HOP grid: Fig. 5.10. This mean flow is used in the HOP computation, as in Section 4.3.2. The same is done with ACTRAN, the steady flow being computed by a finite-element, irrotational compressible flow solver (with an identical result). The effect this has on the propagation is shown in Fig. 5.11: the wavelength is shortened inside the duct, where the velocity is important, but the diffracted wave past the bellmouth lip is essentially unchanged, and this is reflected by the absence of significant change in the directivity (Fig. 5.9).

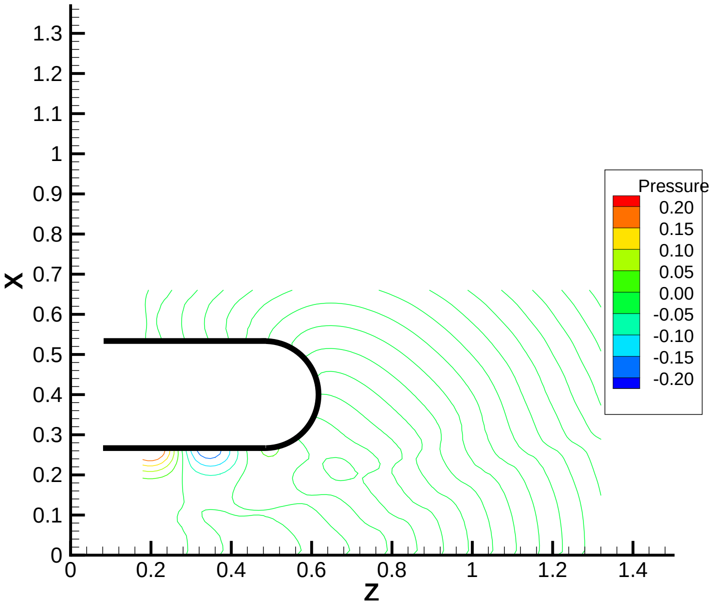

(a) HOP scheme.

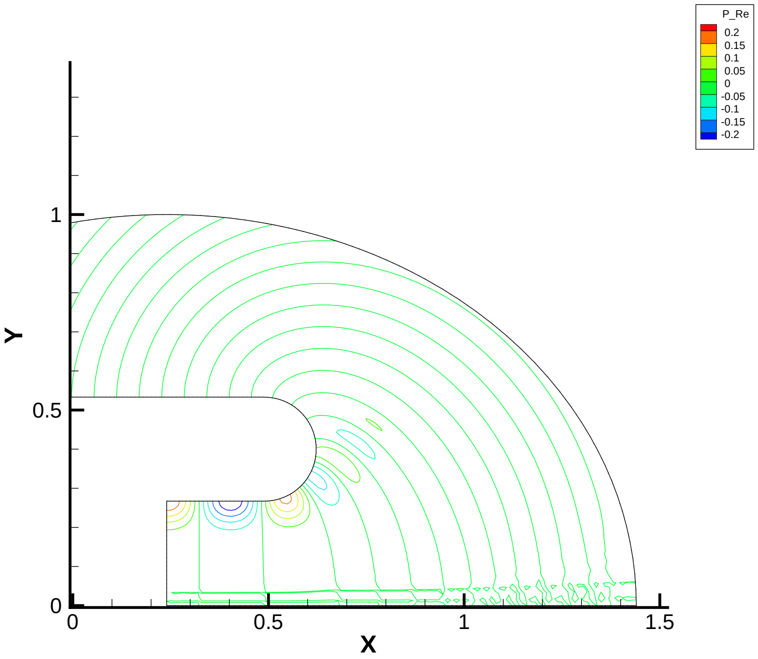

(b) ACTRAN.

Figure 5.8: Pressure contours in a symmetry plan for the (13,1) mode at 3150Hz (unit modal amplitude).

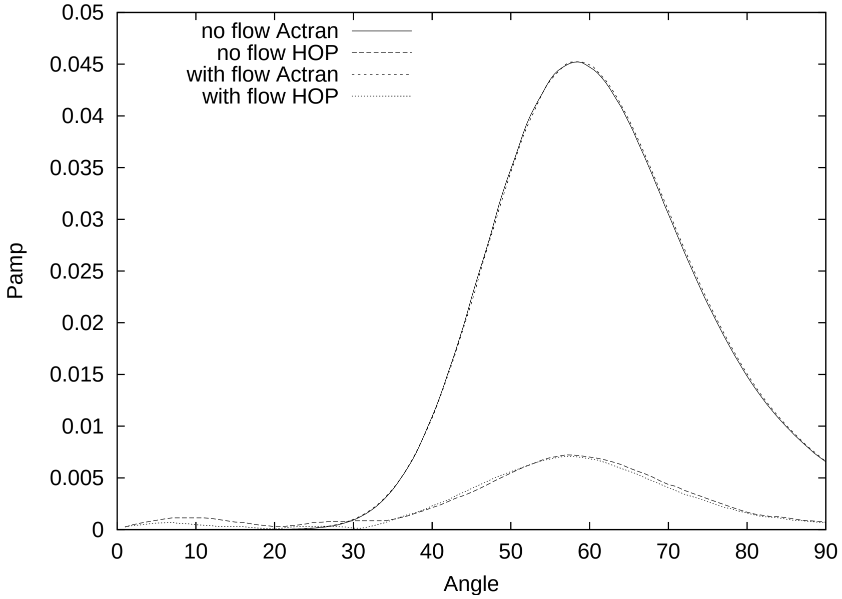

Figure 5.9: Directivity plot for the (13,1) mode at 3150Hz, with and without mean flow (M=0.18), HOP and ACTRAN computations.

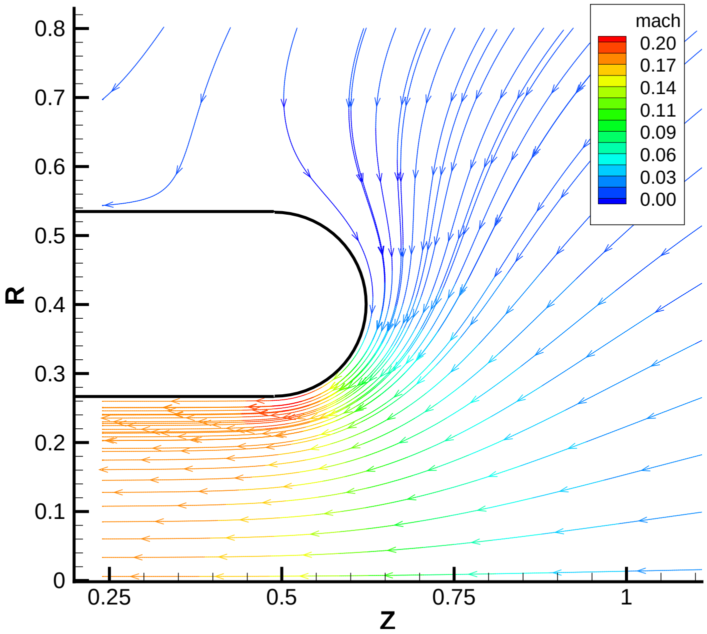

Figure 5.10: Computed mean flow with M=0.18 at the fan-face, streamlines color-coded with the Mach number values.

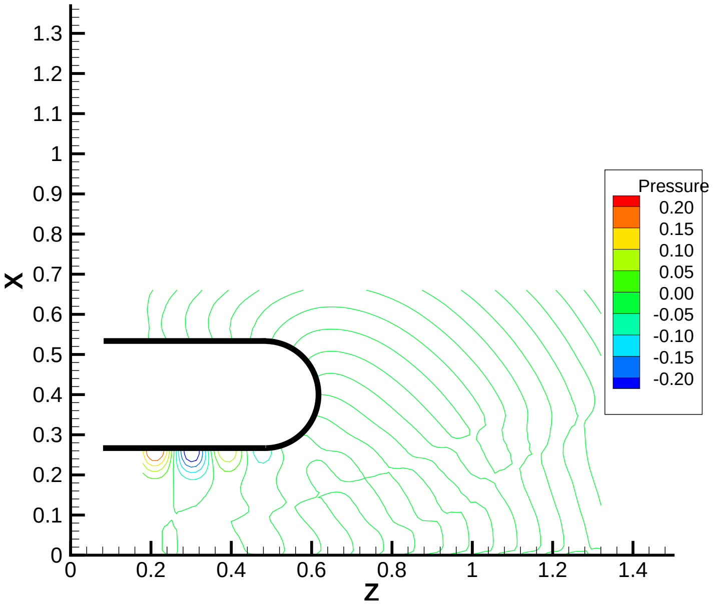

(a) HOP scheme.

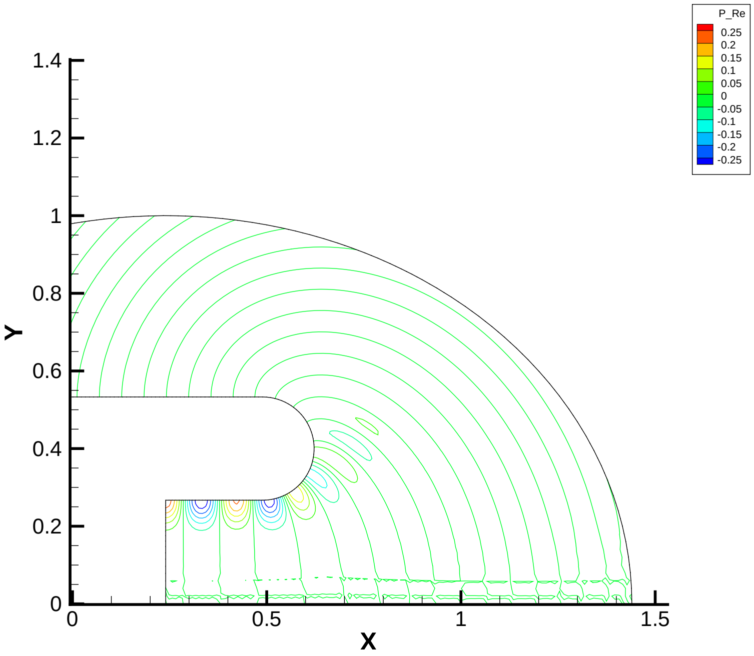

(b) ACTRAN.

Figure 5.11: Pressure contours in a symmetry plan for the (13,1) mode at 3150Hz (unit modal amplitude), with the steady flow of Fig. 5.10.

Full JT15D geometry

An example of a computation run with the full geometry, including the fan spinner, will now be presented. The 110×110×95 grid contains 26337 ghost points. For such a large geometry, the pre-processing phase, including the inversion of the sparse matrix, took 3 hours on the 2.4GHz PC used throughout this study. A 10-point long absorbtion zone inside the duct is imposing the annular modes described by Eq. (5.5). The propagation of the (8,1) mode at 3150 Hz, as in Fig. 5.5(a), is computed. The result is displayed in Fig. 5.12. Qualitatively, the result is very similar to the no-centerbody one (Fig. 5.5(a)), because most of the acoustic energy is situated close to the wall (above the “caustic radius” [22]) and is unaffected by the spinner; the main radiation lobe is similar. There is more dissipation however, because of the long propagation across the wall, and more acoustic pressure close to the centerline, which is probably due both to the varying annular radius, and to additional spurious scattering. This result qualitatively illustrates the capabilities of the systematic 3D wall algorithm in handling complex geometries.

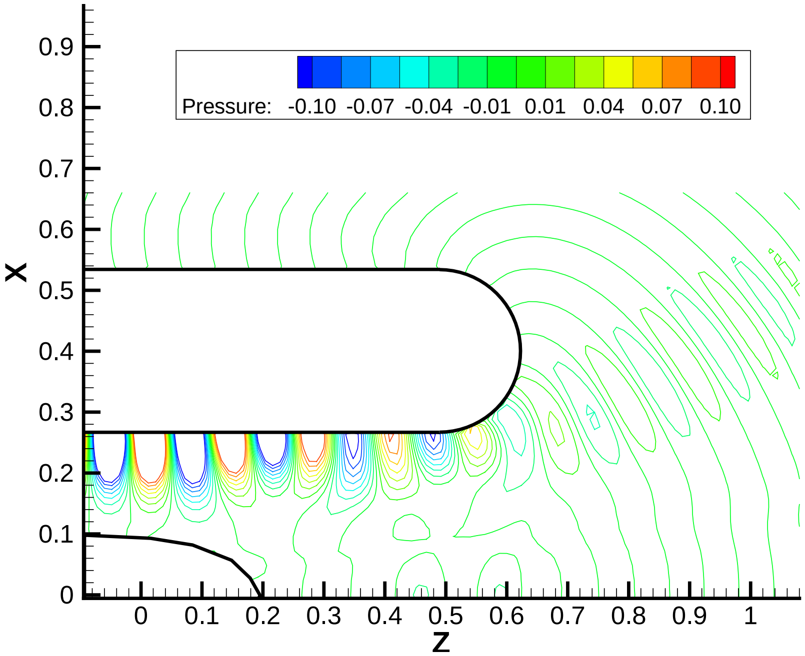

Figure 5.12: Solution for the (8,1) mode at 3150 Hz, full geometry.

5.2.3 Plane wave cases

The computation of plane wave modes ($m = 0$), in the mid-field region of the JT15D geometry used in Section 5.2.2, will now be compared to similar computations made using AU3D, for several frequencies, and using an increasingly fine meshing. This code was used with success in similar problems for low-frequencies cases [17, 18]. The waves are imposed through a 1D non-reflecting characteristic boundary condition, but the investigation of 1D ($m = 0$) modes should limit the errors introduced by the boundary condition.

A 30 degrees angular sector of the simplified axisymmetric inlet is meshed, with most of the details being captured inside the inlet with an almost constant mesh size Δ, as shown in Fig. 5.13. Elsewhere, the grid is increasingly stretched to prevent artificial reflections. The grid shown in Fig. 5.13 is coarsely meshed, with Δ=1.0 cm. Similar meshes were made with: $\Delta = 1.5$ cm, $\Delta = 0.5$ cm and a very fine grid with $\Delta = 0.2$ cm. As in Section 5.1.1, 150 time steps per period will be used, with 3 Newton iterations.

The computation was first done for a high-frequency case (BPF of 3150 Hz, $\lambda = 10.6$cm), with a negligible mean flow, for 16 wave periods. Fig. 5.14 shows the contours of acoustic pressure in an equivalent plane of symmetry for the HOP solution (Δx=0.012 which means 8.84 PPW) and the equivalent AU3D one with $\Delta = 0.2$ cm (53 PPW). Here, and in the following cases, the HOP length-scales were appropriately dimensionalised, and the results scaled to match the initial amplitude of the AU3D non-dimensional acoustic pressure. The values of the computed solutions along the centerline are shown in Fig. 5.15, with the full range of AU3D resolutions.

As previously, the convergence of the spatial discretisation towards a consistent solution, and the strong numerical dissipation and dispersion that arise when a coarse mesh is used, are clearly shown. For 7 PPW, the wave is very quickly damped and becomes half a wavelength out of phase. Even when it is not strongly dissipated (21 and 11 PPW), an increasing phase difference with the 53 PPW solution appears clearly along the propagation; this is again a confirmation that this type of error is dominant in low-order codes (Lockard [63]). There is, overall, only a good match between the HOP solution and the 53 PPW

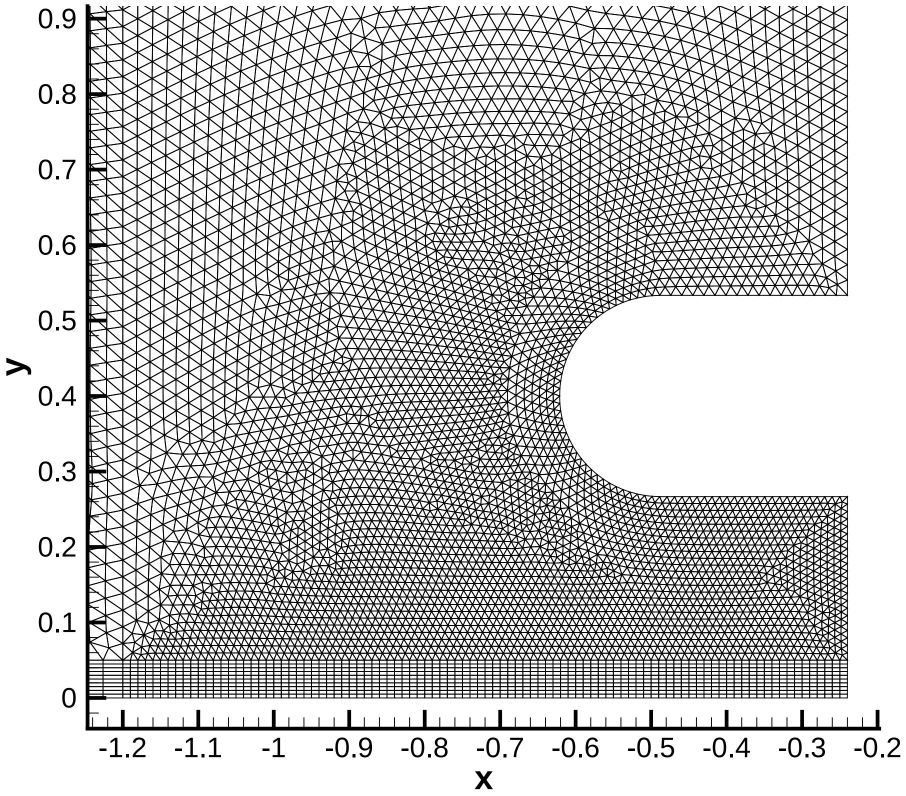

Figure 5.13: 2D-section of the grid used in the low-order sound propagation calculation, $y = 0$ plane. Coarsely meshed case with Δ=1.0 cm.

solution, as can be seen in Fig. 5.14. Some slight asymmetrical discrepancies, visible in Fig. 5.15, indicate the presence of a low-frequency spurious component. From $x = -0.7$, there is increasing dispersion appearing, because the grid is progressively stretched.

The computation shown on Fig. 5.14(b) took 7 hours 15 minutes on a desktop 2.4GHz PC. The AU3D computation for the 21 PPW case took around 10 hours[3] on the same machine, and because the running time scales linearly with the number of points, this is equivalent to 120 hours for the full 3D geometry, nearly 17 times more than with the HOP code. The 53 PPW case was run on a different machine, therefore the running time cannot be directly compared, but it is estimated to be twice as large as for 21 PPW. The 7 PPW case took around 1 hour, which means 12 hours for the full 3D geometry; this is slightly more than the equivalent HOP calculation, even though the computational stencil is larger. This is because HOP is a simpler linear code, dedicated to acoustic computations. These results are summarised in Table 5.3.

Method	Running time	Ratio
HOP	$\sim$ 7h	1.0
AU3D, $\Delta = 1.5$ cm	12h	1.6
AU3D, $\Delta = 0.5$ cm	120h	16.5
AU3D, $\Delta = 0.2$ cm (estimate)	240h	33.0

Table 5.3: Computational times for the fully 3D JT15D plane wave cases.

---

[3] The running time is reduced by around 10% to avoid taking into account the extra, stretched grid zone which is necessary to avoid reflections and instability in AU3D runs.

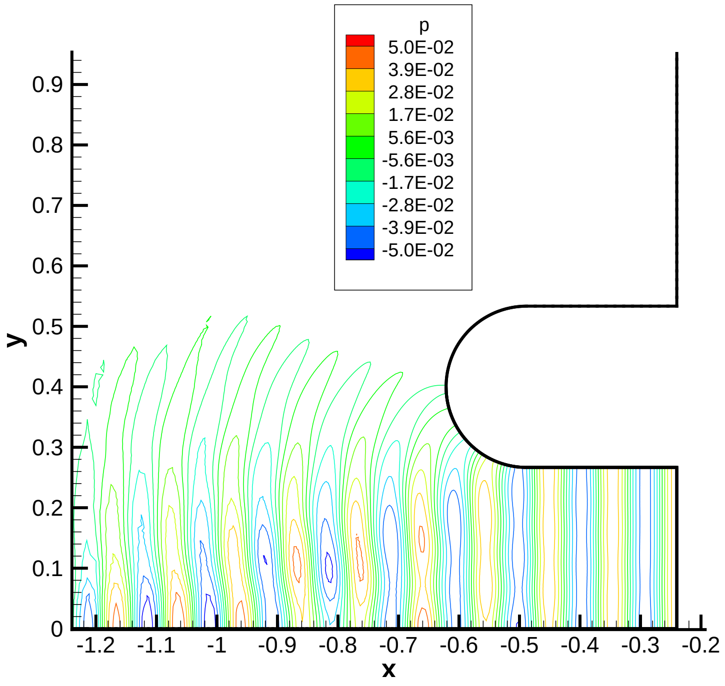

(a) AU3D result with $\Delta = 0.2$cm, 53 PPW.

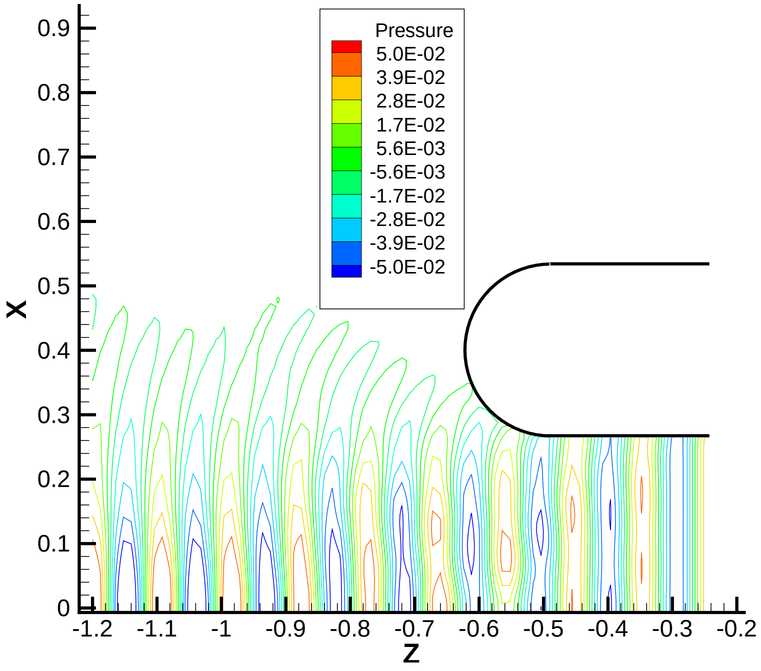

(b) HOP result (scaled) with $\Delta x = 1.2$ cm, 8.84 PPW.

Figure 5.14: Propagation of the (0,0) mode with $\lambda = 10.6$ cm. Contours of non-dimensional acoustic pressure in a symmetry plane.

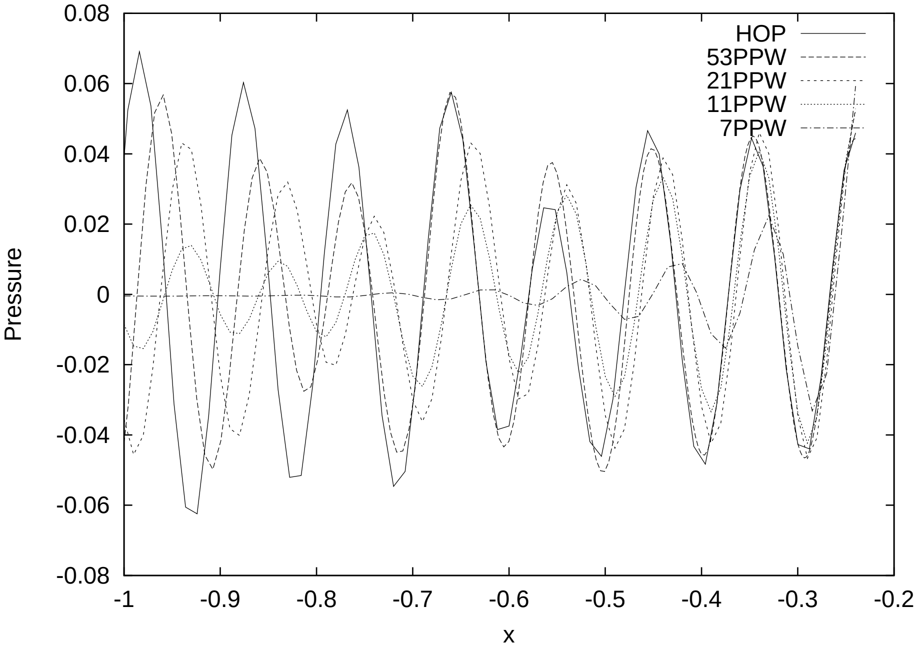

Figure 5.15: Propagation of the (0,0) mode with $\lambda = 10.6$ cm. Acoustic pressure along centerline for HOP with 8.84 PPW, and AU3D with several resolutions.

The same computations are also made for $\lambda = 13.2$cm, which represents a frequency of approximately 2532Hz, to study the evolution of the convergence of both solutions (now $\tilde{\alpha} \simeq 13$). Results are displayed in Fig. 5.16: the AU3D solution with a 66 PPW resolution, and 11 PPW for HOP. The pressure along the centerline is shown in Fig. 5.18. Similar observations as for the $\lambda = 10.6$ cm case can be made.

The computation was finally done for a low-frequency case, $\lambda = 30$ cm or $\nu \simeq 1113.3$ Hz (now $\tilde{\alpha} \simeq 5.6$), for 8 wave periods. Fig. 5.17 shows the pressure contours in the symmetry plane. The match between the HOP computation with 25 PPW and the first three AU3D cases, as shown in Fig. 5.19, is not as good as above, although the low-order solution seems to converge as the resolution is increased from 20 and 30 PPW to 60.

The ratios of the running times for the last two cases are similar to those presented in Table 5.3. Taking all these results together, it is clear that, as the PPW resolution of the AU3D computations is increased, there is convergence towards a single solution, with the dissipation and the dispersion errors being reduced, in that order. As in the previous HOP computations, some dissipation appears close to the wall, but there is an overall good match of both solutions, and the diffraction seems to be correctly represented. Examining the solution along the centerline, this match seems to degrade as the wavelength is increased, with a slowly varying amplitude discrepancy appearing. Overall, this is not a very serious problem, as the high-order HOP method is not as advantageous for low-frequency problems. But it was not the case in Section 5.1.1, when no wall was present, and the validation results of Section 4.3.1 showed that the errors of the new wall boundary condition tended to disappear as $\tilde{\alpha}$ decreased. It could come from the AU3D boundary conditions, which are not designed for acoustic computations, or from the limited size of the HOP domain which leads to artificial reflections, particularly since the radiation depicted in Fig. 5.17 is very different from a monopole source. The absorbing condition used to impose the incoming acoustic solution could also be a source of low-wavelength error.

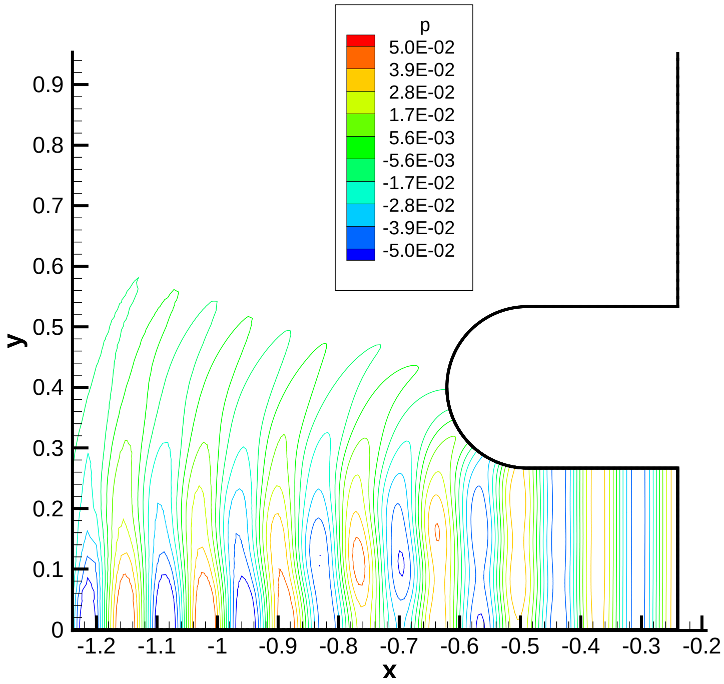

(a) AU3D result with $\Delta = 0.2$ cm, 66 PPW.

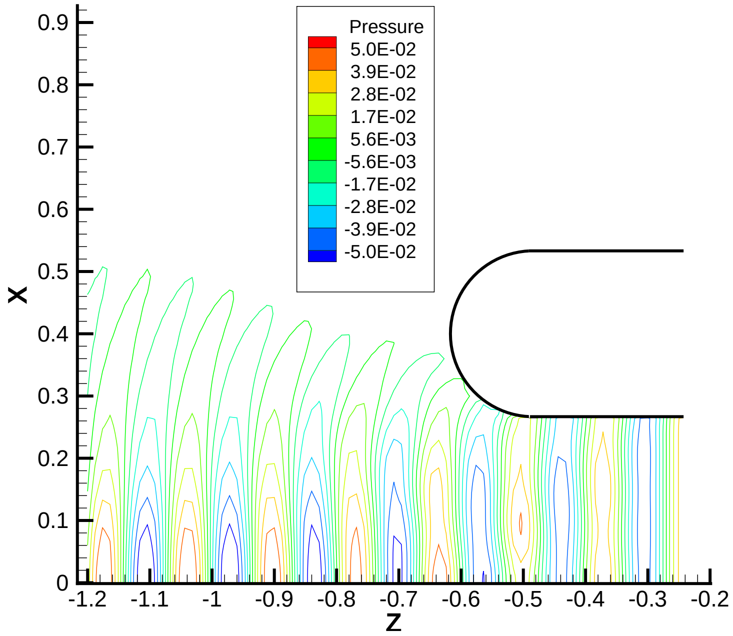

(b) HOP result (dimensionalised) with $\Delta x = 1.2$ cm., 8.84 PPW

Figure 5.16: Propagation of the (0,0) mode with $\lambda = 13.2$ cm, contours of non-dimensional acoustic pressure.

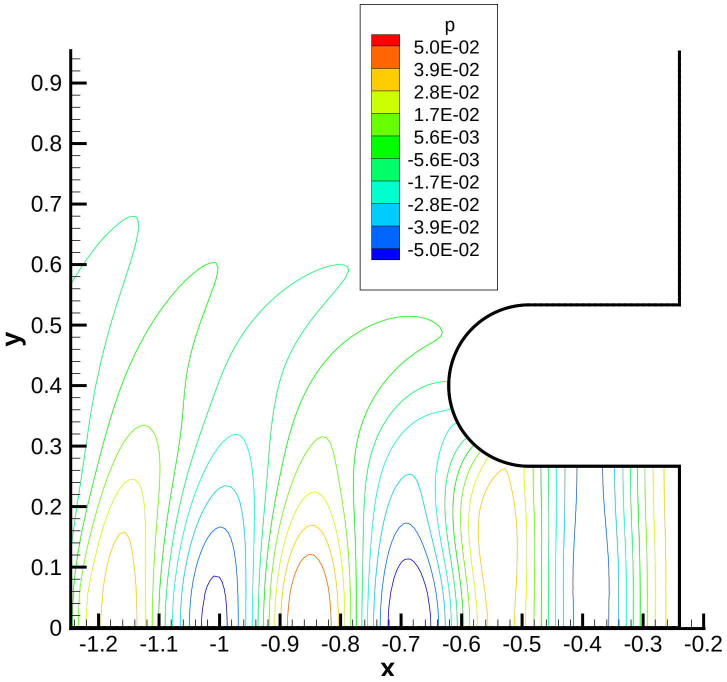

(a) AU3D result with $\Delta = 0.5$ cm, 60 PPW.

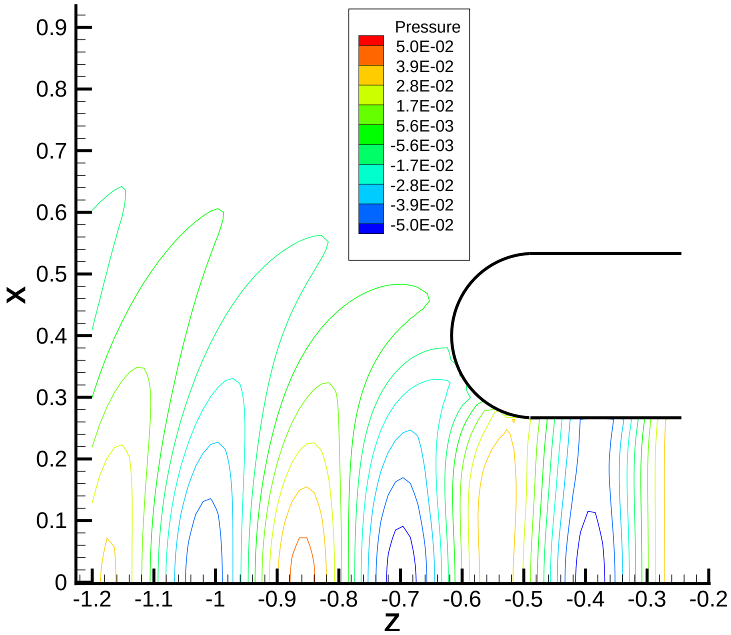

(b) HOP result (dimensionalised) with $\Delta x = 1.2$ cm, 8.84 PPW.

Figure 5.17: Propagation of the (0,0) mode with $\lambda = 30$cm, contours of non-dimensional acoustic pressure.

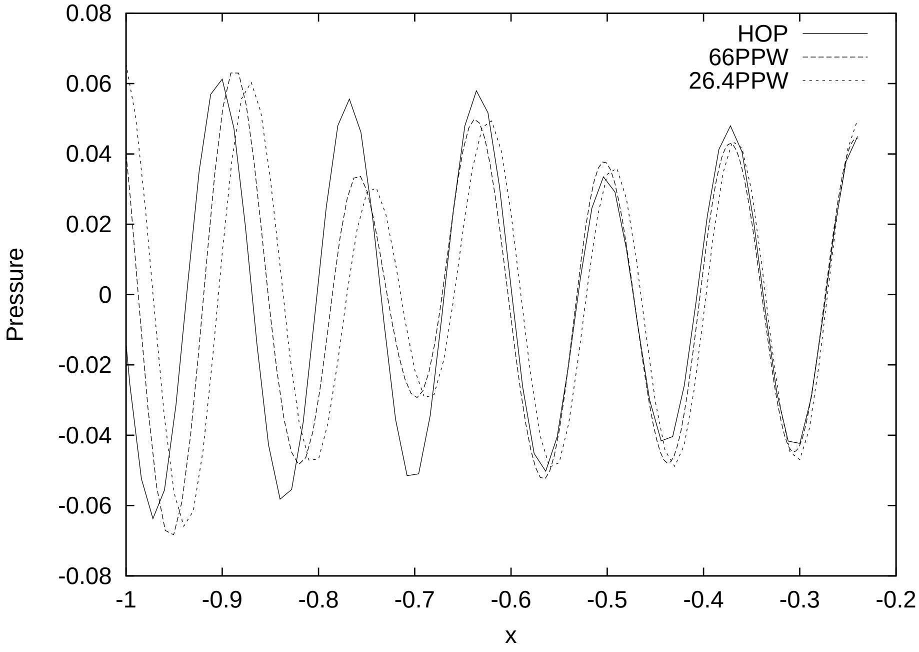

Figure 5.18: Same as Fig. 5.15, with $\lambda = 13.2$ cm.

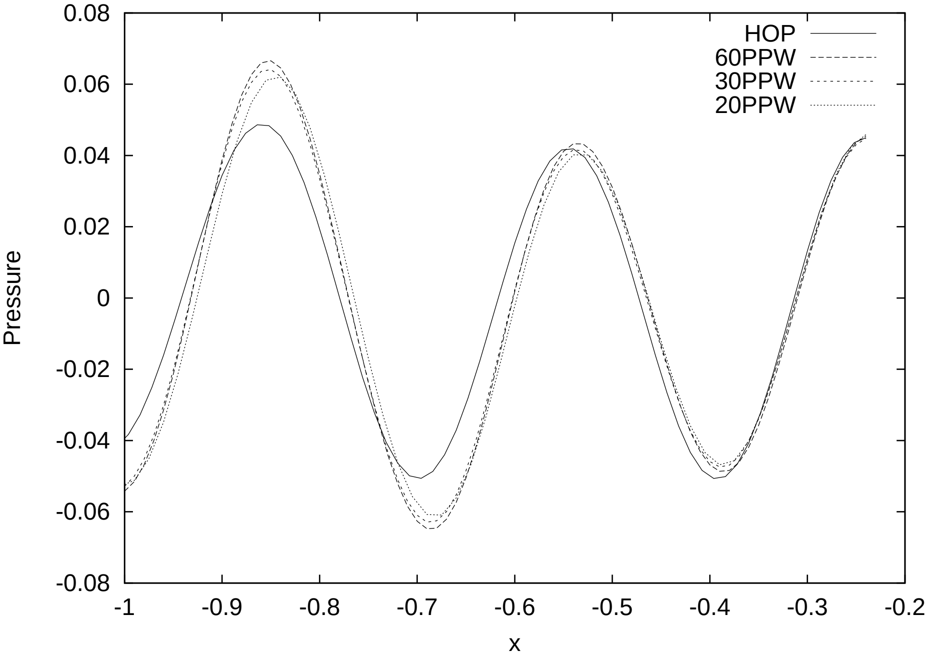

Figure 5.19: Same as Fig. 5.15, with $\lambda = 30$ cm.

Different configurations were investigated in this case to study boundary effects: Fig. 5.20. The previous computation is shown together with several other cases, the first has a domain extended to $z = -117$, the second has the absorbing boundary condition added to all borders, and the third uses the 1D in-duct boundary condition of Eq. (2.17) instead of the absorbing one used above. No significant change to the solution is observed, so a boundary problem is unlikely. The error probably comes from the spurious centerline radiation which was observed in previous modal results.

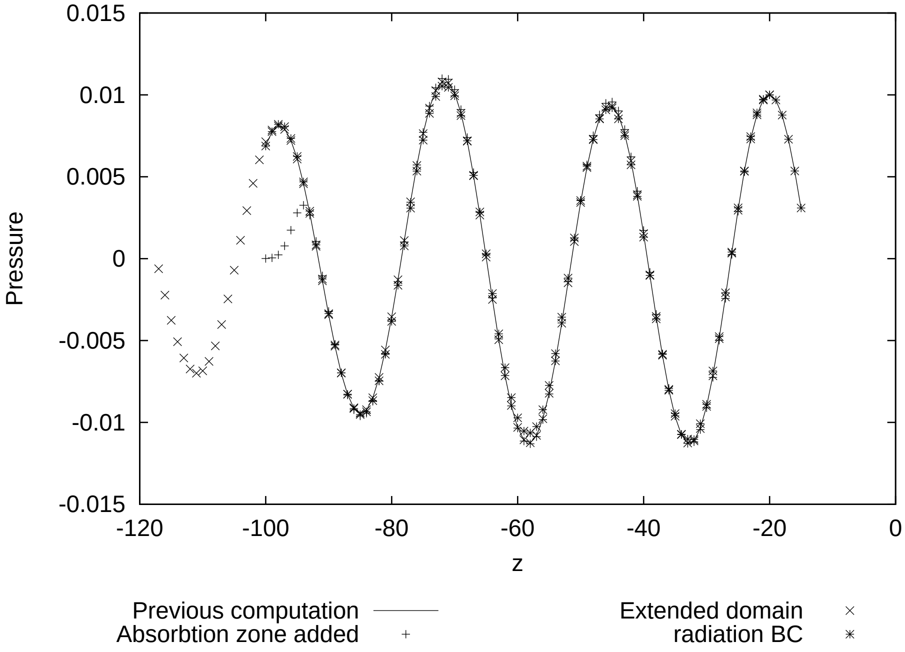

Figure 5.20: (0,0) mode with $\lambda = 30$ cm: boundary conditions investigations.

Discussion

It appears that the HOP scheme correctly predicts the directivity of propagating azimuthal modes, both by comparing results to the theoretical far-field trend (Table 5.2), and by direct comparison to ACTRAN results. But the spinning modes lose some of their amplitude as they propagate along the wall. The amount of dissipation depends on the modal angle and thus on the amount of modal reflections on the wall. This defect is related to the validation results of Section 4.3.1: for important Helmholtz numbers, the wave is dissipated as it travels along the wall boundary, more than it is dispersed (its phase is more accurate): see Fig. 4.21(b) for example.

This probably comes from the extrapolation inaccuracies, exacerbated by the fact that three are performed in 3D. The selective artificial dissipation, necessary to maintain stability, could possibly also be a factor, but it is little different to the 2D case. However, together with Section 5.1.1, these results effectively show that, if a low-order discretisation is employed, it is necessary to use at least 30 PPW to propagate an acoustic wave over 10 wavelengths, even for a low target accuracy. Using such resolutions with acoustic problems of large Helmholtz numbers (more than 10) leads to impractical situations in the mid-field region, with large computational and memory costs. With the HOP code, gains of one order of magnitude in the computational time are obtained (see Table 5.3), for equivalent solutions. This ratio of around 20 to 30 times is also slightly underestimated because of the grid-stretching employed from $x = -0.7$, and could become even larger if higher accuracy or a larger propagation distance are needed.

One of the defects appearing in the HOP solutions is the excessive radiation appearing along the centerline, between 0 and 20 degrees, after the mode is diffracted by the inlet mouth. It does not disappear as the wavelength is increased, and represents, in a sense, a scattering of the incoming mode into higher radial orders, probably caused by the dissipation occurring along the wall. The low-order normal extrapolation, used on a few points which are situated around the bellmouth inlet lip, could also be at the origin of this defect, but it is only used for a limited amount of ghost points.

5.3 Second case study: elliptic inlet models

Most early studies of inlet propagation with a high-order scheme were performed on idealised, infinitely thin cylindrical inlets, for example Dong and Mankbadi [80] or Li *et al.* [96]. They are simple to implement, and allow the inclusion of a simple uniform convective mean flow as an approximation of real flows. This captures most of the diffraction effects at the lip, but not the details of the geometry or the complex effects of real inhomogeneous flow. The next step, made possible by the current boundary method, is to study simple inlets with a finite thickness. An elliptic profile can be used to model both thin and bell-mouth inlets, depending on the parameters used, and this has been used by some researchers as a good case study for the propagation and radiation of spinning modes, as Keith points out in Ref. [22]. It also leads to a simple model of an asymmetric inlet: the scarfed inlet. First, some preliminary tests on an axisymmetric geometry are made, using comparisons with AU3D, as for the JT15D geometry in Section 5.2.3.

5.3.1 Axisymmetric inlet

The parameters of the profile to be used are shown in Fig. 5.21. The surface is described by the following equation:

$$\left(\frac{z}{K}\right)^2 + (\sqrt{x^2+y^2} - R)^2 = T^2 \tag{5.9}$$

An inlet shape with parameters $T^2 = 0.51$, $R = 3$, K=4 (dimensionless quantities) is modelled with $\Delta x = 0.1$. The grid is composed of 97×97×100 points, and contains 13468 ghost points. An extrapolation along the normal direction is needed for 56 of those (0.4%). The pre-processing phase in this case took 1 hour 20 minutes on the 2.4GHz PC. The small curvature present at the tip of the ellipse was handled well by the wall algorithm. A 10-point wide absorbing zone, which introduces the input wave, was included, as in the JT15D cases.

The propagation of the $m = 0$ waves with the HOP model above will be compared to AU3D results, for different frequencies ($\lambda = 1$ and 2, $\tilde{\alpha} = 18.8$ and 9.4). A 30 degree sector is meshed, using several resolutions to verify the convergence towards a consistent solution. Around the inlet, a uniform grid

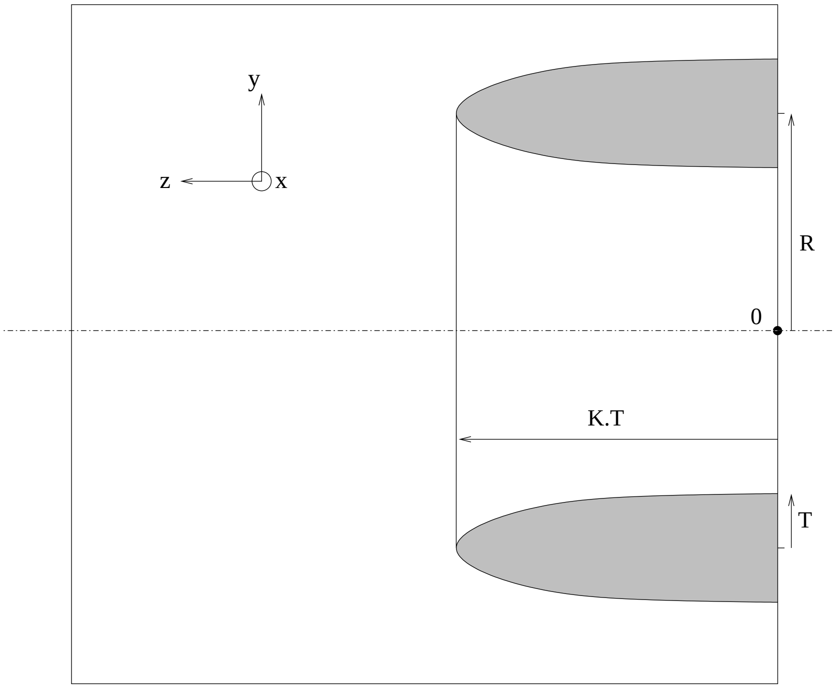

Figure 5.21: Description of the elliptic inlet geometry.

resolution of Δ is used, and the grid is stretched elsewhere. $\Delta = 0.1$, $\Delta = 0.05$ and $\Delta = 0.033$ will be used, to obtain respectively 10, 20 and 30 PPW for the first case and 20, 40, 60 in the second. The low resolution grid is shown in Fig. 5.22.

<u>$\lambda = 1$</u>

The $\lambda = 1$ case is first computed, using the same time step parameters as in Section 5.2.3, and running the computation for 16 wave periods. The results for the HOP and the high-resolution AU3D computations are shown in Fig. 5.23, and the pressure was scaled in the same way as for Section 5.2.3. Some amount of artificial distortion appears in the HOP result because of aliasing from the low resolution and contour plot artifacts near the elliptic boundary.

The match in most of the domain is good, even if an increasing phase difference appears as the wave propagates. Examining the results along the centerline, in Fig. 5.24, confirms this. It appears that the 10 PPW solution is strongly numerically dissipated, and that increasing the grid resolution reduces this effect.

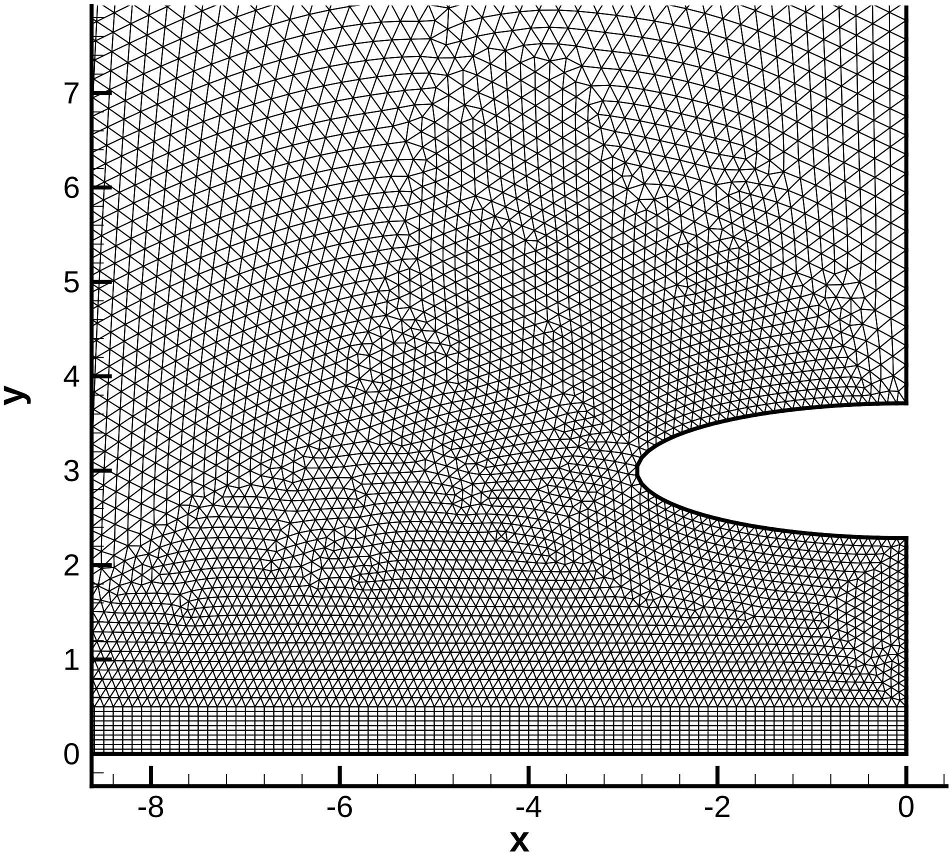

Figure 5.22: 2D-section of the grid used in the low-order sound propagation calculation. Coarsely meshed case with Δ=0.1.

However, even the 30 PPW solution becomes out of phase with the HOP solution. Dissipation also appears close to the wall. These trends are consistent with the JT15D results above, showing that more than 30 PPW lead to an approximately correct solution, although some discrepancies still exist. The 3D computational times and gains obtained by using the high-order method are shown in Table 5.4. They were scaled as in Section 5.2.3, and the gains obtained are similar but slightly higher, because the current grid is not as strongly stretched as for the JT15D case (Fig. 5.13).

Method	Running time (hours)	Ratio
HOP, $\Delta x = 0.1$	9	1
AU3D, $\Delta = 0.1$	31	3.5
AU3D, $\Delta = 0.05$	106	12
AU3D, $\Delta = 0.033$ (estimate)	164	19

Table 5.4: Computational times for the plane wave computations with the 3D elliptic inlet.

$\lambda = 2$

For the $\lambda = 2$ case, the results can be seen in Fig. 5.25 and Fig. 5.26. The match in amplitude along the centerline is not as good as above, even though both solutions are close in phase, and the AU3D solutions seems to converge as the resolution increases up to 60 PPW. Similar observations as for the JT15D cases of Section 5.2.3 are made: the match along the centerline is not as good for the low-frequency case, with an apparent amplitude discrepancy. The overall quality of the HOP results is satisfactory (Fig. 5.26), except close to the wall where once more the waves are dissipated.

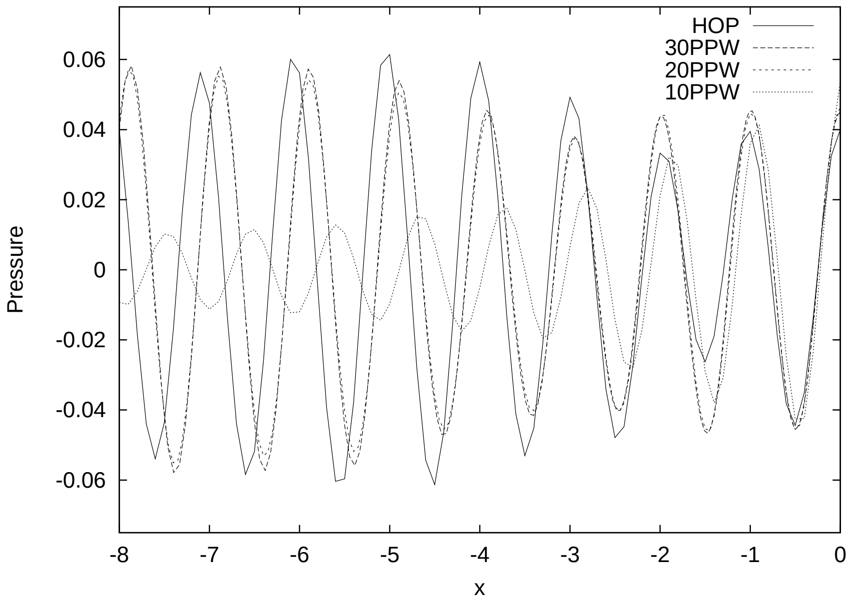

Figure 5.23: (0,0) mode with $\lambda = 1$, acoustic pressure along centerline for the HOP solution (10 PPW) and AU3D solutions.

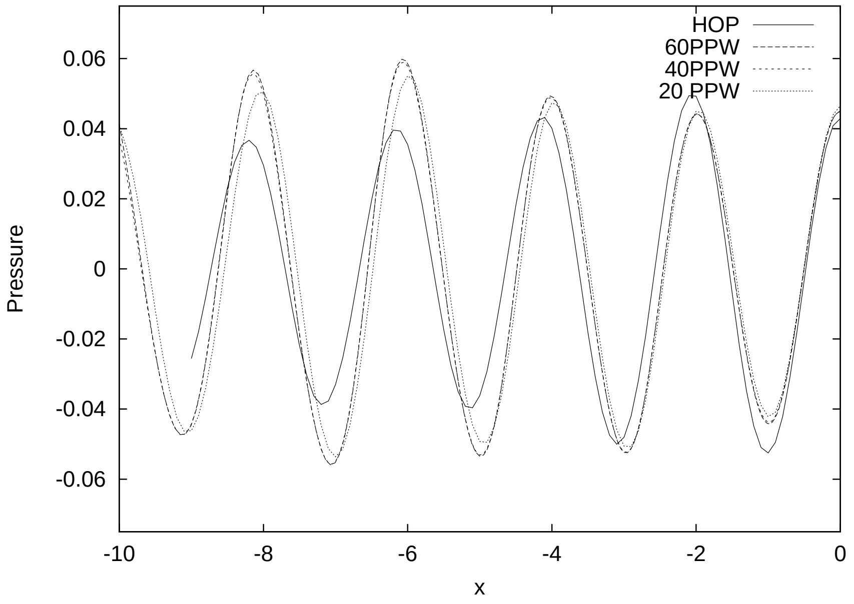

Figure 5.24: Same as Fig. 5.24 with $\lambda = 2$.

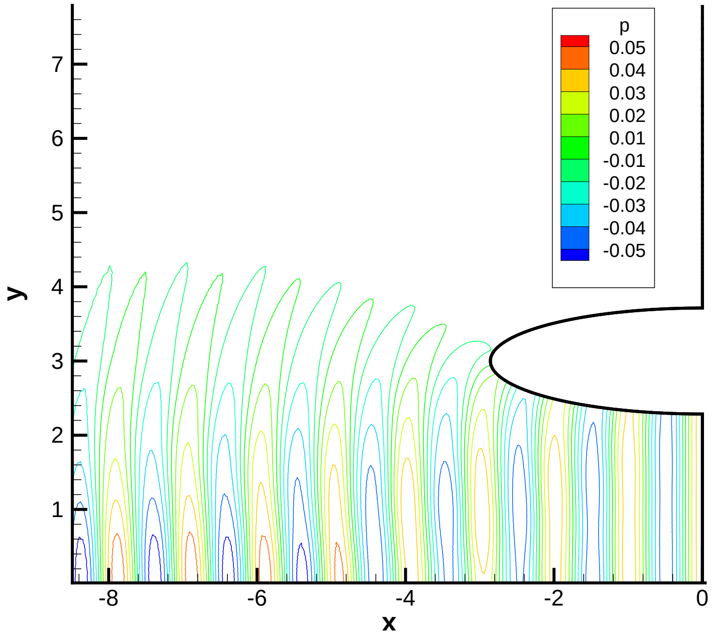

(a) AU3D result with $\Delta = 0.033$, 30 PPW.

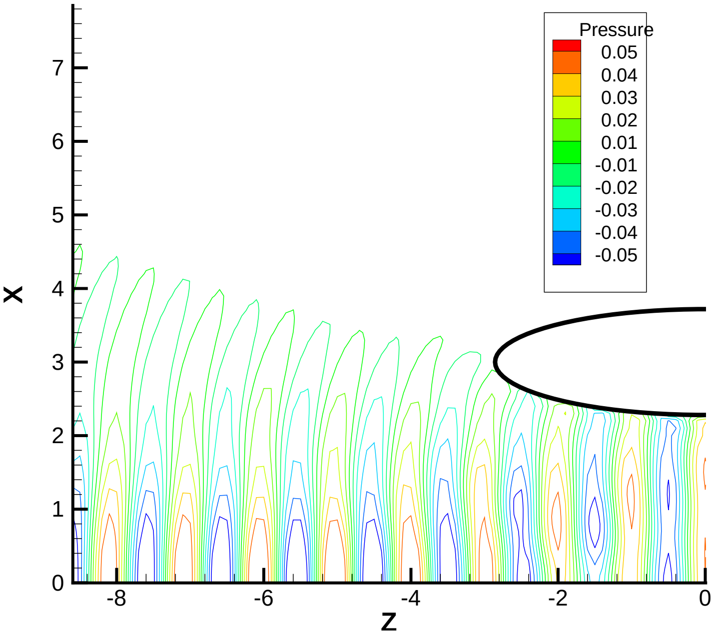

(b) HOP result with $\Delta x = 0.1$, 10 PPW.

Figure 5.25: Propagation of the (0,0) mode with $\lambda = 1$. Contours of non-dimensional acoustic pressure in a symmetry plane, scaled for comparison.

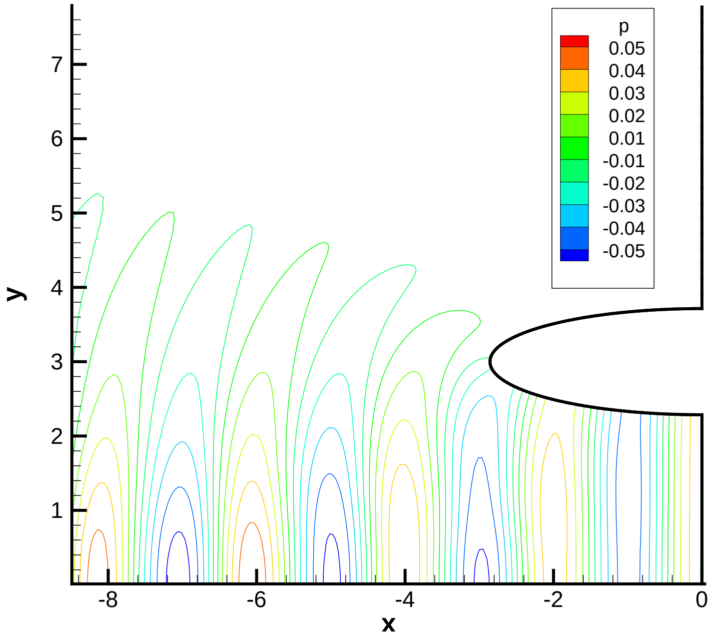

(a) AU3D result with $\Delta = 0.05$, 40 PPW.

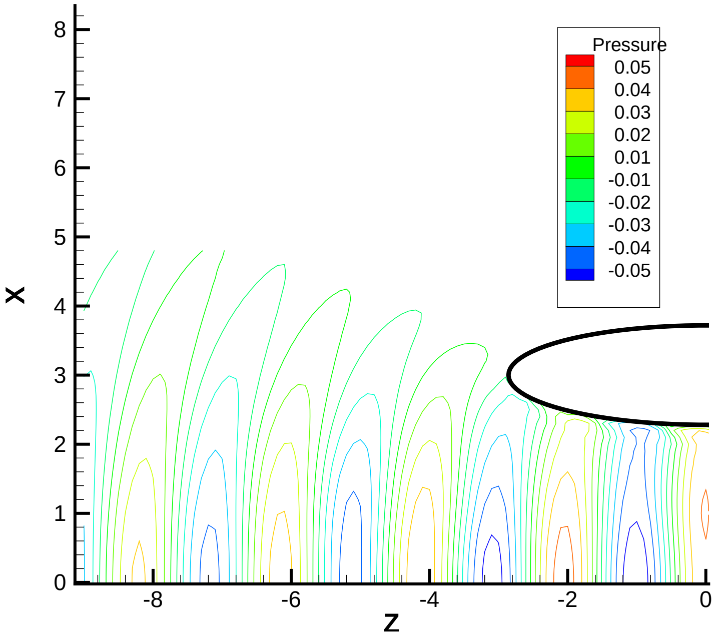

(b) HOP result (dimensionalised) with $\Delta x = 0.1$, 20 PPW.

Figure 5.26: Propagation of the (0,0) mode with $\lambda = 2$. Contours of unsteady pressure (arbitrary amplitude) in a symmetry plane.

5.3.2 Scarfed inlet

The elliptic inlet above was then modified to represent a scarfed inlet. Traditionally, this means that the inlet has a longer upper lip, for aerodynamic reasons. But, as was pointed out in Chapter 1, negatively scarfed ones are being investigated for their acoustic performance, as they can reflect some of the acoustic energy away from the ground direction, as represented in Fig. 5.27. This is a simple but representative example of an asymmetric geometry: in this case, a full 3D model is needed. A similar study was made by Keith [22] using ray theory, for one high frequency mode ($\tilde{\alpha} = 40$), using some approximations, as it was very mathematically intensive. A more complete study was also made in Ref. [22] for an infinitely thin scarfed cylinder, which showed that the inverse scarf caused a reduction in the peak amplitude radiated downwards (main lobe), but that this effect was only small for well cut-on modes.

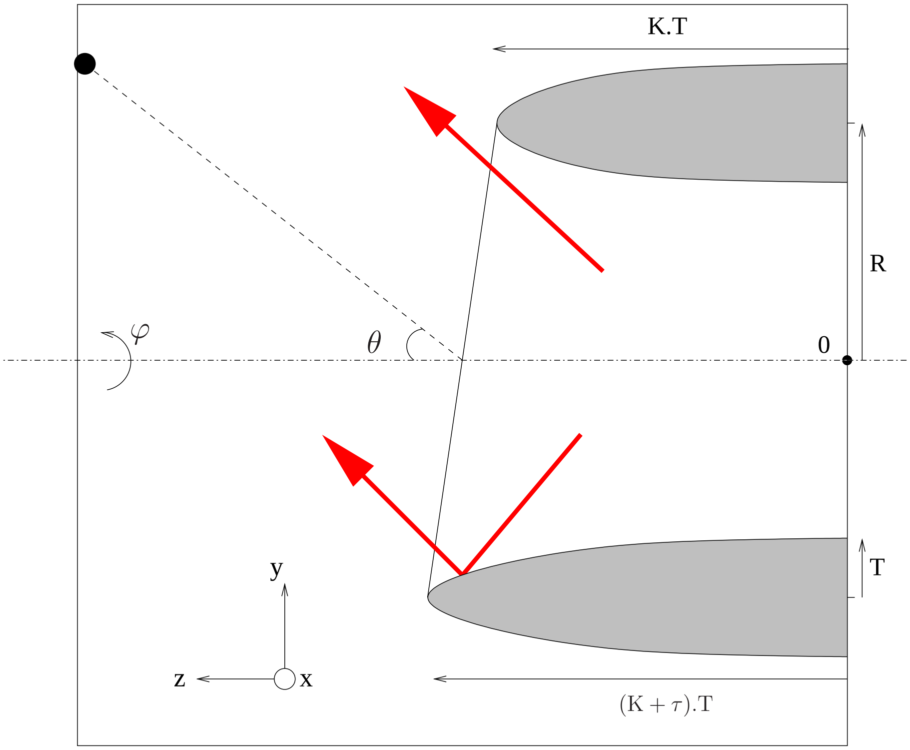

Figure 5.27: Description of the negatively scarfed inlet model, and its effect on radiated sound.

The HOP scheme is very interesting for this problem. 30 PPW would be required with a low-order scheme: this would represent a grid of more than 2 million points, around 1.7Gb of memory and a run-time of several hundred hours, because the full annulus would need to be included. As explained in Chapter 2, compact or quadrature-based methods also become very costly in 3D, as they require solving large linear systems. Özyörük used a finite difference method which could handle 3D inlets, using cylindrical coordinates, but did not investigate asymmetrical geometries [9]. A good-quality body-fitted grid, structured or unstructured, would be difficult to generate in this case, particularly for high scarfing ratios. The Cartesian grid used here, containing the immersed boundary, remains smooth and uniform in most of the domain.

The geometry is modelled by modifying the elliptic profile of Eq. (5.9), as shown in Fig. 5.27. The radius is still $R = 3$, and $T^2 = 51$, but this time the surface equation is modified by a scarfing ratio $0 < \tau \leq 1$:

$$\left(\frac{z}{K + \tau \sin(\varphi)}\right)^2 + (\sqrt{x^2 + y^2} - R)^2 = T^2 \tag{5.10}$$

if φ is the azimuthal angle around the z axis. The particular geometry studied uses $\tau = 0.4$. The grid is identical to that of the axi-symmetric case above, but contains 13470 ghost points, 44 of which need extrapolation along the normal. The wall algorithm used in HOP has no difficulty in handling this asymmetrical geometry, shown in Fig. 5.28.

The effect of the scarfing on several acoustic modes will be investigated. First, a plane wave mode is used as input, with $\lambda = 0.9$ (9 PPW, $\tilde{\alpha} \simeq 21$). The computation is run until a periodic regime is obtained. The mid-field SPL directivity obtained along the domain's boundary is shown in Fig. 5.29 as a function of the polar angle θ (*cf.* Fig. 5.27). Most of the energy radiates in the center, so the scarfed lip does not have a strong effect on the directivity of most of the sound, which is in any case not radiated towards the ground. A small difference for the secondary diffraction lobes is however noticeable.

The behaviour of spinning modes is more important, because, as was seen in Section 5.2.2, most of the acoustic energy is directed away from the centerline direction. The SPL obtained is shown in Fig. 5.30, for several different modes

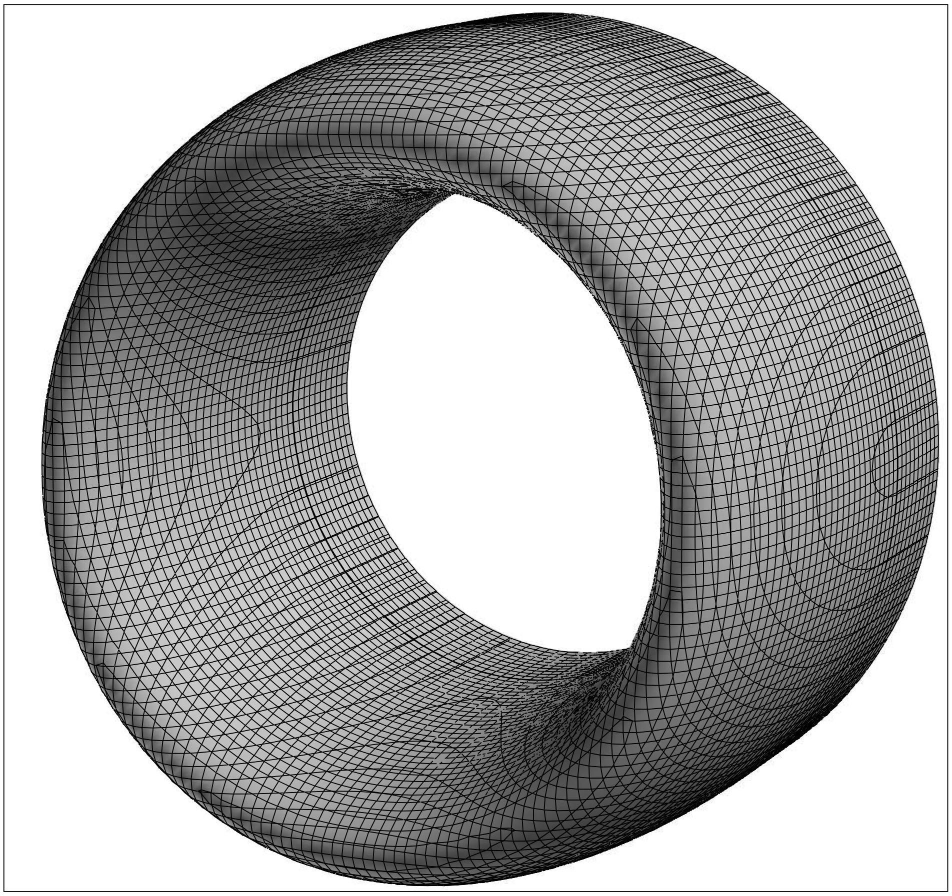

Figure 5.28: 3D scarfed elliptic inlet surface, overlayed with the intersections with the Cartesian grid.

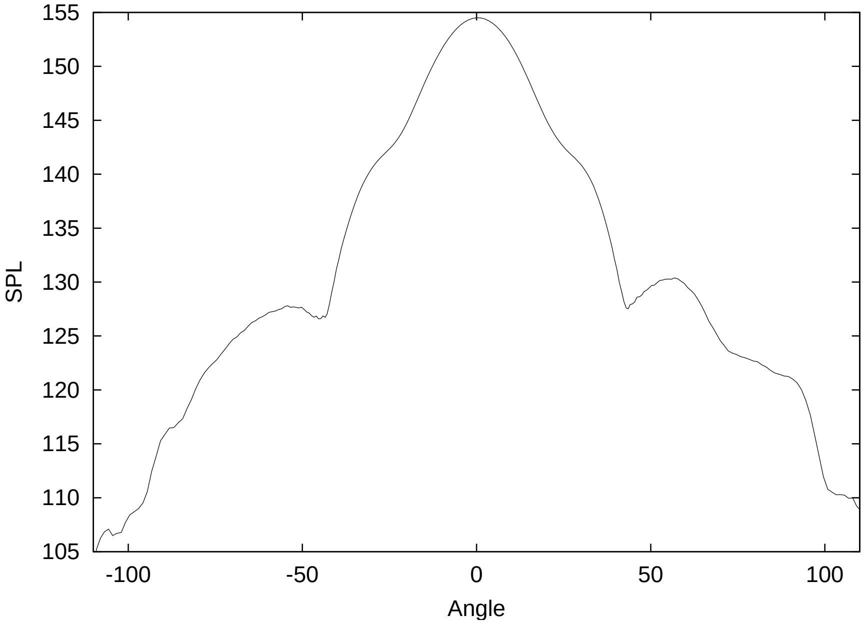

Figure 5.29: Mid-field SPL plot for the plane wave mode with $\lambda = 9$, angle=θ.

with different cut-off ratios (table 5.5). As in the JT15D cases above, the modes become more dissipated as ξ and the modal angle increase. It can be seen that the scarfed lip causes a relative reduction of between 0.5 and 2 dB in the peak SPL radiated downwards, and the overall reduction is higher for modes that radiate with a large angle. The trend exhibited here is consistent with the results of Ref. [22], and with intuition: the modes that radiate most strongly away from the centerline are most affected by the extended inlet lip (see Fig. 5.27). A far-field integration would be necessary to determine the amount of silencing obtained on the ground level. This result is interesting because it is the modes radiating from an engine inlet with a large downwards angle that will tend to cause a lot of noise on the ground level.

Mode	(4,1) $\lambda = 0.9$	(4,1) $\lambda = 2.0$	(8,1) $\lambda = 1.1$	(13,1) $\lambda = 0.9$
PPW	9	20	11	9
ξ	0.33	0.74	0.74	0.94

Table 5.5: Theoretical cut-off ratios ξ for the modes considered.

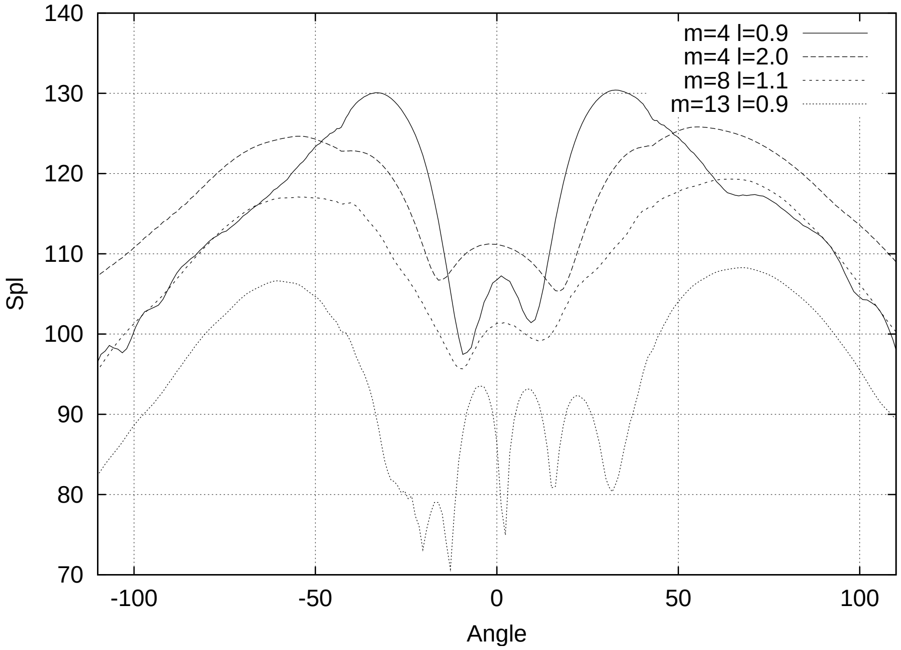

Figure 5.30: Mid-field SPL plot for the modes of Table 5.5.

5.4 Concluding remarks

The first case studied in this chapter, a simple wave propagation problem with no wall surfaces, confirmed classic CAA results by demonstrating the efficiency of the high-order DRP scheme. The new wall boundary condition was then added to HOP, and both the JT15D and the elliptic inlet geometries were modelled. Although no direct comparison with far-field results could be made, mid-field HOP computations were related to equivalent ones obtained with other schemes. Similarly to the validation results of Chapter 4, comparisons with an extensively benchmarked 2D CAA program, ACTRAN, showed that important dissipation, caused by the extra extrapolations used in the 3D method, occurred as the sound propagated. Probably because of this, a small quantity of spurious waves was also found radiating at low angles, close to the centerline. However, the directivity patterns obtained with HOP were consistent with reference and theoretical results.

Comparisons made for plane wave cases, in both geometries, with solutions obtained with the low-order AU3D method, showed that the dissipation occurred close to the wall boundary, and was more important as the modal angle increased. Centerline discrepancies appeared for large wavelengths, because of the spurious radiation described above. A good overall match was obtained, but low-order computations were found to need at least 30 PPW, which leads to an increase in computational time of more than 15 times compared to 8 PPW HOP computations. The memory cost of solving a fully 3D problem with such a fine grid would probably be a crucial limiting factor.

Potential instability leads to the use of reduced time steps, as shown in Chapter 4, but this is also the case for traditional methods using body-fitted grids. Even if the full resolution of 7 PPW, found in free-field problems, cannot be used, the permitted resolutions are effective and still largely more efficient than with a low-order code. For comparison, the non-optimised high-order scheme of Özyörük was used with resolutions of 12 PPW [36]. However, the important dissipation associated with the immersed boundary condition in 3D preclude its immediate use in its present state of development.

The acoustic shielding effect of a negatively scarfed inlet for certain acoustic modes was investigated using a simple but fully 3D model. The new 3D wall boundary condition developed in chapter 3 handled the asymmetric geometry while keeping a high-quality, uniform Cartesian grid in most of the domain. Reductions of around 2 dB in the mid-field SPL were observed for spinning modes that radiate strongly towards the ground direction. This case illustrates how complex, multi-dimensional effects could be investigated with the current approach. To use a low-order or implicit method would be extremely costly for similar problems, unless a 2.5D model with substantial simplifying assumptions is used.

Overall, the duct cases presented in this chapter suggest that the wall boundary developed in this work exhibits some important dissipation which is dependant on the modal angle, and thus on the number of internal modal reflections occurring. As currently implemented, the scheme's accuracy is insufficient for direct application to industrial problems.

Chapter 6

Conclusions and further work

6.1 Conclusions

In the current work:

- A fully 3D sound propagation code ("HOP") was developed. It uses a finite difference discretisation to solve the time domain, non-conservative LEE equations. Both spatial and temporal schemes are optimised for wavenumber accuracy.
- This scheme was chosen after a review of existing computational aero-acoustics schemes. These generally high-order accurate schemes were developed because of the inefficiency of traditional, low-order accurate CFD methods when used for acoustics.
- A novel 3D wall boundary condition was developed, using a structured immersed boundary approach, to enforce the slip boundary condition while keeping a regular Cartesian grid in the whole of the computational domain. It can model disconnected and concave surfaces, with no sharp edges. Few, if any, existing immersed boundary method have been developed in conjunction with a high-order scheme. The associated algorithm was described in detail, and the discretisation errors were estimated.
- The effects of complex underlying steady flows, essential to the fan noise problem, were studied in conjunction with the immersed boundary ap-

proach, a first in the CAA literature to the author's knowledge. The effects of the presence of a low Mach-number underlying steady flow were shown, but higher-speed flows caused instability.

- The HOP scheme was validated on a variety of classic test cases, of increasing complexity (first in 2D and then in 3D), including, if needed, the appropriate wall boundary condition.

- Two different time integration scheme were implemented and compared in detail on a variety of validation cases. Although the optimised Runge-Kutta schemes are theoretically the most efficient, when the time step is restricted because of stability concerns, the optimised Adams-Bashforth scheme becomes the optimal choice.

- Several test cases representative of sound propagation in turbofan engines were also studied, and computations made with HOP were compared with analytical and alternative computational solutions. It was also observed that the wall algorithm could handle complex, realistic geometries, but some important inaccuracies appeared close to the wall boundaries, which caused a dissipation of acoustic modes as a function of their cut-off ratio.

- Two different boundary conditions, introducing the input acoustic modes while minimising the reflections, were implemented. The explicit absorbing boundary was found to perform better than a 1-D radiation condition.

- It was shown that using a high-order method meant obtaining a gain of at least one order of magnitude in the computing time, when compared to a traditional CFD method, AU3D.

As noise constraints become fundamental for the airlines and the aeronautics industry, engines must become quieter; the associated design choices affect other aspects of the turbomachinery's behaviour, so computational modelling should ultimately include all these effects and their interactions to obtain a complete design solution. Robust computational methods already exist to simulate fluid dynamics (CFD), and their interaction with structures (aeroelasticity). This includes the internal generation of sound, but not its propagation to the point of observation.

In this study, dedicated, efficient acoustic propagation methods, to be used in conjunction with these traditional CFD techniques, were investigated. Many existing methods CAA employ 2D models, with simplifying assumptions (uniform or irrotational mean flow *etc.*). To study more general interaction effects, a set of 3D perturbed Euler equations was chosen here, making use of the increase in available computing power. An hybrid linear approach splits the equations between the steady mean flow (computed by a dedicated code) and the acoustic perturbations (governed by the LEE equations).

The computational efficiency of the chosen discretisation method is then of paramount importance. Traditional CFD techniques are inefficient for acoustic computations, and many dedicated, high-order accurate methods have emerged. Popular methods were reviewed, including implicit or explicit finite difference and finite element schemes. In the current work, a structured, finite difference approach that dispenses from using traditional meshing techniques was taken.

Finding correct ways of handling non-trivial wall geometries is an important topic of research in CAA, even before 3D situations are considered. A 2D wall boundary condition by Kurbatskii, designed for finite difference discretisations, and allowing the use of a simple regular grid, was extended to 3D as described in detail in Chapter 3. This represents one of the main contributions of the current work. It is based on a complex but systematic algorithm that analyses the geometrical situation for each relevant point behind the wall surface, and determines the appropriate normal direction. The pressure gradient on the wall surface is obtained using an extrapolation optimised in the wavenumber space, performed along the coordinate axes. This is done in a pre-processing phase, and the large resulting matrices are stored in a sparse fashion and inverted using an appropriate iterative method. This approach allows the automatic treatment of complex geometries without using lengthy meshing procedures, which can be problematic, particularly with high-order discretisations. Furthermore, body-fitted grids were developed for traditional, more dissipative CFD schemes and can lead to instability and inaccuracy if used with high-order schemes, which are generally less robust, particularly if the grid is highly stretched or of low quality.

In Chapter 4, the results of several classic test cases, used to verify the correct implementation of the chosen CAA methods, were presented. The 3D wall boundary condition of Chapter 3 was tested against a standard 3D scattering benchmark. The results were overall correct, but the accuracy was inferior than with similar 2D results. Because the normal directions were estimated correctly, this is due to the additional extrapolations required. It was shown that the new 3D treatment converged as the Helmholtz number increased. It appeared that small time steps were needed to prevent instability near the wall, which, in a sense, reduces the overall temporal order of the method.

In Chapter 5, the developed code was used for cases directly representative of the aero-acoustic problems described in the introduction. Detailed comparisons of spinning mode propagation from an axisymmetric inlet with results from equivalent low- and high-order methods confirmed that dissipation occurred close to the wall boundary. For plane wave propagation results, the overall scheme remains more efficient than low-order approaches, as a gain of at least one order of magnitude in the computational time needed was clearly established.

Because of the inaccuracies observed, the wall boundary in its present state cannot be directly applied to practical engineering problems such as the fan noise cases presented in Chapter 1. For now, traditional structured approaches using body-fitted grids, or unstructured discontinuous Galerkin techniques remain the principal solutions to be used. For the approach investigated in the current work to be salvaged, the accuracy of the wall boundary in 3D would need to be enhanced, probably orienting research along the directions outlined below. The inclusion of steady flows with the immersed wall boundary condition, exhibited in Chapters 4 and 5, is also an important contribution of this work, but instability problems that occurred in the presence of steady flows with important Mach number represent an important limitation of the method in its current state.

To evaluate wether an immersed boundary approach should be retained, it should be kept in mind that other approaches also introduce errors: “chimera” grids are connected using extrapolations, and traditional deformed or unstructured grids introduce errors. Furthermore, a body-fitted grid of good quality is often very difficult to obtain, particularly for the inlet mouth region. In the comparable study of Özyörük [9], it was generated with difficulty, in a specific axisymmetric case. This strongly limits the application of grid-mapping methods to the design of modern inlets, where several asymmetric geometries need to be investigated.

6.2 Recommendations for further work

Extrapolation scheme: compared to the 2D method, the accuracy of the 3D extrapolation procedure is problematic because of the additional extrapolations required. This is a major difficulty, and future research in this direction could aim at improving results, while carefully maintaining stability (following the discussion of Section 3.3 at the end of Chapter 3). A more stable method would allow the time step to be extended, with substantial gains on the computational efficiency relative to low-order methods, but this must not be offset by a loss of spatial accuracy. Attempts made in this direction during the current research were inconclusive. It is too early to say wether the limitations of high-order accurate 3D extrapolation are fundamental, and the present method represents the best accuracy/stability compromise, or wether a better method can be found. The approach of Bin *et al.* [124], using only one interpolation direction, seems promising in that respect. Some dissipation is also probably caused by the selective damping used at the boundaries, therefore the use of higher-order filters which would preserve more of the frequencies of interest could be investigated.

In order to reduce the instability appearing close to the wall boundary, particularly in the presence of large Mach number flows, up-winding techniques such as those of Ref. [83] could be investigated, and integrated in the algorithm of Chapter 3. The use of conservative LEE equations could also possibly lead to more numerical stability [46].

Liners: because of its wide use in modern aero-engines, the soft-wall boundary condition, used to model absorbing panels (or “liners”), is of great interest in CAA, and should be added to the current method. Difficulties arise when frequency-domain impedance models are used with time-domain computations, but several successful approaches now exist, as was discussed in Section 2.3.2, and their inclusion in the current immersed boundary would be straightforward: Eq. (2.16) needs to be modified. But the presence of mean flow next to a porous wall, in an inviscid model, leads to fundamental instability problems which might be difficult to handle because of the current method's lack of robustness.

Hybrid system: on a practical level, the connection between the propagation scheme and the source of sound would need to be carefully designed, to obtain the complete design system described in the introduction. Both codes would need to run together, in the time domain, for optimal efficiency, with correct data transmission between boundaries. The absorbing boundary condition used in Chapter 5 makes this easier, since it can use an acoustic solution directly as input. For certain cases, a feedback of the waves reflected at the inlet mouth into the source domain could be necessary.

Non-linearities: although non-linear effects were not included in this study, the current approach allows such an extension by adding the relevant corrective terms. As pointed out in Chapter 2, shock-capturing techniques could also be avoided through the careful use of pressure-sensitive selective dissipation. In the context of noise propagation from the aircraft inlet, it is important to consider where to set the limit of the middle-field domain, where the new CAA method would be used for acoustic propagation. For example, if computing N-wave propagation, the near field zone should include the region where the propagation is non-linear because of the high amplitude of the waves.

Other applications: the immersed boundary approach developed here could be applied to other problems; for example, 3D finite difference computations of sound scattering from complex or disconnected geometries, which are difficult to model with traditional structured grids. It would also be interesting to use this approach for optimisation problems, where several geometries need to be assessed automatically, by varying a parameter for example: the pre-processing could be done automatically.

Bibliography

[1] M. J. T. Smith. *Aircraft Noise*. Cambridge University Press, 1989.

[2] K. A. Kurbatskii and C. K. W. Tam. Cartesian Boundary Treatment of Curved Walls for High-order Computational Aeroacoustics Schemes. *AIAA Journal*, 35(1):133–140, 1997.

[3] J. E. Green. Civil Aviation and the Environmental Challenge. *The Aeronautical Journal*, 107(1072):281–299, June 2003.

[4] P. C. Ruffles. Aero Engines of the Future. *The Aeronautical Journal*, 107(1072):307–321, June 2003.

[5] M. D. Guynn and E. D. Olson. Evaluation of an aircraft concept with overwing, hydrogen-fueled engines for reduced noise and emissions. Technical Report NASA/TM-2002-211926, NASA, Langley Research Center, `http://techreports.larc.nasa.gov/ltrs/2002-cit.html`, September 2002.

[6] A. H. Nayfeh et al. Acoustics of Aircraft Engine-Duct Systems. *AIAA Journal*, 13(2):130–153, 1975.

[7] C. Bogey. *Calcul Direct du Bruit Aérodynamique et Validation de Modèles acoustiques Hybrides.* PhD thesis, École Centrale de Lyon, Laboratoire de Mécanique des Fluides et d'Acoustique, Lyon, France, April 2000.

[8] H. Shen and C. K. W. Tam. Numerical simulation of the Generation of Axisymmetric Mode Jet Screech Tones. *AIAA Journal*, 36(10):1801–1807, 1998.

[9] Y. Özyörük. *Sound Radiation from Ducted Fans Using Computational Aeroacoustics on Parallel Computers*. PhD thesis, Pensylvenia State University, 1995.

[10] E. Envia. Fan Noise Reduction: an Overview. *International Journal of Aeroacoustics*, 1(1):43–64, 2002.

[11] J. M. Mendoza, B. Schuster, J. H. Lan, and C. Gerhold. Application of Duct Propagation Codes to the Prediction of Far Field Turbofan Generated Noise. [131].

[12] E. J. Richards and D. J. Mead. *Noise and Acoustic Fatigue in Aeronautics*. John Wiley & Sons, 1968.

[13] J. M. Tyler and T. G. Sofrin. Axial Flow Compressor Noise Studies. *SAE Transactions*, 70:309–332, 1962.

[14] A. McAlpine and M. J. Fisher. On the Prediction of "buzz-saw" Noise in Aero-Engine Inlet Ducts. *Journal of Sound and Vibration*, 248(1):123–149, 2001.

[15] M. J. Fisher and R. H. Self. Aeroacoustic Research in Europe: the CEAS-ASC Rerport on 2001 Highlights. *Journal of Sound and Vibration*, 258(1):1–30, 2002.

[16] J. G. Marshall and M. Imregun. A Review of Aeroelasticity Methods with Emphasis on Turbomachinery Applications. *Journal of Fluids and Structures*, 10(3):237–267, 1996.

[17] M. Vahdati, A. I. Sayma, C. Bréard, and M. Imregun. Computational Study of Intake Duct Effects on Fan Flutter Stability. *AIAA Journal*, 40(3):408–418, 2002.

[18] X. Wu, A. I. Sayma, M. Vahdati, and M. Imregun. Computational techniques for aeroelasticity and aeroacoustic analyses of aero-engine fan assemblies. In *International Conference on Fans*, number C631/005/2004, pages 85–98, ImechE Headquarters, London, UK, 9-10 Nov. 2004. ImechE, Professional Engineering Publishing Ltd.

[19] M. E. Goldstein. *Aeroacoustics*. Mc Graw-Hill, 1976.

[20] S. W. Rienstra. Sound transmission in slowly varying circular and annular lined ducts with flow. *Journal of Fluid Mechanics*, 380:279–296, 1999.

[21] C. J. Chapman. Sound Radiation from a Cylindrical Duct. Part1. Ray Structure of the Duct Modes and of the External Field. *Journal of Fluid Mechanics*, 281:293–311, 1994.

[22] G. M. Keith. *A Theoretical Investigation Into the Acoustic Radiation from an Aeroengine Intake*. PhD thesis.

[23] P. Gliebe, R. Mani, and H. Shin. Aeroacoustic Prediction Codes. Technical Report NASA/CR-2000-210244, NASA Glenn Research Center, 2000.

[24] K. A. Kurbatskii and C. K. W. Tam. Microfluid Dynamics and Acoustics of Resonant Liners. *AIAA Journal*, 38(8):1331–1339, 2000.

[25] T. J. Chung. *Computational Fluid Dynamics*. Cambridge University Press, Cambridge, U.K., 2002.

[26] A. I. Sayma, M. Vahdati, and M. Imregun. An Integrated Nonlinear Approach for Turbomachinery Forced Response Prediction. Part I: Formulation. *Journal of Fluids and Structures*, 14:87–101, 2000.

[27] A. I. Sayma, M. Vahdati, and M. Imregun. An Integrated Nonlinear Approach for Turbomachinery Forced Response Prediction. Part II: Case Studies. *Journal of Fluids and Structures*, 14:103–125, 2000.

[28] A. I. Sayma, M. Vahdati, L. Sbardella, and M. Imregun. Modelling of Three-Dimensional Viscous Compressible Turbomachinery Flows Using Unstructured Hybrid Grids. *AIAA Journal*, 38(6):945–954, 2000.

[29] C. L. Rumsey, R. T. Biedron, F. Farassat, and P. L. Spence. Ducted-Fan Engine Acoustic Predictions Using a Navier-Stokes Code. *Journal of Sound and Vibration*, 213(4):643–664, 1998.

[30] C. K. W. Tam. Computational Acoustics: Issues and Methods. *AIAA Journal*, 33(10):1788–1796, 1995.

[31] D. P. Lockard. An investigation of accuracy requirements for computational aeroacoustics. Master's thesis, George Washingon University, JIAFS, Hampton, VA, USA, July 1993.

[32] C. K. W. Tam and J. C. Webb. Dispersion-Relation Preserving Finite Difference Schemes for Computational Acoustics. *Journal of Computational Physics*, 107:262–281, 1993.

[33] J. C. Hardin, J. R. Ristorcelli, and C. K. W. Tam, editors. *ICASE/LARC Workshop on Benchmark Problems in Computational Acoustics*. 1995. NASA CP 3300.

[34] A. S. Lyrintzis. Integral Methods in Computational Aeroacoustics - From the CFD (Near-Field) to the (Acoustic) Far-Field. In *CEAS Workshop "From CFD to CAA"*, Athens, Greece, 2002.

[35] Y. Özyörük, L. N. Long, and V. Ahuja. Time Domain Simulation of Radiation from Ducted Fans with Liners. In 7^{th} *AIAA/CEAS Aeroacoustics Conference*, 2001. AIAA paper 2001-2171.

[36] Y. Özyörük and V. Ahuja. Numerical Simulation of Fore and Aft Sound Fields of a Turbofan. *AIAA Journal*, 42(10):2028–2034, 2004.

[37] D. Stanescu, D. Ait-Ali-Yahia, W. G. Habashi, and M. P. Robichaud. Multidomain Spectral Computations of Sound Radiation from Ducted Fans. *AIAA Journal*, 37(3):296–302, 1999.

[38] D. Stanescu, D. Ait-Ali-Yahia, W. G. Habashi, and M. P. Robichaud. Spectral Element Method for Linear Fan Tone Noise Radiation. *AIAA Journal*, 42(4):696–705, 2004.

[39] D. Stanescu, M. Y. Hussaini, and F. Farassat. Aircraft engine noise scattering by fuselage and wings: a computational approach. *Journal of Sound and Vibration*, 263:319–333, 2003.

[40] C. Bréard. Acoustic Propagation and Radiation Modeling of Lined Duct With Linear and Non-linear Frequency-Domain Solver. In 9^{th} *AIAA/CEAS Aeroacoustics Conference*, number AIAA 2003-3265, Hilton Head, South Carolina, U.S.A., May 2003.

[41] W. Eversman and A. V. Parrett and J. S. Preisser and R. J. Silcox. Contributions to the finite element solution of the fan noise radiation problem. *Journal of Vibration, Acoustics, Stress, and Reliability in Design, Transactions of the ASME*, 107:216–223, April 1985.

[42] J. H. Lan, Y. Guo, and C. Bréard. Validation of Acoustic Propagation Code with JT15D Static and Flight Test Data. [131].

[43] C. K. W. Tam and N. Pastouchenko. Noise from Fine-scale Turbulence of Nonaxisymmetric Jets. *AIAA Journal*, 40(3):456–464, 2002.

[44] C. Bailly and C. Bogey. Contributions Of Computational Aeroacoustics to Jet Noise Research and Prediction. *International Journal of Computational Fluid Dynamics*, 18(6):481–491, 2004.

[45] O. Marsden, C. Bogey, and C. Bailly. High-order curvilinear simulations of flows around non-Cartesian bodies. [131].

[46] S. Redonnet. *Simulation de la Propagation Acoustique en Présence d'Écoulements Quelconques et de Structures Solides Par Résolution Numérique des*

Équations d'Euler. PhD thesis, Université Bordeaux 1, Bordeaux, France, November 2001.

[47] P. Morse and K. Ingard. *Theoretical Acoustics*. Mc Graw-Hill, 1968.

[48] F. Fahy. *Foundations of Engineering Acoustics*. Academic Press, 2001.

[49] F. Farassat and M. K. Myers. Extension of Kirchhoff's formula for Radiation from Moving Surfaces. *Journal of Sound and Vibration*, 123:451–460, 1988.

[50] J. E. Ffowcs Williams and D. L. Hawking. Sound Generation by Turbulence and Surfaces in Arbitrary Motion. *Transactions of the Royal Society of London*, A264:321–342, 1969.

[51] F. Farassat. Linear Acoustic Formulas for Calculation of Rotating Blade Noise. *AIAA Journal*, 19:1122–1120, 1981.

[52] X. Zhang, X. X. Chen, C. L. Morfey, and B. J. Tester. Computation of Fan Noise Radiation through A Realistic Engine Exhaust Geometry with Flow. In 9^{th} *AIAA/CEAS Aeroacoustics Conference*, number AIAA 2003-3267, Hilton Head, South Carolina, U.S.A., May 2003.

[53] P. J. Morris, L. N. Long, et al. Simulations of supersonic Jet Noise. *International Journal of Aeroacoustics*, 1(1):17–41, 2002.

[54] C. Bailly and D. Juvé. Numerical Solutions of Acoustic Propagation Problems Using Linearized Euler Equations. *AIAA Journal*, 38(1):22–29, 2000.

[55] R. J. Astley, J. A. Hamilton, N. Baker, and E. H. Kitchen. Modelling tone propagation from turbofan inlets the effect of extended lip liners. In *Proceedings of the* 8^{th} *AIAA/CEAS Aeroacoustics Conference*, number AIAA 2002-2449, Breckenridge, Colorado, USA, 2002.

[56] C. Bogey, C. Bailly, and D. Juvé. Computation of Flow Noise Using Source Terms in Linearized Euler's Equations. *AIAA Journal*, 40(2):235–243, 2002.

[57] C. K. W. Tam and H. Shen. Direct Computation of Nonlinear Acoustic Pulses Using High Order Finite Difference Schemes. In 15^{th} *AIAA Aeroacoustics Conference*, 1993. AIAA paper 93-4325.

[58] P. J. Morris, L. N. Long, A. Bangalore, and Q. Wang. A Parallel Three-Dimensional Computational Aeroacoustics Method Using Nonlinear Disturbance Equations. *Journal of Computational Physics*, 133:56–74, 1997.

[59] L. N. Long. A Nonconservative Nonlinear Flowfield Splitting Method for 3-D Unsteady Fluid Dynamics. In 6^{th} *AIAA/CEAS Aeroacoustics Conference*, 2000. AIAA paper 2000-1998.

[60] J. C. Hardin and C. K. W. Tam, editors. *Second Computational Acoustics Workshop on Benchmark Problems*. NASA Langley Research Center, Hampton VA, 1997. NASA CP 3352.

[61] J. C. Hardin, D. Huff, and C. K. W. Tam, editors. *Third Computational AeroAcoustics (CAA) Workshop on Benchmark Problems*. Number NASA/CP-2000-209790. Ohio Aerospace Institute, Cleveland, Ohio, USA, November 1999.

[62] W. Press, P. Flannery, S. Teulosky, and W. Vetterling. *Numerical Recipes (FORTRAN)*. Cambridge University Press, 1989.

[63] D. P. Lockard, K. S. Brenner, and H. L. Atkins. High-Accuracy Algorithms for Computational Acoustics. *AIAA Journal*, 33(2):246–251, 1995.

[64] C. Bogey and C. Bailly. A Family of Low Dispersive and Low Dissipative Explicit Schemes for Noise Computations. *Journal of Computational Physics*, 194:194–214, 2004.

[65] J. Berland, C. Bogey, and C. Bailly. Optimized explicit schemes: matching and boundary schemes and 4th-order Runge-Kutta algorithm. [131].

[66] R. R. Mankbadi, M. E. Hayder, and L. A. Povinelli. Structure of Supersonic Jet Flow and Its Radiated Sound . *AIAA Journal*, 32(5):897–906, 1994.

[67] F. Owis and P. Balakumar. Jet Noise Computation Using Explicit McCormack Schemes and Non-Reflecting Boundary Conditions. *AIAA Journal*, 39(10):2019, 2001.

[68] S. K. Lele. Compact Finite Difference Schemes with Spectral-Like Resolution. *Journal of Computational Physics*, 103(16):42, 1992.

[69] A. Harten and S. Osher. Uniformly High-Order accurate Non-Oscillatory Schemes, I. *SIAM Journal of Numerical Analysis*, 24:279–309, 1987.

[70] J. Casper and K. R. Meadows. Using High-Order Accurate Essentially Nonoscillatory Schemes for Aeroacoustic Applications. *AIAA Journal*, 34(2):244–250, 1996.

[71] G. S. Jiang and C. W. Shu. Efficient Implementation of Weighted ENO Schemes. *Journal of Computational Physics*, 126:202–212, 1996.

[72] K. J. Baumeister and S. J. Horowitz. Finite Element-Integral Acoustic Simulation of JT15D Turbofan Engine. *Journal of Vibration, Acoustics, Stress, and Reliability in Design, Transactions of the ASME*, 106:405–413, July 1984.

[73] H. L. Atkins and C.-W. Shu. Quadrature-Free Implementation of the Discontinuous Galerkin Method for Hyperbolic Equations. In 2^{nd} *AIAA/CEAS Aeroacoustics Conference*, 1996. AIAA paper 96-1683.

[74] C. Canuto, M. Y. Hussaini, A. Quarteroni, and T. A. Zang. *Spectral Methods in Fluid Dynamics*. Springer-Ferlag, New-York/Berlin, 1988.

[75] M. Ganesh and I. G. Graham. A high-order algorithm for obstacle scattering in three dimensions. *Journal of Computational Physics*, 198:211–242, 2004.

[76] S. J. Sherwin and G. E. Karniadakis. Tetrahedral hp Finite Elements: Algorithms and Flow Simulations. *Journal of Computational Physics*, 124:14–45, 1996.

[77] D. Casalino, M. Roger, and M. C. Jacob. Prediction of Sound Propagation in Ducted Potential Flows Using Green's Function Discretization. *AIAA Journal*, 42(4):736, 2004.

[78] D. Casalino, P. D. Francescantonio, and Y. Druon. GFD Predictions of Fan Noise Propagation. [131].

[79] K. Yokoi, F. Xiao, H. Liu, and K. Fukasaku. Three-Dimensional Numerical Simulation of Flows With Complex Geometries in a Regular Cartesian Grid and its Application to Blood Flow in Cerebral Artery with Multiple Aneurysms. *Journal of Computational Physics*, 202:1–19, 2005.

[80] T. Z. Dong and R. R. Mankbadi. Direct Numerical Simulation of Engine Internal Noise Propagation and Radiation. In *First Joint CEAS/AIAA Aeroacoustics Conference, Volume I*. DGLR, 1995. CEAS/AIAA paper 95-064.

[81] P. J. Morris and C. Shieh. 3D Calculations of Acoustic Scatterings by a Sphere: a Parallel Implementation. In Hardin and Tam [60]. NASA CP 3352.

[82] E. J. Avital. Optimized Differentiation Schemes on Non-Uniformgrids for Computational Aeroacoustics. *Journal of Computational Acoustics*, 10(2):195–209, 2002.

[83] M. Zhuang and R. F. Chen. Applications of High-Order Optimized Upwind Schemes for Computational Aeroacoustics. *AIAA Journal*, 40(3):443–449, 2002.

[84] K. A. Kurbatskii and C. K. W. Tam. A Wavenumber Based Extrapolation and Interpolation Method for Use in Conjunction with High-Order Finite Difference Schemes. *Journal of Computational Physics*, 157:588–617, 2000.

[85] C. K. W. Tam and K. A. Kurbatskii. Multi-Size-Mesh Multi-Time-Step Dispersion-Relation-Preserving Scheme for Multiple-Scales Aeroacoustics Problems. *International Journal of Computational Fluid Dynamics*, 17(2):119–132, 2003.

[86] C. Wall, C. D. Pierce, and P. Moin. A Semi-implicit Method for Resolution of Acoustic Waves in Low Mach Number Flows. *Journal of Computational Physics*, 181:545–563, 2002.

[87] F. Q. Hu, M. Y. Hussaini, and J. L. Manthey. Low-Dissipation and Low-Dispersion Runge-Kutta Schemes for Computational Acoustics. *Journal of Computational Physics*, 124:177–191, 1996.

[88] D. Stanescu and W. G. Habashi. 2N-storage Low-Dissipation and Dispersion Runge-Kutta Schemes for Computational Acoustics. *Journal of Computational Physics*, 143:674–681, 1998.

[89] K. W. Thompson. Time Dependent Boundary Conditions for Hyperbolic Systems, I. *Journal of Computational Physics*, 68:1–24, 1987.

[90] M. B. Giles. Nonreflecting Boundary Conditions for Euler Equations Calculations. *AIAA Journal*, 28(12):2050–2058, 1990.

[91] F. Q. Hu. On Absorbing Boundary Conditions for Linearized Euler Equations by a Perfectly Matched Layer. *Journal of Computational Physics*, 129:201–219, 1996.

[92] C. K. W. Tam, L. Auriault, and F. Cambuli. Perfectly Matched Layer as an Absorbing Boundary Conditions for the Linearized Euler Equations in Open and Ducted Domains. *Journal of Computational Physics*, 144:213–234, 1998.

[93] F. Q. Hu. On using Perfectly Matched Layer for the Euler Equations with a Non-Uniform Mean Flow. [131].

[94] A. Bayliss and E. Turkel. Far-field Boundary Conditions for Compressible Flows. *Journal of Computational Physics*, 48:182–199, 1982.

[95] C. K. W. Tam, J. Fang, and K. A. Kurbatskii. Non-Homogeneous Radiation and Outflow Boundary Conditions Simulating Incoming Acoustic and Vorticity Waves for Exterior Computational Aeroacoustics Problems. *International Journal for Numerical Methods in Fluids*, 26:1107–1123, 1998.

[96] X. D. Li, N. Schönwald, and F. Thiele. Numerical Computation of Sound Propagation and Radiation in a Duct. In 7^{th} *AIAA/CEAS Aeroacoustics Conference*, 2001. AIAA paper 2001-2179.

[97] C. K. W. Tam and L. Auriault. Time-Domain Impedance Boundary Condition for Computational Aeroacoustics. *AIAA Journal*, 34(5):917–923, 1996.

[98] L. Sbardella, M. Imregun, and B. Tester. A Time Domain Method for the Prediction of Sound Attenuation in Lined Ducts. *Journal of Sound and Vibration*, 239(3):379–396, 2001.

[99] J. A. Lordi, G. F. Homicz, and R. G. Rehm. Effects of Finite Duct Length and Blade Chord on Noise Generation by a Rotating Blade Row. In *AIAA* 7^{th} *Fluids and Plasmadynamics Conference*, 1974. AIAA paper 74-555.

[100] N. C. Ovenden and S. W. Rienstra. Mode-Matching Strategies in Slowly Varying Engine Ducts. *AIAA Journal*, 42(9):1832–1840, 2004.

[101] T. Z. Dong and L. A. Povinelli. On computations of Duct Acoustics with Near Cut-Off Frequency. In Hardin and Tam [60]. NASA CP 3352.

[102] S. Zheng, M. Zhuang, and F. Thiele. Noise Prediction and Optimization System for Turbofan Engine Inlet Duct Design. [131].

[103] M. R. Visbal and D. V. Gaitonde. Nonreflecting Boundary Conditions for the Time-dependent Convective Wave Equation in a Duct. *Journal of Computational Physics*, 197:737–758, 2004.

[104] D. Givoli and I. Patlashenko. Dirichlet-to-Neumann Boundary Condition for Time-dependent Dispersive Waves in Three-Dimensional Guides. *Journal of Computational Physics*, 199:339–354, 2004.

[105] C. K. W. Tam and Z. Dong. Wall Boundary Conditions for High-Order Finite-Difference Schemes in Computational Aeroacoustics. *Theoretical Computational Fluid Dynamics*, 6:303–322, 1994.

[106] E. A. Fadlun, R. Verzicco, P. Orlandi, and J. Mohd-Yusof. Combined immersed-boundary finite-difference methods for three-dimensional complex flow simulations. *Journal of Computational Physics*, 161:35–60, 2000.

[107] S. J. Sherwin and J. Peiro. Mesh generation in Curvilinear Domains Using High-Order Elements. *International Journal of Numerical Methods in Engineering*, 153:207–223, 2002.

[108] E. Manoha, R. Guenanff, S. Redonnet, and M. Terracol. Acoustic Scattering From Complex Geometries. [131].

[109] C. K. W. Tam and F. Q. Hu. An Optimized Multi-Dimensional Interpolation Scheme for Computational Aeroacoustics Applications Using Overset Grids. [131].

[110] C. Cheong and S. Lee. Grid-Optimized Dispersion-Relation-Preserving Schemes on General Geometries for Computational Aeroacoustics. *Journal of Computational Physics*, 174(1):248–276, 2001.

[111] Y. M. Chung and P. G. Tucker. Accuracy of Higher-Order Finite Difference Schemes on Nonuniform Grids. *AIAA Journal*, 41(8):1609–1611, 2003.

[112] M. R. Visbal and D. V. Gaitonde. On the Use of Higher-Order Finite-Difference Schemes on Curvilinear and Deforming Meshes. *Journal of Computational Physics*, 181:155–185, 2002.

[113] C. S. Peskin. The Immersed Boundary Method. *Acta Numerica*, pages 479–518, 2002.

[114] L. B. Tran and H. S. Udaykumar. A Particle-Level Set-Based Sharp Interface Cartesian Grid Method for Impact, Penetration, and Void Collapse. *Journal of Computational Physics*, 193:469–510, 2004.

[115] A. Gilmanov, F. Sotiropoulos, and E. Balaras. A General Reconstruction Algorithm for Stimulating Flows with Complex 3D Immersed Boundaries on Cartesian Grids. *Journal of Computational Physics*, 191:660–669, 2003.

[116] Y.-H. Tseng and J. H. Ferziger. A Ghost-cell Immersed Boundary Method for Flow in Complex Geometry. *Journal of Computational Physics*, 192:593–623, 2003.

[117] G. Yang, D. M. Causon, and D. M. Ingram. Calculation of Compressible Flows about Complex Moving Geometries Using a Three-Dimensional Cartesian Cut Cell Method. *International Journal for Numerical Methods In Fluids*, 33:1121–1151, 2000.

[118] M. P. Kirkpatrick, S. W. Armfield, and J. H. Kent. A Representation of Curved Boundaries for the Solution of the NavierStokes Equations on a

Staggered Three-dimensional Cartesian Grid. *Journal of Computational Physics*, 184:1–36, 2003.

[119] W. J. Coirier and K. G. Powell. An Accuracy Assessment of Cartesian-Mesh Approaches for the Euler Equations. *Journal of Computational Physics*, 117:121–131, 1995.

[120] B. Lombard and J. Piraux. Numerical Treatment Of Two-Dimensional Interfaces for Acoustic And Elastic Waves. *Journal of Computational Physics*, 195:90–116, 2004.

[121] K. A. Kurbatskii. *Solid Wall Boundary Conditions for Computational Aeroacoustics Problems*. PhD thesis, The Florida State University, College of Arts and Science, Florida, USA, Fall 1997.

[122] M. J. Aftosmis, M. J. Berger, and J. E. Melton. Robust and Efficient Cartesian Mesh Generation for Component-Based Geometry. *AIAA Journal*, 36(6):946–951, 1998.

[123] A. S. Glassner, editor. *Graphic Gems*. AP Professional, 1995.

[124] J. Bin, C. Cheong, and S. Lee. Optimised Boundary Treatment of Curved Walls for High-Order Computational Aeroacoustics Schemes. *AIAA Journal*, 42(2):414–417, 2004.

[125] P. J. Morris. The Scattering of Sound from a Spatially Distributed, axisymmetric cylindrical source by a Circular Cylinder. *Journal of the Acoustical Society of America*, 97(5):2651–2656, 1995.

[126] P. J. Morris. Scattering of Sound from a Spatially Distributed, Spherically Symmetric Source by a Sphere. *Journal of the Acoustical Society of America*, 98(6):3536–3539, 1995.

[127] F. M. White. *Viscous Fluid Flow*. Mechanical Engineering. Mc Graw-Hill International, 2nd edition, 1991.

[128] M. M. Denn, editor. *Process Fluid Mechanics*. Prentice Hall PTR.

[129] J. A. Lordi and G. F. Homicz. A Note on The Radiative Directivity Patterns of Duct Acoustic Modes. *Journal of Sound and Vibration*, 41(3):283–290, 1975.

[130] R. Astley and W. Eversman. Wave Enveloppe and Infinite Element Schemes for Fan Noise Radiation from Turbofan Inlets. *AIAA Journal*, 22:1719–1726, 1984.

[131] 10^{th} *AIAA/CEAS Aeroacoustics Conference*, Manchester, U.K., May 2004.

[132] A. Chaigne. *Ondes acoustiques*. Les éditions de l'École Polytechnique, Palaiseau, France, 2001.

[133] M. Goossens, F. Mittelbach, and A. Samarin. *The LaTeXCompanion*. Addison-Wesley, 1994.

[134] H. J. Greenberg. A simplified introduction to LaTeX. `http://www.cudenver.edu/~hgreenbe/`, April 2000.

[135] M. M. Cand. Computing the 3-Dimensional Propagation of Forward-Arc Fan Noise from Aero-Engines. In *Up and Coming in Fluid Machinery, Seminar Proceedings*, London, U.K., 9 October 2003. IMechE.

[136] M. M. Cand, A. I. Sayma, and M. Imregun. 3-Dimensional Noise Propagation Using a Cartesian Grid. [131].

[137] M. M. Cand, A. I. Sayma, and M. Imregun. Efficient 3-Dimensional Noise Propagation using an Immersed Boundary. *Journal of Sound and Vibration*. Submitted for consideration.